ABSTRACT

Name: Sergey A. Uzunyan Department: Physics

Title: A SEARCH FOR CHARGE 1/3 THIRD GENERATION LEPTOQUARKS IN MUON CHANNELS

Major: Physics Degree: Doctor of Philosophy

Approved by: Date:

Dissertation Director

NORTHERN ILLINOIS UNIVERSITY

ABSTRACT

Leptoquarks are exotic particles that have color, electric charge, and lepton number and appear in extended gauge theories and composite models. Current theory suggests that leptoquarks would come in three different generations corresponding to the three quark and lepton generations. We are searching for charge 1/3 third generation leptoquarks produced in $p\bar{p}$ collisions at $\sqrt{s}$=1.96 TeV using data collected by the DØ detector. Such leptoquarks would decay into either a tau-neutrino plus a b-quark or, if heavy enough, to a tau-lepton plus a t-quark. We present preliminary results on an analysis where both leptoquarks decay into neutrinos giving a final state with missing energy and two b-quarks using 367 pb^{-1} of Run II DØ data taken between August 2002 and September 2004. We place upper limits on $\sigma(p\bar{p} \rightarrow LQ\overline{LQ})B^2$ as a function of the leptoquark mass M_{LQ}. Assuming $B = 1$, we exclude at the 95% confidence level third generation leptoquarks with $M_{LQ} < 197$ GeV/c^2.

NORTHERN ILLINOIS UNIVERSITY

A SEARCH FOR CHARGE 1/3 THIRD GENERATION LEPTOQUARKS IN MUON CHANNELS

A DISSERTATION SUBMITTED TO THE GRADUATE SCHOOL
IN PARTIAL FULFILLMENT OF THE REQUIREMENTS
FOR THE DEGREE
DOCTOR OF PHILOSOPHY

DEPARTMENT OF PHYSICS

DEKALB, ILLINOIS
August 2006

In accordance with departmental and Graduate School policies, this dissertation is accepted in partual fulfillment of degree requirements

Certification:

_____

Dissertation Director

_____

Date

DEDICATION

To my parents, Andrey and Lidia, and grandfather Vartan.

ACKNOWLEDGEMENT

The presented analysis could never be done without the help and support of the people of the DØ collaboration. The data collected at the DØ detector are the combined product of the efforts of everyone in the collaboration and I am happy to say that I have been working at the right place and at the right time in such s friendly environment as the DØ experiment.

I'm especially grateful to Arthur Maciel, Christos Leonidopolus, Tim Cristiansen and Burair Kothari for the challenging and interesting work in the development of the DØ Level 2 muon trigger system. I would like to thank members of the New Phenomena group for their week-by-week discussions, suggestions and comments, and especially Arnaud Duperrin and Andriy Zatserklyaniy for the development of algorithms directly used in this analysis. I would like to thank Gerald Blazey and other members of the Northern Illinois Center for Accelerator and Detector Development for the everyday support of my work. I would like to say many thanks to my adviser David Hedin for the key proposals in the analysis and for his careful and lightning edit of all the details of this paper. And finally I wish to thank the Department of Education and the National Science Foundation for their support of this work.

TABLE OF CONTENTS

Page

LIST OF TABLES vii

LIST OF FIGURES viii

CHAPTER

1 INTRODUCTION 1

1.1 Particle and Forces 1
1.1.1 The history of matter splitting 1
1.1.2 The basic forces and their carriers 3
1.1.3 Elementary particle classifications 4
1.2 The Standard Model 6
1.2.1 QED and QCD 6
1.2.2 Electroweak Theory 9
1.3 Possible extensions of the Standard Model 12
1.3.1 Grand Unified Theories 12
1.3.2 Supersymmetry 13
1.4 Search for new particles 14

2 LEPTOQUARKS 15

2.1 Leptoquark Phenomenology 15
2.2 Leptoquark searches at modern colliders 17
2.2.1 HERA anomaly 18
2.2.2 LEP results 19
2.2.3 Hadron collider results 19
2.3 Third generation LQ searches at the Tevatron 21

3 DØ detector at the Fermilab Tevatron 25

3.1 The DØ detector 27
3.1.1 The central tracking system 28
3.1.2 The calorimeter system 32

3.1.3 The muon system 32
3.2 The luminosity monitor detector 36

4 The Level-2 Muon trigger of the DØ Detector 38

4.1 The DØ data acquisition system 38
4.2 The Level-2 Trigger System 39
4.3 The Level-2 Muon Trigger 41
4.3.1 The segment finding algorithms 42
4.3.2 Muon track building 49
4.4 The Level-2 muon trigger performance 51

5 Event Reconstruction 53

5.1 The reconstruction software 54
5.2 Muons 54
5.3 Jets 57
5.3.1 Electromagnetic objects 59
5.3.2 Missing energy 60
5.3.3 Jet b-tagging using the impact parameter 60
5.4 Simulations 62

6 Search for the third generation leptoquarks using mu+jet events . . 65

6.1 Data samples 65
6.2 Data cleaning 66
6.3 Trigger efficiency parameterization 68
6.4 Signal features 69
6.5 Backgrounds 72
6.6 The muon tagging analysis 74
6.7 Combining muon and JLIP b-tag 85
6.8 Systematic uncertainties 90
6.9 Leptoquark Mass Limit 90

LIST OF TABLES

Table		Page
1.1	Generations of the quarks and leptons.	3
1.2	Interactions and mediators.	4
1.3	Examples of baryons and mesons.	5
1.4	Forces and symmetries of the theories included in the Standard Model.	7
1.5	Left-handed doublets under the symmetry group $SU(2)$.	10
2.1	Leptoquark classification according to the Buchmüller-Rückl-Wyler model.	16
2.2	Fermilab mass limits (scalar and vector leptoquarks).	22
4.1	Summary for A- and BC-layer muon segment finding.	49
4.2	Quality definition for the L2 muon tracks.	51
5.1	Type and quality definitions of muon candidates used in this analysis.	56
6.1	Effective luminosities associated with different triggers.	66
6.2	The efficiencies of cleaning cuts for data and Monte-Carlo. Events are selected in the m_T window of 50-90 GeV.	68
6.3	MC samples used for SM background description	73
6.4	Initial data sample selection.	75
6.5	Preliminary cuts. Acceptance values for $M_{LQ3} = 150$ GeV.	78
6.6	Number of data events and expected signal after selection cuts.	83
6.7	Muon tagging analysis summary.	85
6.8	JLIP b-tag after "noQCD" cuts, $M_{LQ3} = 200$ GeV	86
6.9	JLIP b-tag after all μ-tag cuts, $M_{LQ3} = 200$ GeV	87
6.10	JLIP b-tag, $M_{LQ3} = 200$ GeV, optimized $\mu - tag$ cuts.	88
6.11	Summary for muon for MUON + JLIP tagging analysis.	88
6.12	Individual contributions of the backgrounds after the b-tag and relaxed muon cuts. $M_{LQ3} = 200$ GeV	89
6.13	Systematic uncertainty summary (in percents.)	91

LIST OF FIGURES

Figure Page

2.1 (a) neutral current deep inelastic scattering, (b) s-channel leptoquark production, and (c) u-channel leptoquark exchange. 19
2.2 Leptoquark production at LEP: (a, b) pairs via γ^*/Z or q exchange, (c) single production dominant contributions $\gamma \rightarrow q\bar{q}$ and (d) "resolved photon" process. 20
2.3 Leading order Feynman diagrams for leptoquark pair production at hadron colliders. 23
2.4 NLO Cross section for scalar leptoquark pair production [25] . . . 24
3.1 The Fermilab Collider Complex 25
3.2 The DØ Detector 28
3.3 The DØ Central Tracker 29
3.4 The DØ silicon microstrip tracker. 31
3.5 The fiber tracker detector, shown from the direction of the beam pipe. 31
3.6 Isometric view of the central and two end calorimeters. 33
3.7 Exploded view of the muon wire chambers. 34
3.8 Exploded view of the muon scintillation detectors. 35
3.9 The location of the LM detectors. 36
3.10 The Tevatron Run II integrated luminosity. 37
4.1 The DØ Trigger System 39
4.2 Block diagram of the dataflow from the detector front-end systems to the L2 global decision 40
4.3 Data processing in the Level-2 muon trigger system. Two stages of processing are completed in a single crate using SLICs and L2beta processors. Central and forward muon regions are processed in separate crates of similar configuration. 42
4.4 Muon detector structure associated with a central BC-layer octant and its division between processing DSPs. 44
4.5 Detector structure associated with a central A layer DSP. The 72×4 cell "hyperchamber" is constructed from three neighboring PDTs. . 46
4.6 Two B and C "hyperchambers" are inputs for the BC-layer DSPs. A reported segment requires matched stubs in each layer. 47
4.7 Results of A and BC layer code timing tests. 50
4.8 A muon track reconstructed by the L2 (red stars) and offline software. 52
5.1 The DØ data reconstruction framework. 55

5.2 View of the calorimeter in the $r - z$ plane. 59
5.3 Taggability as function of jet E_T (a) , η (b), PV_Z (c), and the corresponding closure plots (d, e, f). 63
6.1 The transverse mass distribution for the W mujet triggered sample. 67
6.2 $\not\!\!E_T$ for the W mujet triggered sample. 67
6.3 MU_JT20_L2M0 trigger. Efficiency (left plot, red graph) as a function of the leading muon p_T measured with a missing H_T trigger and its parameterization (right plot, black graph) with the errors bounds (dotted lines). The efficiency as calculated with the TopTrigger package for the signal sample M=150 GeV (left plot, blue graph) is shown for comparison. 69
6.4 MUJET triggers efficiencies vs $\not\!\!E_T$ and the leading jet E_T for the $M_{LQ3} = 150$ GeV signal sample. 70
6.5 Leptoquark ($M_{LQ3} = 150$ GeV) signal properties: a) jet multiplicity distribution, b) first leading jet E_T, c) second leading jet E_T, d) $\not\!\!E_T$ distribution, e) the minimum $\Delta\phi$ angle between $\not\!\!E_T$ and the nearest jet, f) p_T of the leading muon from semileptonic decay, g) p_T of muons in the dimuon channel 71
6.6 The effect of bad jets removal and jet track confirmation on $\not\!\!E_T$. The blue histogram shows preselected events; the yellow shows the effect of removing bad jets, and the red histogram is the cleaned sample after the track confirmation. 76
6.7 *a*) The η distribution of the unconfirmed jets: excess of data (dots) due to instrumental background in the calorimeter crack regions, *b*) The $\not\!\!H_T$ distribution: the SM (red histogram) does not describe data (dots) below 50 GeV. 77
6.8 Excess of data (dots) due to instrumental background for $\not\!\!E_T < 65$ GeV and $\Delta\phi(\not\!\!E_T, nearestjet) < 0.7$ rad regions: *a*) the $\not\!\!E_T$ distribution after the $\Delta\phi(\not\!\!E_T, nearestjet) > 0.7$ rad cut. *b*) The $\min(\Delta\phi(\not\!\!E_T, jet)$ distribution after $\not\!\!E_T > 65$ GeV. SM background is shown in red histograms and the leptoquark signal for M_{LQ}=150 GeV is shown in green histograms. 78
6.9 Comparison data (dots) and SM MC (red histograms) in the "no-QCD" point: *a*) the $\not\!\!E_T$ distribution, *b*) leading jet p_T, *c*) second leading jet p_T, *d*) leading muon p_T. For the leptoquark signal (M_{LQ}=150 GeV) these distributions are shown in green histograms. 79
6.10 a) Distributions of the X_{jj} variable, b) the E_T of the recoil jet. SM background is shown in grey histograms and the leptoquark signal for M_{LQ}=150 GeV is shown in green histograms. Also shown the contribution of the $W \to \mu\nu + jets$ background (red histograms) . . 81

6.11 Distributions of the isolation variables used for the suppression of the W background (red histograms). *a*) Sum of tracks p_T in a cone of 0.5 around the muon, *b*) Fraction of calorimeter energy around the muon direction in a 0.4 cone over a 0.6 cone (F_μ), *c*) $\Delta R \times p_T^\mu$ distribution. SM background is shown in grey histograms and the leptoquark signal for M_{LQ}=150 GeV is shown in green histograms. . 82
6.12 a) The $\not\!\!E_T$ and b) the jet multiplicity distributions after the muon tagging. SM background is shown in red histograms and the leptoquark signal for M_{LQ}=150 GeV is shown in green histograms. 84
6.13 The $\not\!\!E_T$ distribution after the muon- and b-tagging. The contribution of the W+two light jets background (red histogram) is small compare to W/Z($l\nu$)+$b\bar{b}$ and Top samples (grey histograms). The leptoquark signal for M_{LQ}=200 GeV is shown in green histogram. 89
6.14 The 95% CL limit on σB^2 (points plus solid line) as a function of M_{LQ} for the pair production of third generation leptoquarks. The theory band which includes PDF and the renormalization scale errors is shown in grey. The long-dashed line below the theory band indicates the threshold effect for the τt channel. Also shown are the expected 95% CL limits (points plus short-dashed line) 92
6.15 MU_JT25_L2M0 trigger (a) and MUJ2_JT25_LM3 trigger (b). Efficiency (left plot, red graph) as a function of the leading muon p_T measured with a missing H_T trigger and its parameterization (right plot, black graph) with the errors bounds (dotted lines). The efficiency as calculated with the TopTrigger package for the signal sample M_{LQ3}=150 GeV (left plot, blue graph) is shown for comparison. 95

CHAPTER 1
INTRODUCTION

Since the very first step of physics there have been two questions which scientists have been trying to answer through the centuries - what are the buildings blocks of matter and how do they interact with each other? This chapter describes the major discoveries in particle physics, the Standard Model theory (SM), and examples of theories beyond the SM.

1.1 Particle and Forces

1.1.1 The history of matter splitting

While the first recorded elementary particle or"atomic theory" is dated to the fifth-century C.E. (Democritus of Abdera, Greece) the term "elementary" earned its scientific definition only in 1808 with the work of John Dalton. He assigned it to identical atoms which form elements and postulated that atoms of one element could not be changed into atoms of another element "by any power we can control". But until the end of the 19th Century the most elementary objects of matter for the experimentalists were chemical elements. The constantly growing number of them (31 in 1800, 60 by 1860) and correlation of properties such as relative atomic weight and valence allowed chemist D.I. Mendeleev in 1869 to build the first successful classification of chemical elements and predict several new ones. In 1887

germanium was discovered with the predicted properties. Until the discovery of the electron by J.J Thomson in 1897 atoms kept their elementary status - in the first model of William Thomson in 1867 they were described as vortices of a liquid. As a legacy of such understanding the "pudding" model was proposed in 1903 - electrons are embedded in a positively charged sphere. Finally the scattering experiments of Ernest Rutherford (1911) proved the existence of atomic nuclei with electrons orbiting at large distances. The lightest hydrogen nuclei was called the proton (1920). Later in the 20th century the family of subatomic particles accumulated a number of a new members :

• Neutron (n), predicted by Rutherford in 1920, discovered by J. Chadwick in 1932

• Positron (e^+), 1932. the antiparticle of the electron.

• Muon (μ), 1936, similar to the electron, but heavier by a factor of 200.

• Neutrino (ν), 1956, predicted by W. Pauli.

• "Up" (u), "Down" (d) and "Strange" (s) Quarks, elementary blocks for neutrons, protons and strange particles. The quark model (1964, Gell-Mann and Zweig) allowed an explanation of unstable (lifetime 10^{-10} s) particles and resonances (lifetime 10^{-23} s) discovered in cosmic rays and accelerator experiments in the 1950s and 1960s as composed of "more" fundamental particles called quarks. Confirmed in deep inelastic scattering experiments at Stanford Linear Accelerator Center (SLAC) in 1968.

Three more quarks were discovered in later experiments : charm (c) - 1974 (simultaneously at Brookhaven National Laboratory and SLAC), bottom (b) - 1977(Fermilab), and top (t) - 1995 (DØ and CDF experiments, Fermi National Accelerator

Laboratory). The discovery of the tau-lepton in 1975 and its corresponding neutrino (2000) complemented the modern table of the "true" elementary particles (Table 1.1) with three generations of quarks and leptons.

Table 1.1: Generations of the quarks and leptons.

Generation	Quarks (mass in MeV)				Leptons (mass in MeV)			
1	u	(1.5 to 4)	d	(4 to 8)	e	0.511	ν_e	< 0.000003
2	c	(1150 to 1350)	s	(80 to 130)	μ	106	ν_μ	< 0.19
3	t	(174300±3400)	b	(4.1 to 4.4)	τ	1777	ν_τ	< 18.2

1.1.2 The basic forces and their carriers

The elementary particles interact with each other through four fundamental forces: gravitation, electromagnetism, weak nuclear interactions, and strong nuclear interactions. Special elementary particles serve as carriers for the corresponding force - the photon for the electromagnetic force, W and Z particles (discovered in 1983, at CERN) for the weak force, and the gluon (DESY, 1975) for the strong force. Gravity is not yet explained and its assigned mediator, the graviton, has not yet been found. A given particle can experience certain of these forces, but may be immune to others (Table 1.2). Gravity acts on all massive particles while the electromagnetic force is responsible for interactions between electrically charged particles. Quarks and gluons are the only particles which participate in strong

nuclear interactions, but quarks also participate in weak (together with all leptons) and electromagnetic (with charged leptons) interactions.

Table 1.2: Interactions and mediators.

Theory	Force	Carrier	Acts on
The	Weak	W^+, W^-, Z^0	Quarks and Leptons
Standard	Electromagnetic	Photon	Quarks, Charged Leptons
Model			and W^+, W^-
	Strong	Gluon	Quarks and Gluons
Not explained	Gravity	Graviton	All

1.1.3 Elementary particle classifications

Each elementary particle is associated with a set of properties like spin, electric or leptonic charge, and color. Spin, or the intrinsic angular momentum, is the initial discriminator in the classification. Particles which carry spin of $\pm 1/2, \pm 3/2, ...$ (fermions) are not allowed to occupy the same quantum state (the Pauli exclusion principle). The number of particles with integer spin (bosons) in a single state is not restricted. Quarks and leptons are fermions, while the force carriers are bosons. Positively charged fermions or bosons are defined as antiparticles to their negative charged twins with the same set of quantum numbers. Quarks and gluons carry color quantum number (eight possible types) but can only be observed in color-neutral particles called hadrons. Hadrons composed of quark-antiquark pairs are

mesons while baryons are hadrons consisting of quark triplets. Table 1.3 shows examples of mesons and baryons.

Table 1.3: Examples of baryons and mesons.

Symbol	Name	Quark content	Electric charge	Mass, GeV	Spin
		Barions qqq and Antibarions $\bar{q}\bar{q}\bar{q}$			
p	proton	uud	1	0.938	1/2
$\bar{p}$	antiproton	$\bar{u}\bar{u}\bar{d}$	-1	0.938	1/2
n	neutron	udd	0	0.940	1/2
Λ	lambda	uds	0	1.116	1/2
Ω^-	omega	sss	-1	1.672	3/2
		... About 120 types ...			
		Mesons $q\bar{q}$			
π^+	pion	$u\bar{d}$	+1	0.140	0
K^-	kaon	$s\bar{u}$	-1	0.494	0
$\rho+$	rho	$u\bar{d}$	+1	0.770	1
B^0	B-zero	$d\bar{b}$	0	5.279	0
η_c	eta-c	$c\bar{c}$	0	2.980	0
		... About 140 types ...			

1.2 The Standard Model

The efforts to describe data from particle accelerator experiments culmulated in creation of the modern theory of matter known as the Standard Model (SM) which is based on three renormalizable quantum gauge field theories in which each interaction is described by the associated symmetry group.

The transformations of local gauge symmetries are described by unitary $n \times n$ matrices, $U = e^{iH}$, $H^{\dagger} = H$ with real, space-time dependent elements. The matrices U form a group called $U(n)$ ($SU(n)$ if additionally $det(U) = 1$). $U(n)$ has n^2 parameters which "define" it (an example is electric charge for $U(1)$), while $SU(n)$ has $n^2 - 1$ parameters α_j and corresponding generators λ_j ($j = 1, n$). In quantized gauge theories gauge bosons are quanta of gauge fields. For a theory described by a $SU(n)$ symmetry the $n^2 - 1$ matrices correspond to gauge bosons.

The Standard Model is based on the combined group $SU_C(3) \times SU(2)_L \times U(1)_Y$. Indexes define the generator of the groups - quark color charge C, weak isospin L, and weak hypercharge Y. Quantum chromodynamic (QCD) [1], describing strong nuclear interactions, is based on the $SU_C(3)$ group and the electroweak theory [2] on the $SU(2)_L \times U(1)_Y$. Table 1.4 shows the forces and symmetries of the theories included in the SM.

1.2.1 QED and QCD

The first theory which became a model for subsequent gauge theories was quantum electrodynamic [3] (QED) with gauge group $U(1)_{Q_{EM}}$ where Q_{EM} is the electric charge. In the early 1940s, Tomonaga, Schwinger and Feynman developed

Table 1.4: Forces and symmetries of the theories included in the Standard Model.

	Gauge bosons	Gauge group	Details
EM force	Photon	The unbroken local $U(1)_{EM}$: invariance under the space-time dependent phase transition; generated by the electric charge	Photon is massless and neutral; couples to electric charge; force is infinite range; Theory - QED.
Weak nuclear force	$W^{\pm}$,Z	$SU(2)_L \times U(1)_Y$: invariance under space-time dependent rotations in 3D weak isospin space and under phase transitions generated by the weak hypercharge Y ($Q = I_3 + \frac{1}{2}Y$)	Gauge symmetry is hidden by interaction with Higgs particle; W and Z are massive, have weak and electric charge, short range
Strong nuclear force	eight Gluons	The unbroken local $SU_C(3)$: invariance under space-time dependent rotations in the 8-dimensional color space	Gluon is massless but self-interacting; charge is called quark color; Theory - QCD.

the ideas of P.A.M Dirac who first proposed a wave equation for a relativistic electron. Requiring the Dirac equation to be invariant under $U(\alpha) = 1 + iQ\delta\alpha(x)$ transformations leads to the electron-photon interaction and the existence of a massless photon. To calculate observable quantities, R. Feynman developed diagramming

techniques and implemented the renormalization procedure to eliminate divergent terms. The resulted prescriptions allowed the theory to obtain finite values for physical measurables.

The mathematical methods of QED later were adapted to the study of the strong interactions between quarks. Initially the existence of the color charges of quarks were inspired by the Δ^{++} discovery; in the quark model, this particle is composed of three up quarks with parallel spins. But quarks are fermions, and this combination is forbidden by the Pauli exclusion principle. To resolve this problem the 3 color charges together with their anticolors were proposed in 1965 by Moo-Young Han with Yoichiro Nambu and independently by Oscar W. Greenberg. With color charge the strong interaction between quarks is represented by the $SU(3)_C$ group: quarks are fundamental unit vectors in 3-dimensional color space and gluons correspond to a basis of eight $[3 \times 3]$ matrices which provide interactions. So all processes which occur in the theory can be resolved into the elementary interactions (represented by vertexes in Feynman diagrams): qqg, ggg and $gggg$. A quark may emit (or absorb) a gluon, a gluon may emit (or absorb) a gluon, and two gluons may directly interact. Mesons are colorless as combinations of color-anticolor quark pairs. Baryons are three quarks of different colors and so have no color as well.

The color charge of gluons intuitively explains the absence of free quarks (confinement in color-neutral hadrons). The gluon fields form narrow strings of color charge between quarks and thus the force experienced by the quark remains constant regardless of its distance from the other quark. Correspondingly, an infinite energy is required to separate two quarks.

The most important property of QCD is asymptotic freedom or very weak interactions between quarks and gluons within nucleons, such as the neutron or proton. They behave as free, non-interacting particles; this allows calculation of the cross sections of high-energy hadron reactions using pertubative techniques. That QCD predicts this behavior was first discovered in the early 1970s by David Politzer, Frank Wilczek, snd David Gross.

1.2.2 Electroweak Theory

The $SU(2)_L \times U(1)_Y$ part of the SM describing the electroweak theory is more complex as it needs the spontaneous symmetry breaking mechanism that explains the non-zero masses of the W^+, W^-, and Z^0 bosons proposed in the 1974 work of A. Salam, S. Weinberg, and S. Glashow. The $U(1)_Y$ symmetry corresponds to Quantum Electrodynamics, but the generator of the $U(1)_Y$ is the weak hypercharge Y, related to electric charge Q and the third component of isospin I_3 by $Y = 2Q - 2I_3$. The $SU(2)_L$ symmetry group corresponds to the weak nuclear interaction. It's generators are the three components of the weak isospin which can be symbolized by the Pauli matrices σ_i where

$$\sigma_1 = \begin{pmatrix} 0 & 1 \\ 1 & 0 \end{pmatrix}; \qquad \sigma_2 = \begin{pmatrix} 0 & -i \\ i & 0 \end{pmatrix}; \qquad \sigma_3 = \begin{pmatrix} 1 & 0 \\ 0 & -1 \end{pmatrix}, \quad i \equiv \sqrt{-1} \tag{1.1}$$

The index L in the $SU(2)_L$ notation reflects the fact that in the SM the left and right helicities are treated differently. Experimentally it was found that only right handed neutrinos are produced in $\pi^- \rightarrow \mu^- \bar{\nu_\mu}$ decay[4]. So helicity projections

$\psi_L = \frac{1}{2}(1-\gamma_5)\psi$ and $\psi_R = \frac{1}{2}(1+\gamma_5)\psi$ are needed where γ_5 is a Dirac matrix:

$$\gamma_5 = \begin{pmatrix} 0 & 1 \\ 1 & 0 \end{pmatrix}$$

Under the weak isospin $SU(2)$ the left-handed and right-handed helicities have different charges. The left-handed particles are weak-isospin doublets with $I_3 = \pm\frac{1}{2}$ (Table 1.5), whereas the right-handed are singlets ($I_3 = 0$). Electromagnetic

Table 1.5: Left-handed doublets under the symmetry group $SU(2)$.

$\psi_L = \frac{1}{2}(1-\gamma_5)\psi$			I_3	Q	L	B
Leptons						
$\begin{pmatrix}\nu_e\\ e\end{pmatrix}_L$	$\begin{pmatrix}\nu_\mu\\ \mu\end{pmatrix}_L$	$\begin{pmatrix}\nu_\tau\\ \tau\end{pmatrix}_L$	$+\frac{1}{2}$	0	$+1$	0
			$-\frac{1}{2}$	-1	$+1$	0
Quarks						
$\begin{pmatrix}u\\ d\end{pmatrix}_L$	$\begin{pmatrix}c\\ s\end{pmatrix}_L$	$\begin{pmatrix}t\\ b\end{pmatrix}_L$	$+\frac{1}{2}$	$+\frac{2}{3}$	0	$+\frac{1}{3}$
			$-\frac{1}{2}$	$-\frac{1}{3}$	0	$+\frac{1}{3}$

interactions are parity conserving and involve both left-handed and right-handed states of electrons. To unify it with parity violating weak interaction the common lepton and quarks states are assigned to a left-handed doublet and a right-handed

singlet. For leptons:

$$\psi_L = \frac{(1+\gamma_5)}{2}\begin{pmatrix}\nu_e\\ e^-\end{pmatrix}, \quad T=\frac{1}{2}, Y=-1 \tag{1.2}$$

$$\psi_R = \frac{(1-\gamma_5)}{2}\begin{pmatrix}e^-\end{pmatrix}, \quad T=0, Y=-2 \tag{1.3}$$

For quarks:

$$\psi_L = \frac{(1+\gamma_5)}{2}\begin{pmatrix}u\\ d\end{pmatrix} \tag{1.4}$$

$$\psi_R = u_R \ or \ d_R \tag{1.5}$$

The Weinberg-Salam theory unified weak and electromagnetic interactions at the interaction momentum transfer scale of $q^2 \sim M_W^2 = (100GeV)^2$. But the $SU(2)_L \times U(1)_Y$ group formalism requires three massless bosons W_μ^i (i=1,2,3) of the $SU(2)_L$ group and a massless isosinglet B_μ of the $U(1)_Y$. To be consistent with experiment a linear combination of the W^3 and B_μ is assigned to the Z^0 and another becomes the photon while two of the W^i become $W^\pm$. In the Standard Model this mechanism requires the introduction of a new massive, neutral, spin 0 particle known as the Higgs (H) boson. The Higgs boson remains the last unobserved particle in the SM theory.

1.3 Possible extensions of the Standard Model

The Standard Model allowes all describe existing experimental data. Its validity was shown by the discoveries of Ws, Z, quarks, and gluons. If the Higgs field is discovered the SM will be mathematically self-consistent. But even with a Higgs it will not be a complete theory. Unresolved problems include:

• masses of particles, gauge couplings, quark-mixing angles and a phase in the Cabibbo-Kobayashi-Maskawa (CKM) matrix are parameters of the model which are arbitrary chosen to satisfy experimental data

• no explanation of why there are three generanions of quarks and leptons

• the SM does not include gravity

The leading extensions of the Standard Model are the supersymmetric (SUSY) and the Grand Unification Theories (GUTs).

1.3.1 Grand Unified Theories

The aim of Grand Unified Theories is to construct a gauge group with a single coupling constant that describes all known SM interactions. This single coupling appears at the energy scale M_{GUT} (10^{18} GeV) where $SU(3)_C$, $SU(2)_L$ and $U(1)_Y$ couplings unite. The new gauge group contains $SU(3)_C \times SU(2)_L \times U(1)_Y$ as subgroups and has a symmetry which makes no distinction between quarks and leptons. The symmetry breaking down to SM subgroups is analogous to that already present in electroweak theory. The simplest variant of a GUT is based on the $SU(5)$ symmetry group. Leptons and quarks are combined into single representations:

$$\bar{\mathbf{5}} = (\bar{3}, 1) + (1, 2) = \bar{d}_c + (\nu_l, l^-) \tag{1.6}$$

$$\mathbf{10} = (\bar{3}, 1) + (3, 2) + (1, 1) = \bar{u}_c + (u_c, d_c) + l^+ \tag{1.7}$$

Gauge bosons belongs to the 24 adjoint representation

$$\mathbf{24} = (3, 2) + (\bar{3}, 2) + (8, 1) + (1, 3) + (1, 1) \tag{1.8}$$

The (3,2) + ($\bar{3}$,2) are 12 new superheavy gauge bosons X and Y with charges $\pm\frac{4}{3}$ and $\pm\frac{1}{3}$. This new bosons acquire masses by interaction with a 24-plet of Higgs bosons. The $SU(5)$ GUT predicts for the lifetime of the proton a value ruled out by experiments [5] (proton decay is possible as quark-lepton transitions are allowed and baryon and lepton numbers are not conserved any more). The theory was refined in [6] but the Super-Kamiokande experiment [7] excluded the predicted lifetime limit again. To overcome these weaknesses modern GUT theories include supersymmetry.

1.3.2 Supersymmetry

Supersymmetric theories postulate the existence of superpartners for each SM particle which would have the same quantum numbers except spin which would differ by $\frac{1}{2}$. Thus each SM fermion will have a boson as a superpartner and vice versa. SUSY theories also predict the existence of heavy weakly interacting stable particles which would be candidates to form dark matter. The simplest possible SUSY theory compatible with the SM is known as the Minimal Supersymmetric Standard Model (MSSM). There are also supersymmetric string GUT theories which include gravity [8] and so pretend to be called "Theories of Everything".

1.4 Search for new particles

SM extensions propose the existence of new particles some of which may be observed at existing detectors if they are not too heavy. A search described futher in this work set the limits on the mass of the leptoquark - scalar (spin 0) or vector (spin 1) bosons that have color, fractional electric charge, and lepton number. Among theories which predict such particles are the already mentioned SU(5) and SO(10) GUTs, and also the superstring E_6 models [9], R-parity violating Supersymmetry and Technicolor models.

CHAPTER 2
LEPTOQUARKS

As was mentioned in Chapter 1 a number of extended gauge theory models predict the existence of leptoquarks which unify SM leptons and quarks. The properties of the leptoquarks predicted by the subset of theories allowing leptoquark masses in the range achievable by the existing colliders as well as the results of previous experiments are described in this Chapter.

2.1 Leptoquark Phenomenology

The leptoquark states as described by the Buchmüller, Rückl and Wyler (BRW) model [10] assumes that leptoquark interactions respect the $SU(3)\times SU(2)\times U(1)$ symmetry of the Standard Model. Additionally, coupling to SM fermions and bosons only and the conservation of the lepton and baryon numbers to preserve the stability of a proton are required. Leptoquarks couple either to left-handed or to right-handed leptons and quarks (coupling to both type of electrons would mediate rare decays [11] which are not observed). If generation-changing leptoquarks are not considered then only 14 states (seven scalars and seven vectors) are allowed, assuming leptoquark mass degeneration within weak isospin doublets and triplets.

The so-called Aachen notation [12] is used in Table 2.1 for the description of these states. Leptoquark $Scalar(Vector)_i^{L,R}$ carries the fermion number $F = L+3B$

(0 or 2), isospin I (0,1/2,1) and fractional charge Q (ranges from -5/3 to +5/3). A tilde differentiates between leptoquarks that differ by two units of hypercharge. The branching fraction to a charged lepton β= (0, 1/2 or 1) shown is required in GUT models; for R-parity violating SUSY theories this is a free parameter. All leptoquarks listed in Table 2.1 are predicted by the SU(15) GUT model [13]

Table 2.1: Leptoquark classification according to the Buchmüller-Rückl-Wyler model.

Scalar Leptoquarks					Vector Leptoquarks			
LQ	Q	F	Decay	β	LQ	Q	F	Decay
S_0^L	-1/3	2	$l_L^- u_L$, $\nu_L d_L$	1/2	V_0^L	-2/3	0	$l_L^- \bar{d}_R$, $\nu_L \bar{u}_R$
S_0^R	-1/3	2	$l_R^- u_R$	1	V_0^R	-2/3	0	$l_R^- \bar{d}_L$
$\tilde{S}_0^R$	-4/3	2	$l_R^- d_R$	1	$\tilde{V}_0^R$	-5/3	0	$l_R^- \bar{u}_L$
$S_{1/2}^L$	-5/3	0	$l_L^- \bar{u}_L$	1	$V_{1/2}^L$	-4/3	2	$l_L^- d_R$
	-2/3	0	$\nu_L \bar{u}_L$	0		-1/3	2	$\nu_L d_R$
$S_{1/2}^R$	-5/3	0	$l_R^- \bar{u}_R$	1	$V_{1/2}^R$	-4/3	2	$l_R^- d_L$
	-2/3	0	$l_R^- \bar{d}_R$	1		-1/3	2	$l_R^- u_L$
$\tilde{S}_{1/2}^L$	-2/3	0	$l_L^- \bar{d}_L$	1	$\tilde{V}_{1/2}^L$	-1/3	2	$l_L^- u_R$
	+1/3	0	$\nu_L \bar{d}_L$	0		+2/3	2	$\nu_L u_R$
	-4/3	2	$l_L^- d_L$	1		-5/3	0	$l_L^- \bar{u}_R$
$\tilde{S}_1^L$	-1/3	2	$l_L^- u_L$, $\nu_L d_L$	1/2	$\tilde{V}_1^L$	-2/3	0	$l_L^- \bar{d}_R$, $\nu_L \bar{u}_R$
	+2/3	2	$\nu_L u_L$	0		+1/3	0	$\nu_L \bar{d}_R$

while other theories need only subsets of these states. An example is the light $\tilde{S}_{1/2}$ isodoublet introduced in refined $SU(5)$ GUT [14] to achieve better agreement with the experimental limit on the proton decay and the value of the Weinberg angle $sin^2\theta_w$. Vector state V_0 appears in the Pati-Salam model [15] while superstring E_6 theory predicts the S_0^L state.

2.2 Leptoquark searches at modern colliders

As leptoquarks have both electroweak and color charges they could be produced in strong and electroweak interactions at ee, ep, and pp colliders. Leading recent and current experiments are H1 and ZEUS at the Hadron-Electron Ring Accelerator (HERA) in Hamburg; OPAL, DELPHI, L3 and ALEPH at the Large Electron Positron Collider (LEP) at CERN; and DØ and CDF at the Fermilab Tevatron. In ee and pp collisions the dominant leptoquark pair production modes do not depend on the unknown Yukawa coupling λ of the $LQ-l-q$ interaction. That makes it possible to set direct limits on leptoquark masses of all three leptoquark generations. In ep collisions and in $e^{+/-}\gamma$ interactions the single leptoquark production cross-section is proportional to either λ or λ^2 and so requires an analyses of the (λ, M_{LQ}) plane. Single production modes restrict searches to first generation leptoquarks or requires coupling to the different fermion generation, like in the $e^+p \to \tau X$ channel. A review of searches presented in this section is based on [16], [17] and [18].

2.2.1 HERA anomaly

The first experimental results which suggested leptoquarks as a possible explanation for a disagreement with the SM prediction were reported by the H1 [19] and Zeus [20] collaborations based on the analysis of $e^{+/-}p$ collisions at HERA. The excess of events in neutral current deep inelastic scattering (DIS) data samples (Fig 2.1a) allows an interpretation of the processes in Figs. 2.1b and 2.1c which describe correspondingly the s-channel production and the u-channel exchange of leptoquarks. s-channel leptoquarks would form a resonance at $x = \frac{M_{LQ}^2}{s}$ (x is the fraction of nucleon momentum carried by the parton and s is the squared c.m. energy). The distribution of the events versus the cosine of the incident lepton scattering angle would be flat for scalar and $(1 - cos\theta^*)^2$ for vector leptoquark and is different then that of DIS. In 1997 seven events in the $M_{LQ} = 200 \pm 25$ GeV, $0.4 < y = \frac{1}{2}(1-cos(\theta^*) < 0.9$ window were found in H1 data with 0.95 expected, and four were observed in the $M > 220$ GeV, $y > 0.25$ box by ZEUS where 0.91+0.08 were expected. The studies (for example [21]) of this anomaly show that the fusion of a positron and a valence quark into a $F = 0$ leptoquark could explain the excess with the appropriate choice of the Yukawa coupling. However the analysis of data collected after 1997 did not confirm these results. For first generation leptoquarks with $\lambda = 0.1$ the lower mass limits are in the range of 250-280 GeV (ZEUS searches) depending on the leptoquark type.

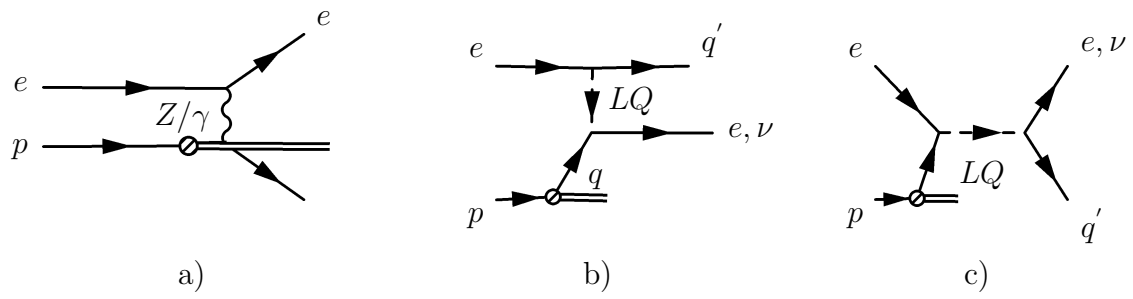

Figure 2.1: (a) neutral current deep inelastic scattering, (b) s-channel leptoquark production, and (c) u-channel leptoquark exchange.

2.2.2 LEP results

In e^+e^- collisions leptoquarks could be produced in pairs via electroweak couplings or singly via the interaction of an electron with a radiated photon [22]. The dominant single production contributions are from $\gamma \rightarrow q\bar{q}$ and the "resolved photon" processes. These diagrams are shown in Fig. 2.2. Combined leptoquark mass limits from the OPAL and DELPHI collaborations are in the range 165-917 GeV [17] for $\lambda = \sqrt{4\pi\alpha_{em}}$.

2.2.3 Hadron collider results

At hadron colliders like Fermilab's Tevatron, leptoquark pair production is nearly independent of the Yukawa coupling between the leptoquark and the lepton-quark pair. It arises primarily from quark-antiquark annihilation and gluon-gluon fusion; the leading order Feynman diagrams are shown in Fig 2.3. The contribution of the lepton exchange process (Fig 2.3b) is only about 1% of the total cross section

assuming an electromagnetic coupling strength $\sqrt{4\pi\alpha_{em}}$ for λ_{ql}. The lowest order (LO) cross section for scalar leptoquark pair production via the quark-antiquark annihilation subprocess is [23]:

$$\sigma_{LQ}(q\bar{q}) = \frac{2\pi\alpha_s^2}{27s}(1 - 4M_{LQ}^2/s)^{3/2}$$

where s is the squared center of mass energy.

The vector leptoquark pair production cross section in $q\bar{q}$ subprocess depends on the gVV coupling and additionally on quadratic $ggVV$ couplings if produced in gluon-gluon fusion. In models where vector leptoquarks are gauge bosons of an extended group these couplings are fixed (by gauge invariance), but in more complex

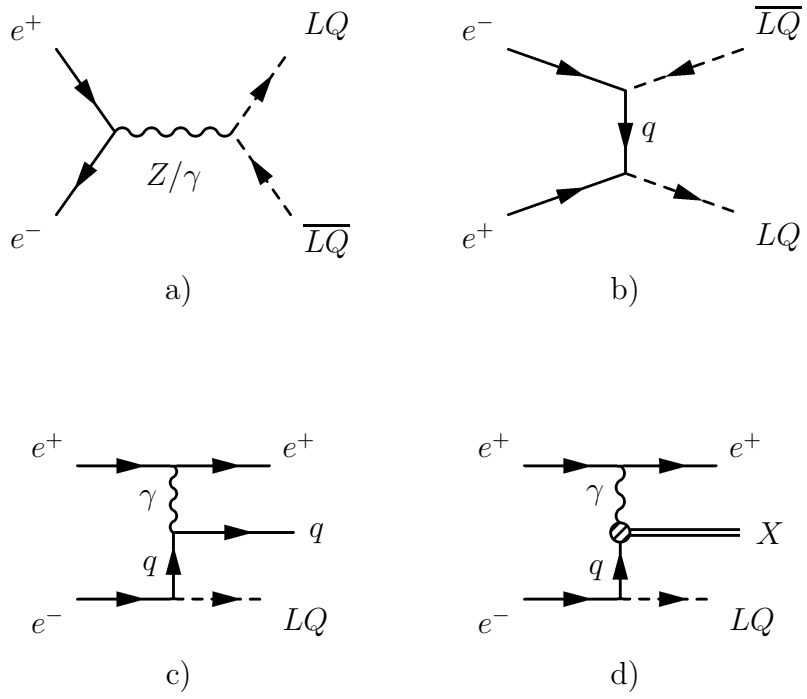

Figure 2.2: Leptoquark production at LEP: (a, b) pairs via γ^*/Z or q exchange, (c) single production dominant contributions $\gamma \to q\bar{q}$ and (d) "resolved photon" process.

theories the "anomalous magnetic and electric moments" couplings depending on k_G and λ_G parameters can appear in both gVV and $ggVV$ vertices. Two models are usually considered: Yang-Mills coupling (k_G=λ_G=0) and the minimal vector coupling (k_G=1, λ_G=0). These LO cross-sections are calculated in [24]. In $p\bar{p}$ collisions at $\sqrt{s}$ = 1.96 TeV quark-antiquark annihilation processes dominate the total cross section for leptoquark masses above 100 GeV (both for scalar and vector leptoquarks).

The final states for scalar leptoquark pairs and vector leptoquark pairs are identical and the experimental acceptances are similar. Each leptoquark decays into a lepton and a quark leading to three possible final states: $ll + jets$, $l\nu + jets$, and $\nu\nu + jets$, where l is a charged lepton and ν is its associated neutrino. The three final states appear with rates proportional to β^2, $2\beta(1-\beta)$, and $(1-\beta)^2$, respectively. Table 2.2 summarizes results of the D0 and CDF collaborations based on the analysis of the Tevatron Run I (1992-1996) data for all three leptoquark generations.

2.3 Third generation LQ searches at the Tevatron

The analyses in this paper set limits on the third generation leptoquark mass assuming they are scalar. The next-to-leading order pair production cross section is determined in [25]. The decay mode is defined by the leptoquark charge and mass. For charge $-\frac{1}{3}$ and $m_{LQ} > m_t + m_\tau$ it could be either $b\nu$ or $t\tau$. But if $m_{LQ} < m_t + m_\tau$, the branching ratio B (B $\equiv 1-\beta$) for $b\nu$ will be 1, and up to a

Table 2.2: Fermilab mass limits (scalar and vector leptoquarks).

Channel	β	Scalar	Vector		Comments
			Yang-Mills	MVb	
First Generation					
		213			CDF
$eejj$	1	225			D0
		242	340	290	Combined CDF/D0
$e(e/\nu)jj$	1/2	204	325	275	D0
$\nu\nu jj$	1	79	200	145	D0
Second Generation					
	1	202			CDF
$\mu\mu jj$	1/2	160			CDF
	1	200	325	277	D0
$\mu(\mu/\nu)jj$	1/2	180	310	260	D0
$\nu\nu jj$	1	79	205	160	D0
Third Generation					
$\tau\tau jj$	1	99	225	170	CDF
$\nu\nu b\bar{b}$	0	148	—	—	CDF
$\nu\nu b\bar{b}$	0	94	216	148	D0

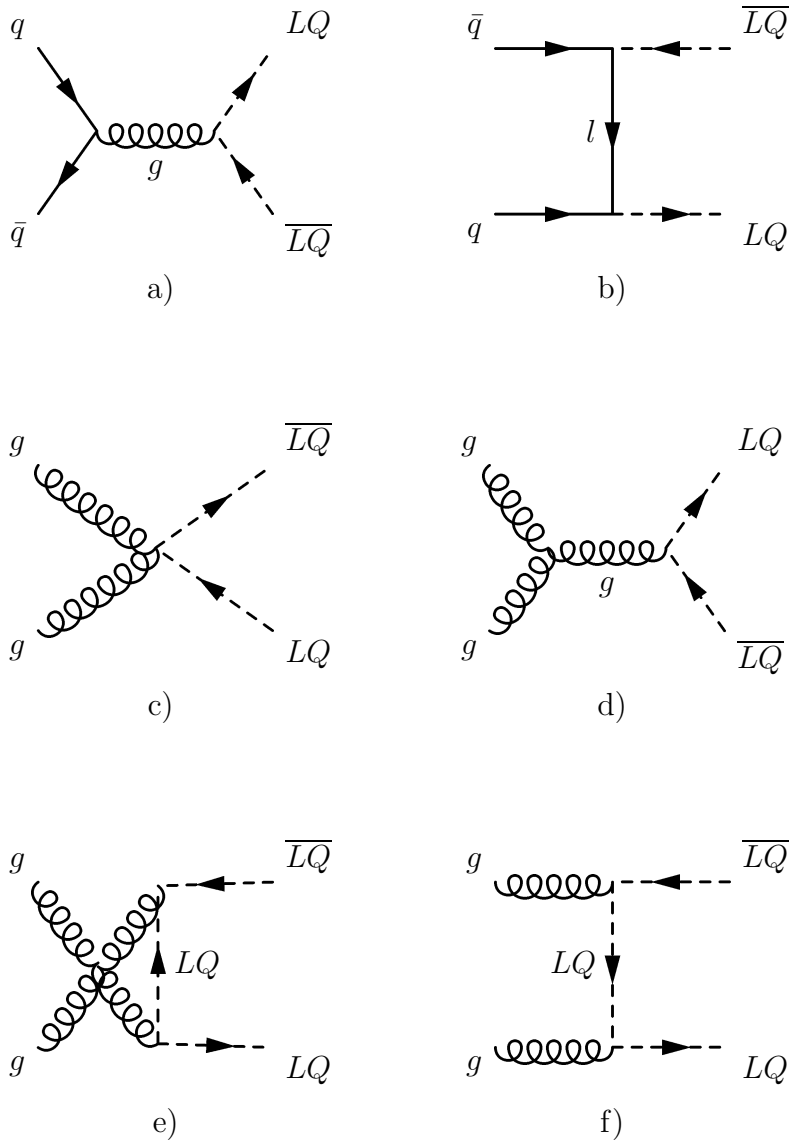

Figure 2.3: Leading order Feynman diagrams for leptoquark pair production at hadron colliders.

leptoquark mass of about 220 GeV phase space will suppress the decay into the top plus tau channel (the effect of this suppression is described in [26]). The charge $-\frac{4}{3}$

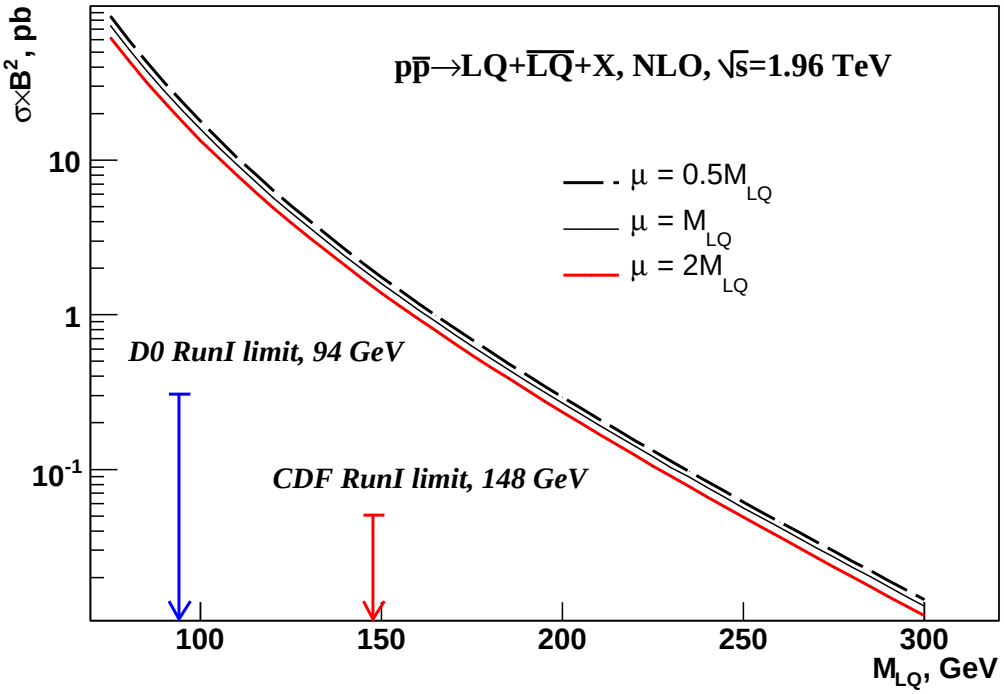

Figure 2.4: NLO Cross section for scalar leptoquark pair production [25]

LQ will give τb, and $-\frac{2}{3}$ will decay to $\tau\bar{b}$ or $\bar{t}\nu$.

The current limits on the LQ_3 mass established by the DØ and CDF collaborations based on the Fermilab Run I data are 94 GeV [26] and 148 GeV [27]. Both collaborations studied the $b\bar{b}\nu\bar{\nu}$ final state. DØ used the muon based criteria to tag b-jets: two muon-tagged jets with $p_T > 10$ GeV or one tagged jet with $p_T > 10$ GeV and a second jet with $p_T > 25$ GeV. CDF results were based on vertex tagging using a silicon detector. A CDF search in the $b\bar{b}\tau\bar{\tau}$ channel described in [28] gave a limit of 99 GeV.

CHAPTER 3
DØ DETECTOR AT THE FERMILAB TEVATRON

The DØ experiment was proposed in 1983 to study high mass states and large p_T phenomena in proton-antiproton collisions at the Fermilab Collider Complex (Tevatron, Fig. 3.1). Among the DØ results of the Tevatron Run I (1992-1996,

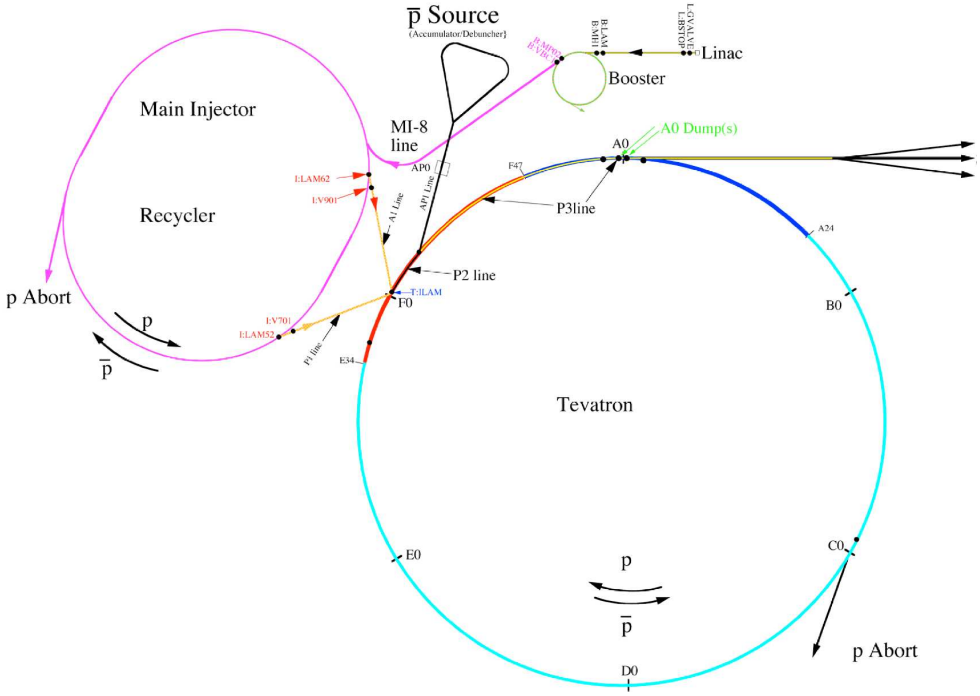

Figure 3.1: The Fermilab Collider Complex

a center-of-mass energy of 1.8 TeV, 125 pb^{-1} recorded data) are the discovery of

the top quark [29] and measurements of its mass and production cross-section, the precise determination of the W boson mass and the electroweak bosons couplings, studies of jet production and limits on the SM Higgs boson production. In searches for physics beyond the Standard Model, limits on leptoquark and supersymmetric particles were obtained for a large spectra of theoretical models. The full list of DØ publications can be found in [30].

During 1996-2001 both the Tevatron and the DØ detector were significantly upgraded [31]. In Run II (which started March 2001) the Fermilab collider operates at an increased center-of-mass energy of 1.96 TeV and at higher instantaneous luminosity. The DØ detector upgrade included new central tracking and new forward muon systems and an improved central muon system.

The analysis presented in this thesis sets limits on the production of charge 1/3 scalar leptoquark pairs decaying to the $b\bar{b}\nu\bar{\nu}$ final state by analyzing Run II DØ data recorded between August 2002 and September 2004. We have analyzed a data sample triggered by muons and jets. To extract a possible leptoquark signal from SM backgrounds (W/Z+jets, top decays) we tag jets by applying strong requirements on an associated muon. We then use impact parameter b-tagging to improve the cleanliness of the signal selection. This Chapter describes the subsystems of the DØ detector which are most important for this analysis.

3.1 The DØ detector

The detector consists of three major subsystems: central tracking detectors, uranium/liquid-argon calorimeters, and a muon spectrometer. In the detector description and in data analysis, a right-handed coordinate system will be used in which the z-axis is along the proton direction and the y-axis is upward. The angles ϕ and θ are, respectively, the azimuthal and polar angles. For the description of a polar direction we will often use the pseudorapidity, η, which is related to polar angle by $\eta = -\ln[\tan(\theta/2)]$ The term "forward" describes the regions at large $|\eta|$. The r coordinate denotes the perpendicular distance from the z axis.

The central tracking system includes a silicon microstrip tracker (SMT) and a scintillating fiber tracker (CFT) located within a 2 T superconducting solenoidal magnet. The silicon microstrip tracker is able to identify displaced vertexes for b-quark tagging at pseudorapidity $|\eta| < 3$. The CFT system allows tracking in the $|\eta| < 2.5$ region.

The central, $|\eta| < 1.1$, and two end calorimeters provide coverage up to $|\eta| \simeq |4|$. Preshower detectors are located between the solenoidal magnet and the central calorimeter and in front of the forward calorimeters to improve electron identification and the measurement of jet energies and the total missing transverse energy ($\not\!\!E_T$). $\not\!\!E_T$ is is determined by the vector sum of the transverse componets of the energy deposited in the calorimeter and the p_T of detected muons.

The muon system resides beyond the calorimetry. It consist of three similar layers of tracking detectors and scintillation trigger counters with one layer located before the 1.8 T muon toroid magnets and two layers outside the toroids. In the

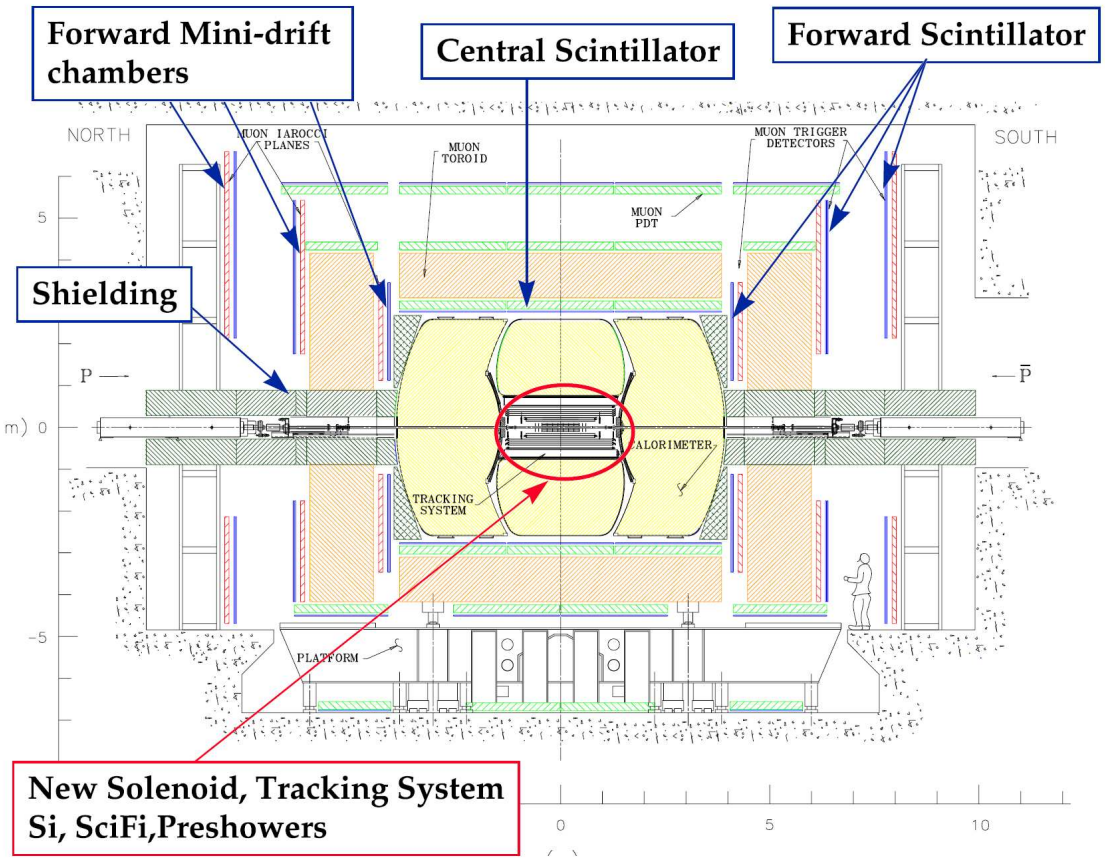

Figure 3.2: The DØ Detector

$|\eta| < 1$ region muon tracking is provided by 10 cm wide drift tubes and 1 cm mini-drift tubes are used for $1 < |\eta| < 2$. A side view of the DØ detector is shown in Fig. 3.2.

3.1.1 The central tracking system

Precise tracking in the central region is necessary for the leptoquark search in the $b\bar{b}\nu\bar{\nu}$ final state as it measures the impact parameter used to tag b-jet candidates.

The central tracking system consists of the silicon microstrip tracker (SMT) and the central fiber tracker (CFT) surrounded by a solenoidal magnet. The two tracking detectors locate the primary interaction vertex with a resolution of about 35 μm along the beamline. They can tag b-quark jets with an impact parameter resolution of better than 15 μm in $r-\phi$ for particles with transverse momentum $p_T > 10$ GeV at $|\eta| = 0$. The high resolution of the vertex position allows good measurement of lepton p_T, jet transverse energy, and missing transverse energy. A schematic view of the central tracking system is shown in Figure 3.3.

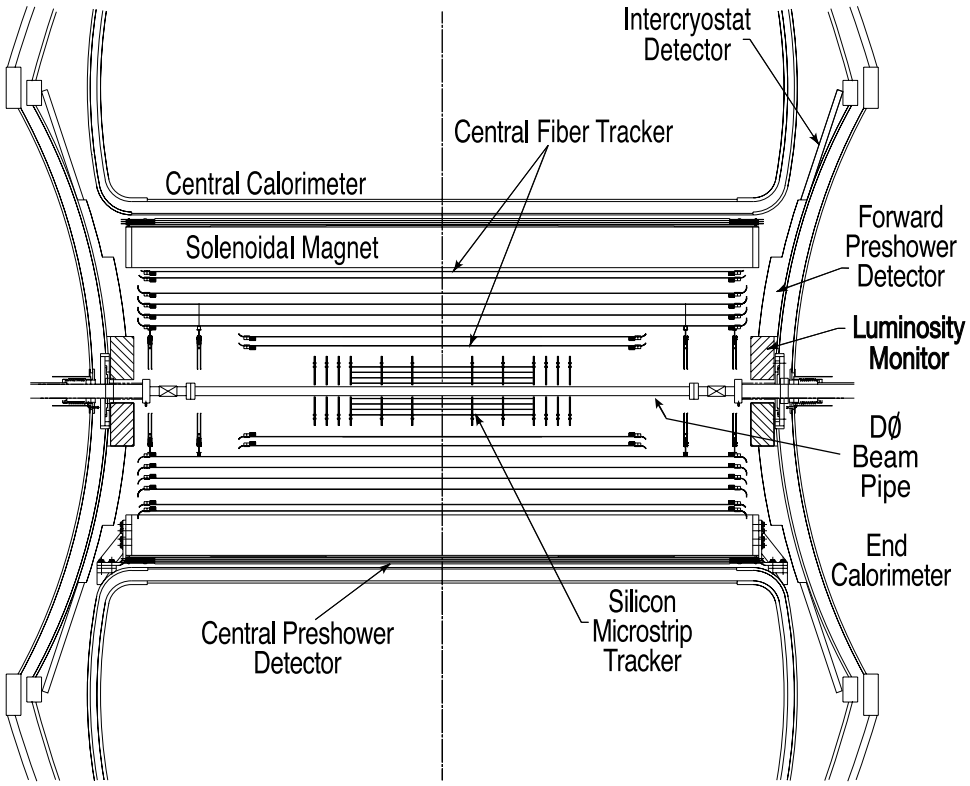

Figure 3.3: The DØ Central Tracker

The SMT provides both tracking and vertexing over nearly the full η coverage of the calorimeter and muon systems. It surrounds the interaction region ($\sigma(z) \approx$ 25 cm). The detector consist of six barrel modules interspersed with disks in the center and assemblies of larger diameter disks in the forward regions. Layers on silicon microstrip modules reside on this structure providing about 790000 readout channels. The barrel detectors primarily measure the $r - \phi$ coordinate and the disk detectors measure $r - z$ as well as $r - \phi$. Thus vertices for particles at high η are reconstructed in three dimensions by the disks, and vertices of particles at small values of η are measured in the barrels and central fiber tracker. Depending on η the detector resolution $\sigma(r)$ of the primary and secondary vertex reconstruction is 15-35 μm while the secondary vertices resolution in the z-direction is 80 μm [32]. An isometric view of the SMT is shown in Fig. 3.4. More details about the detector can be found in [33].

The CFT detector [34] consists of ≈77000 scintillating fibers of diameter 835 μm mounted on eight concentric support cylinders (Fig. 3.5). It occupies the radial space from 20 to 52 cm from the beam axis. The outer cylinder covers the $|\eta|$ region up to ≈ 1.7. Each cylinder supports one doublet layer of fibers oriented along the beam direction (z) and a second doublet layer at ϕ angle of $+3^\circ$ or -3° to the z-axis to provide stereo information about tracks along z. The scintillating fibers are optically connected to photodetectors, which are silicon avalanche devices capable of detecting single photons and provide a gain up to 65000. The combined SMT/CFT momentum resolution $\Delta P_t/P_t^2 = 0.002$ GeV^{-1} [32].

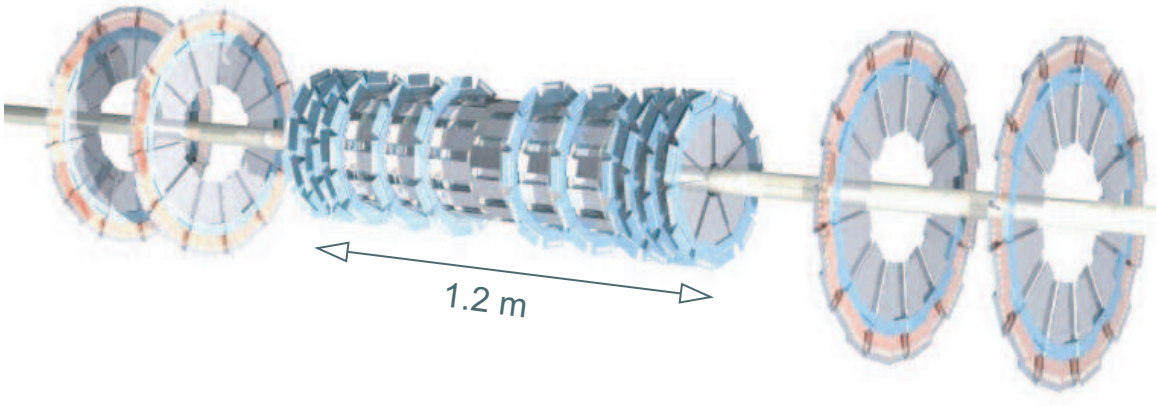

Figure 3.4: The DØ silicon microstrip tracker.

Figure 3.5: The fiber tracker detector, shown from the direction of the beam pipe.

3.1.2 The calorimeter system

In this analysis the calorimeter was used for the reconstructruction of jet energy, missing energy, and for associating jets with muon candidates from b-quark decays. The calorimeters detailed description can be found in [35]. The devices were not changed (except for some of the electronics) since Run I data taking when it played the most important role in the DØ experiment. In Run II the new tracker system made possible an improved calibration of the electromagnetic calorimeter using electrons from $p\bar{p}$ collisions.

Figure 3.6 illustrates the design of the calorimeter system. The central calorimeter covers $|\eta| \lesssim 1$, the north and south end calorimeters extend coverage to $|\eta| \approx 4$. The electromagnetic sections are located closest to the interaction region, then the fine and the coarse hadronic parts. In all section liquid argon is used as the active medium and the passive layers are made from uranium (electromagnetic and fine hadronic sections) and copper or stainless steel (central and forward coarse hadronic modules).

The longitional subdivision is used to differentiate between electromagnetic and hadronic showers. The fine granulation (0.1 x 0.1) in the $\eta - \phi$ plane is matched to the typical size of the parton jets, $\Delta R = \sqrt{\Delta\eta^2 + \Delta\phi^2} \sim 0.5$

3.1.3 The muon system

The muon system provides the possibility of b-jet tagging by using jet associated muons. In the present analysis, which is based on muon plus jet triggered data, it shares a key position with the calorimeter and the central tracking systems.

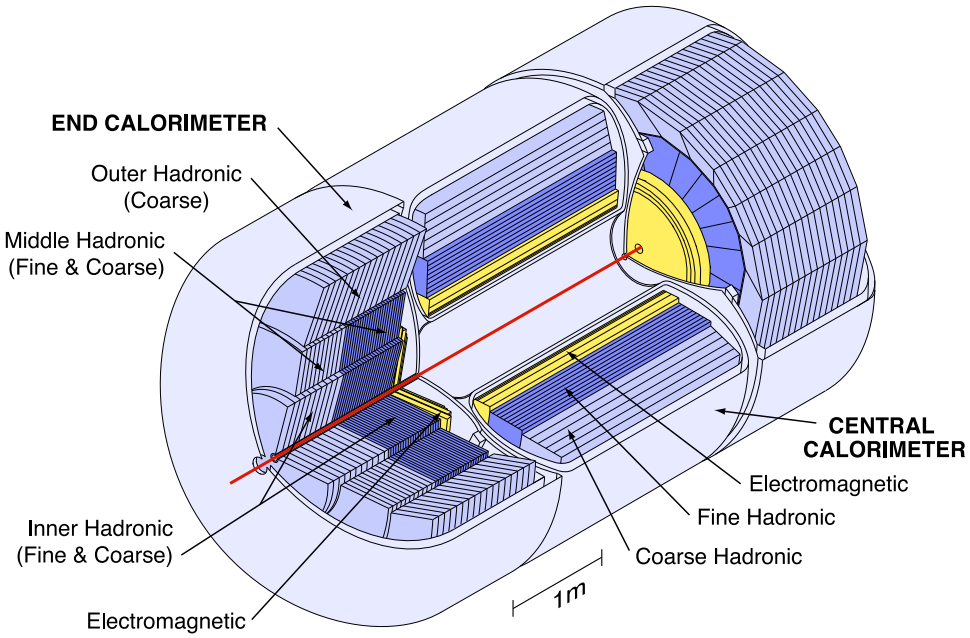

Figure 3.6: Isometric view of the central and two end calorimeters.

The muon triggering and tracking is performed using information from the scintillator counters, proportional drift tubes (PDTs), and mini-drift tubes (MDT). The presence of 1.8 T toroidal magnets allows stand-alone muon momentum measurement. The muon system is divided into central [36] ($|\eta| \lesssim 1.0$) and forward [37] (up to $|\eta| \approx 2.0$) parts which surround the calorimeters. Exploded views of the muon wire chambers and scintillation detectors are shown in Fig. 3.7 and Fig. 3.8.

The central muon system includes three layers (A, B and C) of PDTs and scintillator counters, the A layer between the calorimeter and toroid and the B and C layers after it. The outer layer of scintillators is installed on the top and bottom and sides of the detector. The timing information from these trigger counters are used to reduce the cosmic ray background. The layer of the scintillators located

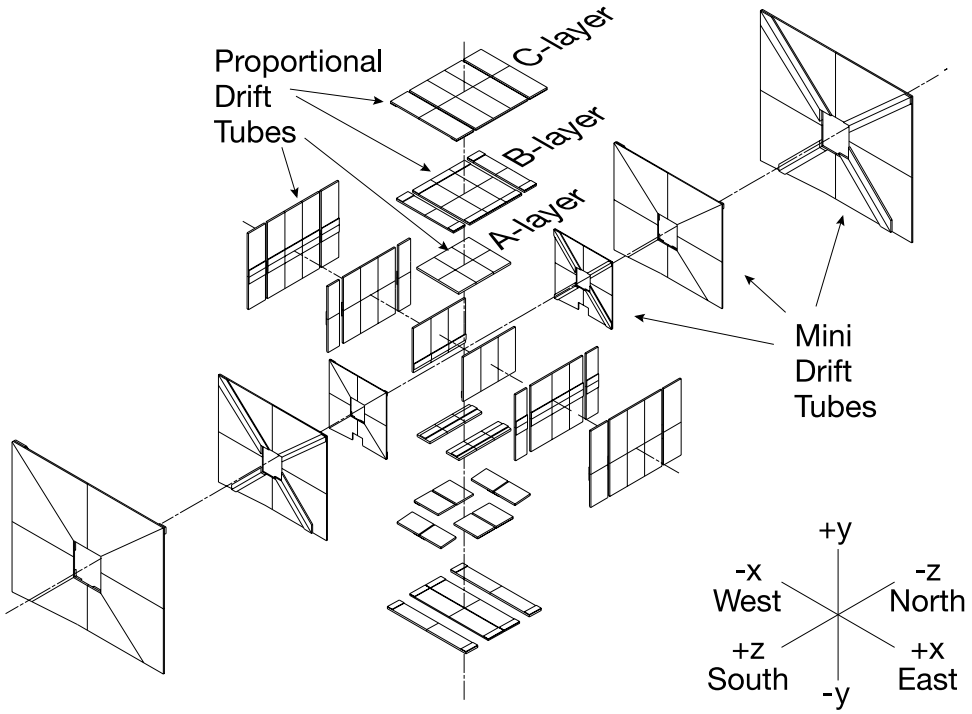

Figure 3.7: Exploded view of the muon wire chambers.

between the calorimeter and the magnet provide a fast detector for triggering and identifying muons and for rejecting out-of-time background events.

The PDT cells, combined in 94 PDT chambers, are used for building three dimensional segments of the muon tracks. Each chamber in the A layer has four layers (except for the bottom where three layer chambers are installed) of drift tubes with anode wires oriented parallel to the toroid magnetic field with each cell having $\sim$1 mm drift distance resolution. The chambers in the B and C layers have three layers of cells.

The north and south forward muon systems have a similar structure. Four

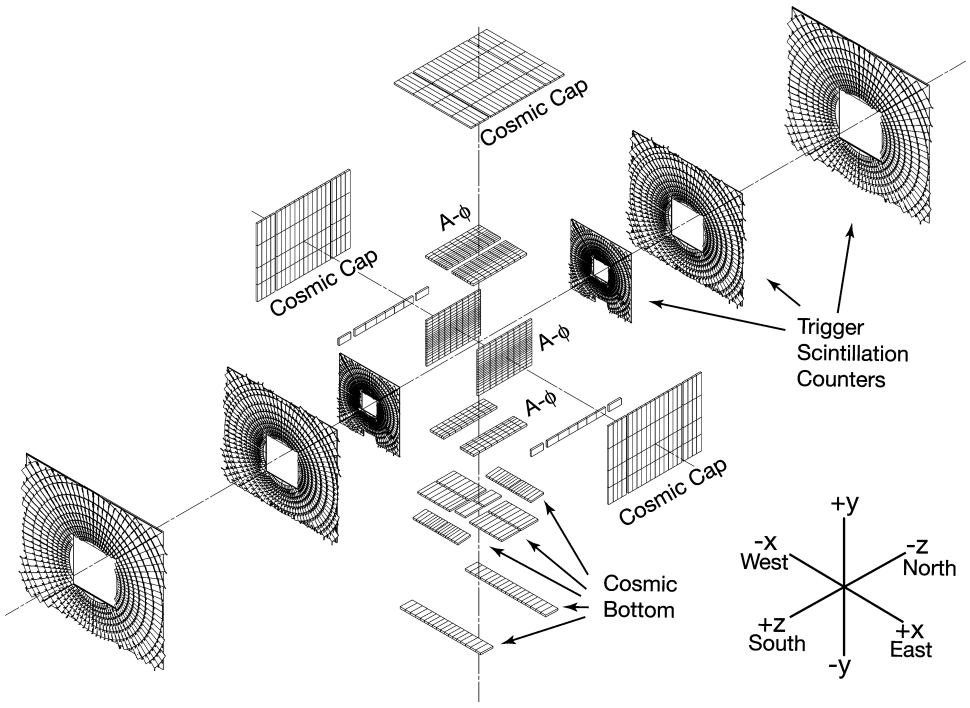

Figure 3.8: Exploded view of the muon scintillation detectors.

planes of mini-drift tubes associated with a layer of the pixel scintillator counters form the system A layer located before the forward toroid. The B and C layers located outside the toroid and include three planes of mini-drift tubes each. The mini-drift tubes have a resolution of $\sim$0.7 mm.

The muon system alone has lower momentum resolution ($\sigma(p_t)/p_t \sim 0.18 \bigoplus .03p$) in comparison with the central tracker due to multiple scattering. So the momentum measured by the central tracking system is assigned to a muon candidate when it matches a central track.

3.2 The luminosity monitor detector

The Tevatron luminosity $\mathcal{L}$ at the the DØ interaction region is extracted from the average number of inelastic collisions per beam crossing, $\bar{N}_{LM}$, measured by the luminosity monitor detector (LM). It is defined as $\mathcal{L} = f\frac{\bar{N}_{LM}}{\sigma_{LM}}$, f is the beam crossing frequency and σ_{LM} is the effective cross section for the LM, which is determined as described in [38]. The LM detector is shown on Fig. 3.9. It consist of two arrays of twenty-four plastic scintillation counters located in front of the end calorimeters at $z = \pm 140$ cm. In the radial direction, it resides between the beam pipe and the forward preshower detector, covering the pseudorapidity range $2.7 < |\eta| < 4.4$. The $p\overline{p}$ interactions are separated from the beam halo using the difference in the time-of-flight for particles which hit the opposite wings of the LM detector.

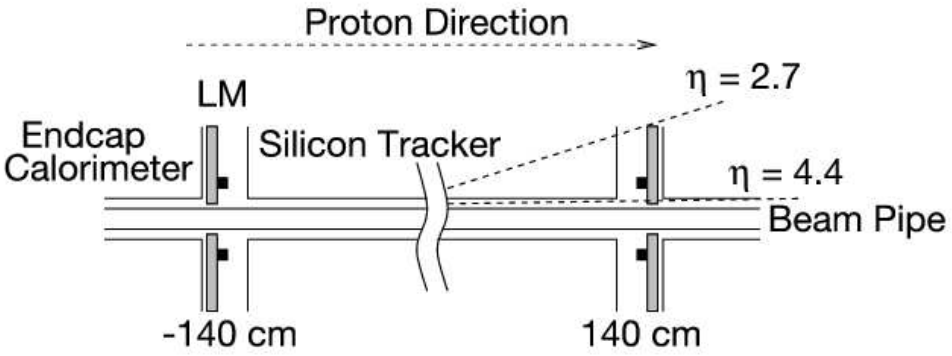

Figure 3.9: The location of the LM detectors.

The fundamental unit of time used for luminosity measurement is defined as the luminosity block. During this (short) time the instantaneous luminosity is effectively constant. The luminosity averaged over the luminosity block is associated

with a unique index - the luminosity block number (LBN). The integrated luminosity used in the data analyses is calculated as the sum over all LBN blocks for which data is considered good. Figure 3.10 shows the collider Run II integrated luminosity. The luminosity used for the present leptoquark analysis was accumulated between August 2002 and September 2004 (red arrows).

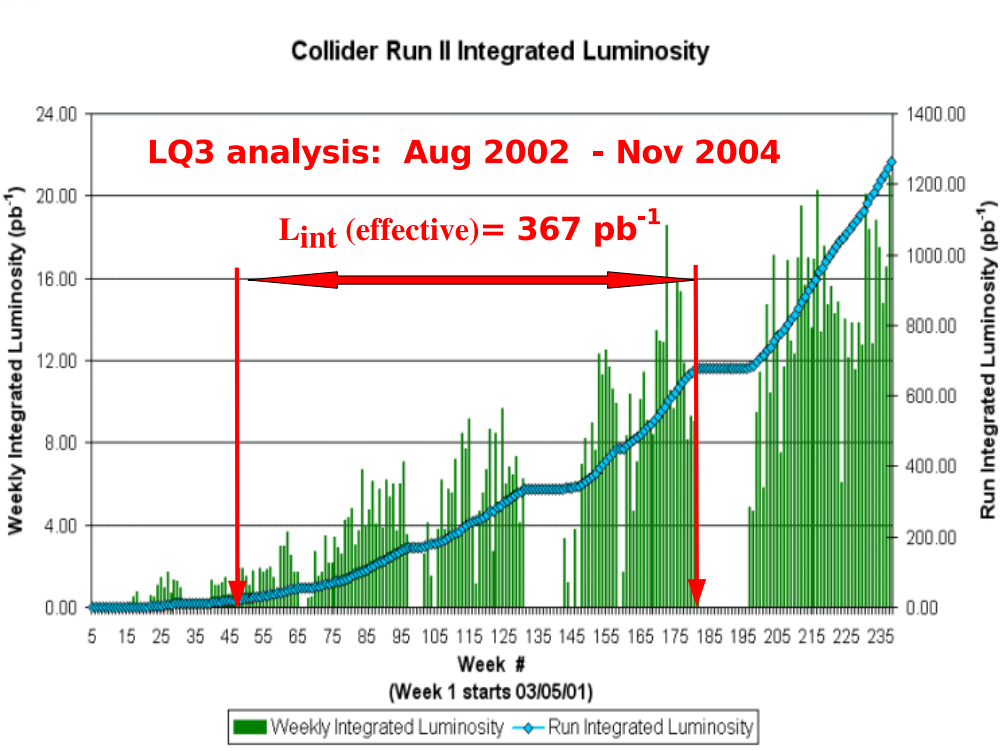

Figure 3.10: The Tevatron Run II integrated luminosity.

CHAPTER 4
THE LEVEL-2 MUON TRIGGER OF THE DØ DETECTOR

The DØ Trigger system is based on three levels of rejection. The second level ("L2") is the first which makes trigger decisions based on physics objects from all detector subsystems. This Chapter is focused on the L2 muon trigger whose performance is critical for a search based on muon plus jet triggered data.

4.1 The DØ data acquisition system

Figure 4.1 illustrates the structure of the DØ trigger and data acquisition system. Three succesive triggering levels (L1, L2, and L3) are used for event selection, decreasing the initial data rate of 1.7 MHz to 50 Hz at which events are recorded for the offline reconstruction. L1 uses hardware elements. The L2 stage uses software running on fast processors optimized for parallel event processing for a more complex analysis. More sophisticated algorithms run at the L3 microprocessor farm. Deadtime is minimized by using L1 and L2 memory buffers to provide storage for the events awaiting a L2 decision or a transfer to L3.

The trigger framework gathers digital information from each of the specific L1 trigger elements and chooses whether a particular event is to be accepted for further examination. It also coordinates various vetoes that can inhibit triggers, provides the prescaling of triggers, correlates the trigger and readout functions, manages the communication tasks with the front-end electronics and the trigger

control computer, and provides accounting of trigger rates and deadtimes.

The overall coordination and control of DØ triggering is handled by the COOR package that interacts directly with the trigger framework for L1 and L2 triggers and with the data acquisition (DAQ) supervising systems for the L3 triggers.

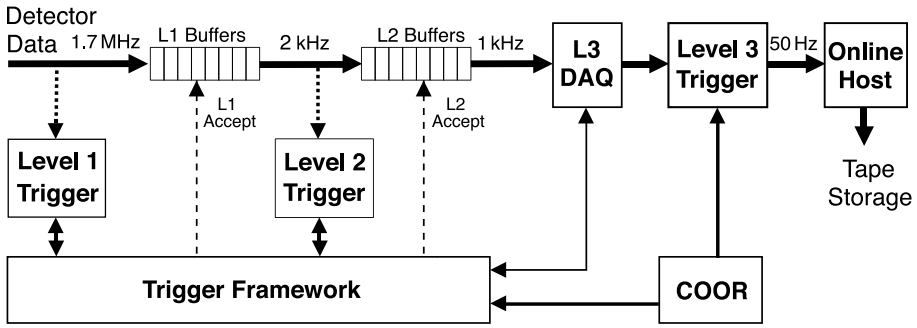

Figure 4.1: The DØ Trigger System

4.2 The Level-2 Trigger System

The L2 trigger system was designed to handle input rates of up to 10 kHz with a maximum accept rate of 1 kHz. The L2 trigger provides detector-specific preprocessing engines and a global stage (L2Global) to test for correlations in physics signatures across detector subsystems. As shown in Fig. 4.2, preprocessors collect data from the front-ends and L1 trigger system and analyze these data to form physics objects: jets, electons, gammas, missing energy, muons, tracks and track impact parameters[1].

[1]The impact parameter is the shortest distance between the track and the assumed interaction vertex in the $r\phi$ plane [39].

The L2Global is the first DAQ stage with access to all detector elements. It can request object matches and improve object ID. It provides angular separation, invariant masses, lepton isolation, CFT track match, STT impact parameter and makes its final trigger decision based on the set of 128 selections applied at L1 and additional programmable criteria. Events passing L2 are tagged for full readout and further analysis is performed in the L3 trigger.

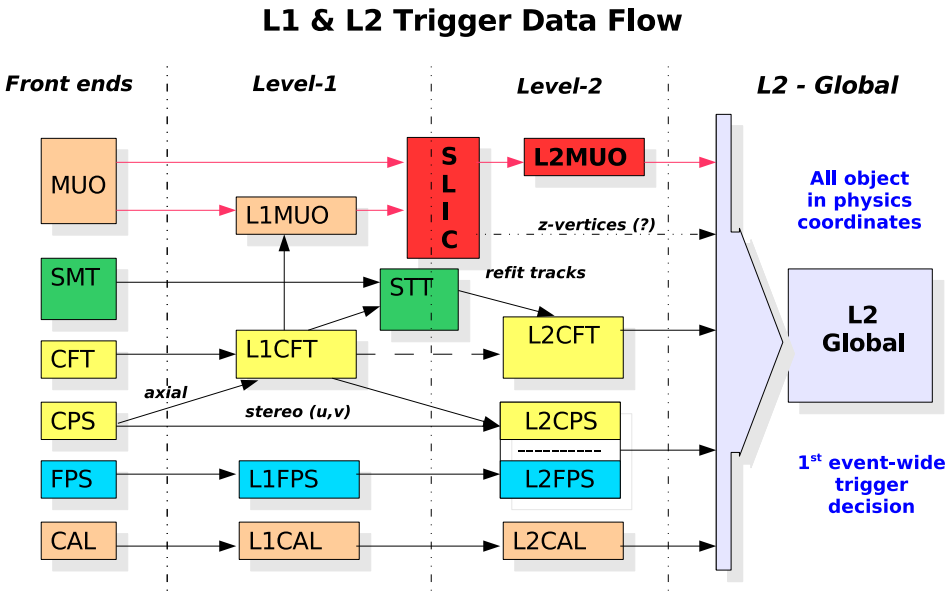

Figure 4.2: Block diagram of the dataflow from the detector front-end systems to the L2 global decision

4.3 The Level-2 Muon Trigger

The L2 muon track finding is done independently of the L1 results. Due to the large number of front end inputs, the L2 muon subsystem implements one extra level of preprocessing compared to all other L2 subsystems. The muon detectors send specially preformatted data to the "Level-1.5" system of eighty 200-MHz processors (DSPs) in a parallel processing scheme.

Each DSP is responsible for finding track segments in a small region of the detector so that the total execution time of the algorithms is independent of the number of hits. The DSPs run on special VME boards (second level input computers or SLICs). Each SLIC carries five DSP chips; four worker DSPs and one administrator DSP. Eleven SLICs process data from the central muon system and five from the forward muon system.

Five different algorithms were developed to run on worker DSPs: four to construct muon segments in the A and BC layers of the central or forward muon systems and one to process the L1 data. These segment finding algorithms provide 3D segment reconstruction using the single detector element hits and improves muon identification and rejection over L1 whose candidates are based on wide 2D hodoscopic road matches. At the second stage the segments found by the SLICs are received by the L2beta processor. The L2beta board uses the track segments to construct integrated muon candidates with an associated p_T and quality evaluation and sends them to the global L2 for event selection. A block diagram of the L2 muon data processing sequence is shown in Fig. 4.3. The SLICs algorithms for the forward muon system are described in detail in references [40] and [41]. In the

next section the central muon triggering will be described (more information can be found in [42],[43],[44] and [45]).

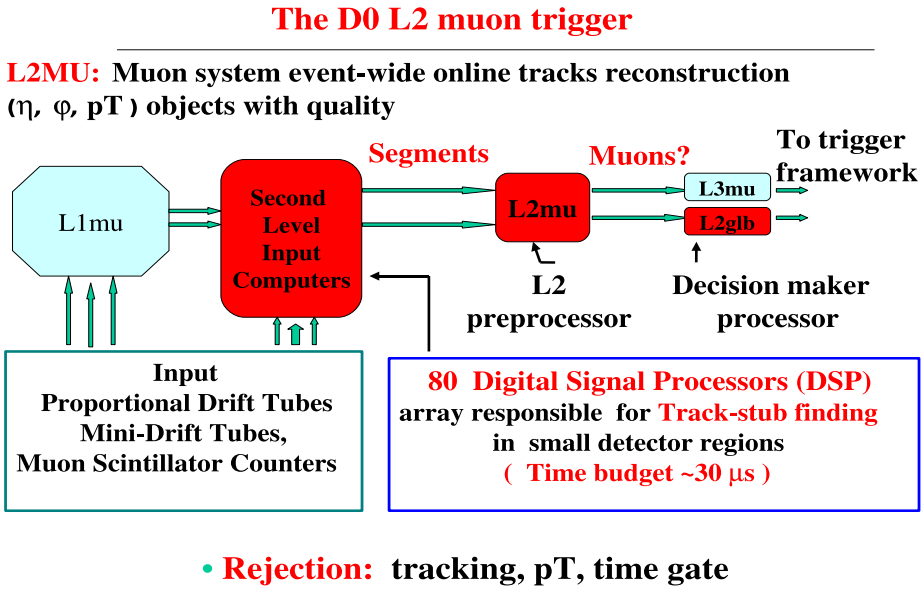

Figure 4.3: Data processing in the Level-2 muon trigger system. Two stages of processing are completed in a single crate using SLICs and L2beta processors. Central and forward muon regions are processed in separate crates of similar configuration.

4.3.1 The segment finding algorithms

There are 40 worker DSPs (each has 64K program memory and 64K RAM) that provide track segment finding in the central region of the D0 muon system. These processors are located on ten SLIC boards with four in each. Two boards get input from A-layer proportional drift chambers and scintillator counters and

the other eight serve B- and C-layers. Accordingly, DSP algorithms have two basic flavors - A or BC. The A-layer algorithms deal with data coming from one full octant and the corresponding code runs on a dedicated DSP. Data from one BC octant is divided between four DSPs (as shown in Fig 4.4) located on one SLIC board. There is in overlap in data between neighboring DSPs but in each octant DSP1 and DSP3 searches segments with negative rz-slope while DSP0 and DSP2 searches segments with rz-slope>0. There are minor differences inside both algorithms flavors due to reflecting muon system geometry (for example, the central bottom chambers are different from the side and top).

To find proper segments all algorithms use pregenerated (unique for each detector region) look-up tables (LUTs). Each tabulated segment is derived from the DØ simulation package (D0GSTAR) by transporting through the detector single muons in the p_T range 2-15 GeV coming from the interaction point with $\sigma(z)$ =30 cm. These segments have a mean η (obtained from their parent generated tracks) in the A-layer or a mean "deflection", or slope of the track, in the case of BC segments. The segment ϕ is defined by the geometrical position of the scintillator if an associated hit is found. In the case of a wire only segment, ϕ is defined as the middle of the corresponding octant. In the first case the scintillator hit time is also assigned with the segment. There are no scintillator-only L2 muon candidates. Depending on the number of hits in the drift chambers and scintillators a quality (three possible gradations) is also assigned to the segment. So each algorithm does three basic steps: constructs segments from the data, checks if it is present in the look-up tables, and in the case of success, reports a vector (η, deflection, ϕ, quality, time) to

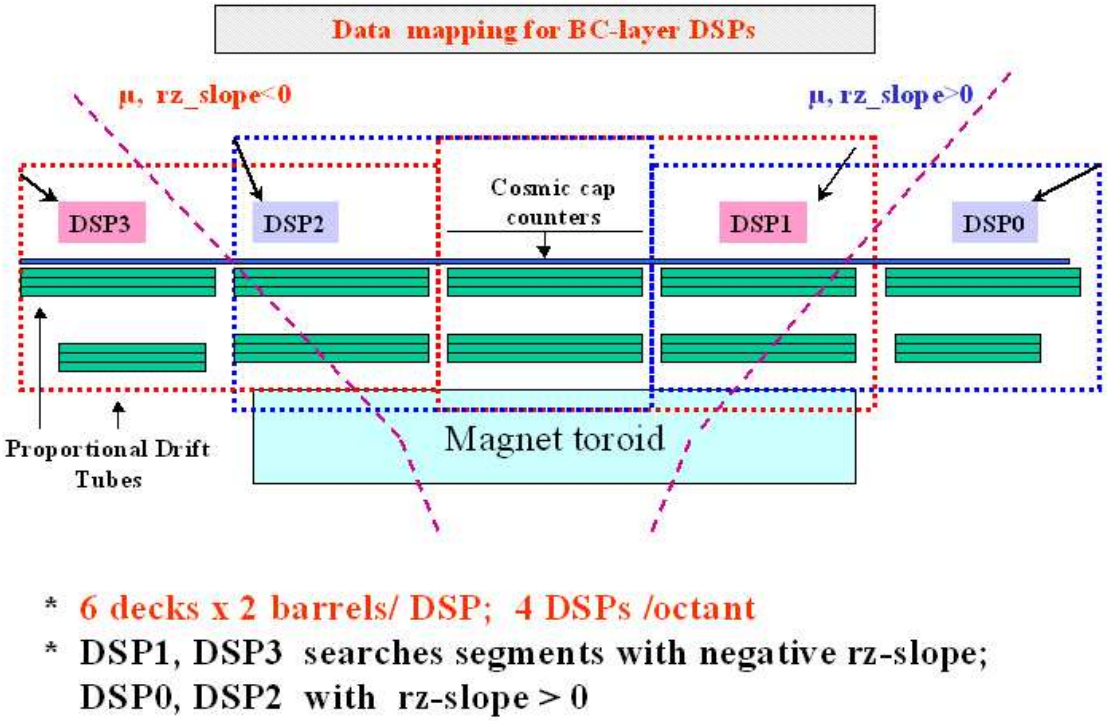

Figure 4.4: Muon detector structure associated with a central BC-layer octant and its division between processing DSPs.

the track reconstruction part of the L2 muon trigger. Code development included two distinct topics:

• Tables: table-making only runs offline, with emphasis on accuracy, efficiency(fast access), and small size. LUTs reside in the DSP auxiliary memory, an external SBSRAM chip with 128KB.

• Tracking: Track finding and fitting runs online, with an average time budget limited to about 30 μs.

Track segment finding starts from clusters of hits in drift chambers. The

chambers are treated as grids with stacked decks of drift cells (wires run along ϕ and cover one octant), each deck with 24 cells. The four-deck chambers in the A-layer form 24-column grids of 96 cells, three-deck B, C and bottom A-layer chambers form 72 cell (3×24) grids. Grid representation allows the definition of a DSP "hyperchamber" which includes PDTs providing input for this processor. In the A layer it covers three PDTs in z and one octant in ϕ, with a 72 column × 4 deck structure. The numbering scheme for cells follows the electronics addressing [46], and is shown in Fig. 4.5 together with the numbering of columns and decks (columns 0...23 – column 0 contains cell 0; decks 0...3 ordered 0=innermost, 3=outermost; bottom PDTs have three decks only but the numbering rules are preserved). In the B- and C-layers the two 48x3 hypercharmbers are constructed for each worker DSP as shown in Fig. 4.6.

Muon track simulation shows that muons from the interaction region can not hit more then three neighboring columns. This defines an inspection window, 3 column × 4(3) deck region of each hyperchamber. Cells inside a window are reassigned local numbers from 0 to 11(9) and thus can be treated as a hit masks (one bit to each cell hit).

Window hit masks are basic objects of the segment finding algorithms. An inspection window is swept through a hyperchamber and all hit mask that are found are compared to a look-up table. LUTs are the repository of all valid combinations of hit cells in each window of a specific hyperchamber (or DSP geometry domain).

In the A-layer the table entry for a valid hit mask search is the column index of its innermost hit. This index (col_i) plays a key role in the construction and

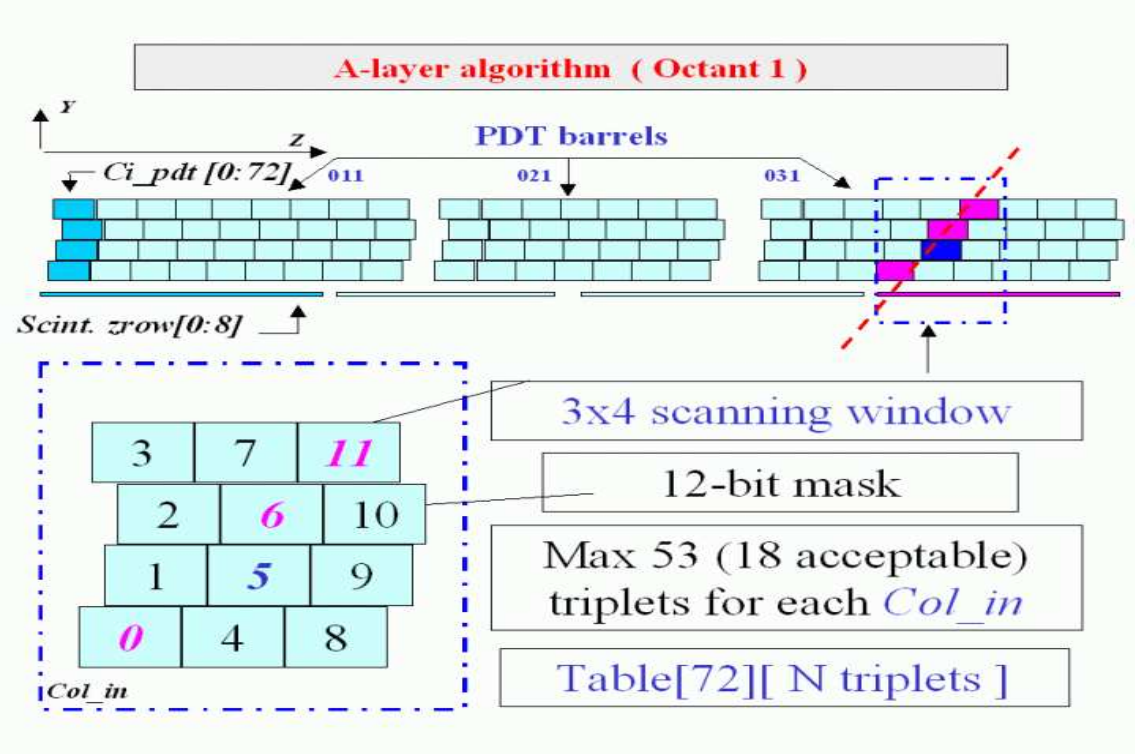

Figure 4.5: Detector structure associated with a central A layer DSP. The 72×4 cell "hyperchamber" is constructed from three neighboring PDTs.

usage of look-up tables. If a valid bitmask is found in a window (the coincidence of minimum three bits is required) then col_i defines the η value of this track candidate. Additionally *coli* is associated with a table of A-layer scintillator counters, which are organized (in each octant) in single decks of 9 ($zrow$=0..8) rows in the z direction times 20 along ϕ. The best match (if any) between col_i and $zrow$ defines an associated scintillator hit and provides ϕ and timing to the segment. Both associations are readily available in the LUTs. After verifying a triplet, the A-layer algorithm performs a residual test using drift distance values of triplet members

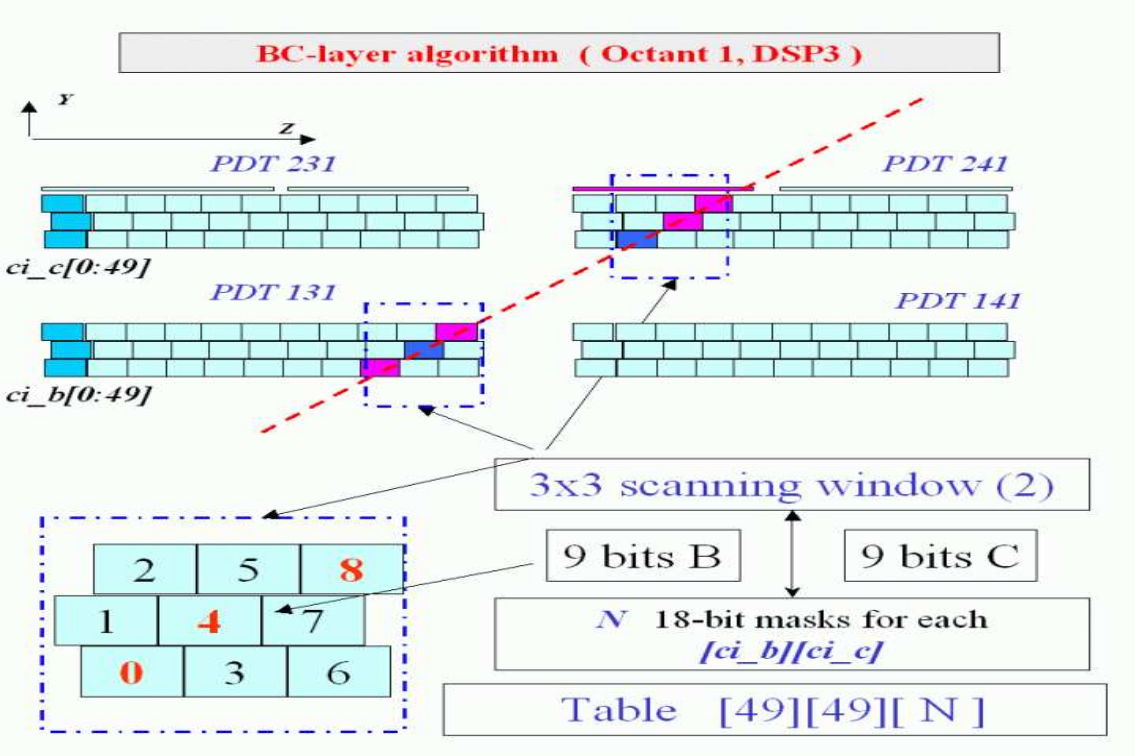

Figure 4.6: Two B and C "hyperchambers" are inputs for the BC-layer DSPs. A reported segment requires matched stubs in each layer.

and precalculated residual equation coefficients.

The BC-layer algorithm differs from the A-layer version mostly due to detector geometry. Every DSP deals with two PDTs in the B layer, two PDTs in the C layer and those scintillator counters that are mounted on them. Two nearby tracks in the B layer may be significantly apart in the C layer, which does not the allow use of inspection windows covering both layers. Thus the search for clusters of hits in the B and C layers is done separately using 3x3 cells inspection windows. Upon hyperchamber inspection N_b and N_c 9-bit masks are formed in each layer (N_b and

N_c correspond to the numbers of nonoverlapped inspection windows with number of hits more then two). Subsequently $N_b \times N_c$ combination masks are formed as unified 18-bit fields (bits 0-8 are reserved for B layer and bits 9-17 for C). Combined masks have an entry column address $[Bcol_{in}][Ccol_{in}]$ and can be quickly tested for validation in the lookup tables. To be accepted the candidate mask should have at least three bits in coincidence with the tabulated one. This method does allow single layer tracks, with three hits only in either the B or C layers. The accepted bitmask is checked for the presence of a C-layer scintillator hit in the z-row corresponding to its $Ccol_{in}$ column index. The LUT-stored detector η and rz-slope, ϕ and time of the associated (if any) scintillator hit and the quality are reported for the successful segment. Table 4.1 summarize tasks performed by the segment finding algorithms.

The described algorithms were coded using the C language. Texas Instruments (the DSP makers) tools were used to make the assembler optimized the the DSP architecture. The resulting executables (hexadecimal files) are downloaded to the DSPs for the online event processing. During the development phase the code was tested in a PCI-resident DSP evaluation board using real collider L2-input data. Timing plots shown in Fig 4.7 measure the algorithm's performance from reading the input data all the way to completing the octant inspection sweep and sending out results. Times are in microseconds and the tester DSP runs at 160 MHz. The 15 μs is well within the $\sim$30 μs time budget.

Table 4.1: Summary for A- and BC-layer muon segment finding.

Actions	
• construction of candidate track segments from the drift hits	
• check candidate validity with look-up tables, extract η or rz_{slope}	
• check for associated scintillator hit, extract ϕ and time(s)	
• associate quality flag that reflects all stub attributes	
• report that stub (η,rz_{slope},quality,times) to the manager DSP	
Segment quality assignment criteria	
(C1) 3 PDT hits with	(C1) 3 PDT hits with
valid LUT bitmask	valid LUT bitmask
(C2) Drift time satisfy	(C2) Hit patterns includes
track residual test	B and C layers
(C3) Associated A-layer scintillator hit	(C3) Associated C-layer scintillator hit
Reported quality bits	
(01b) $\equiv$ (C1)	
(10b) $\equiv$ (C1).and.[(C2).or.(C3)]	
(11b) $\equiv$ (C1).and.(C2).and.(C3)	

4.3.2 Muon track building

The L2 muon tracks are built from the SLIC's segments in two steps. At the first stage a combination of A- and BC- layer segments into tracks is provided on the two processors separately for central and forward segments. Each processor runs code that match A- and BC-segments ordered by segment quality, and favors

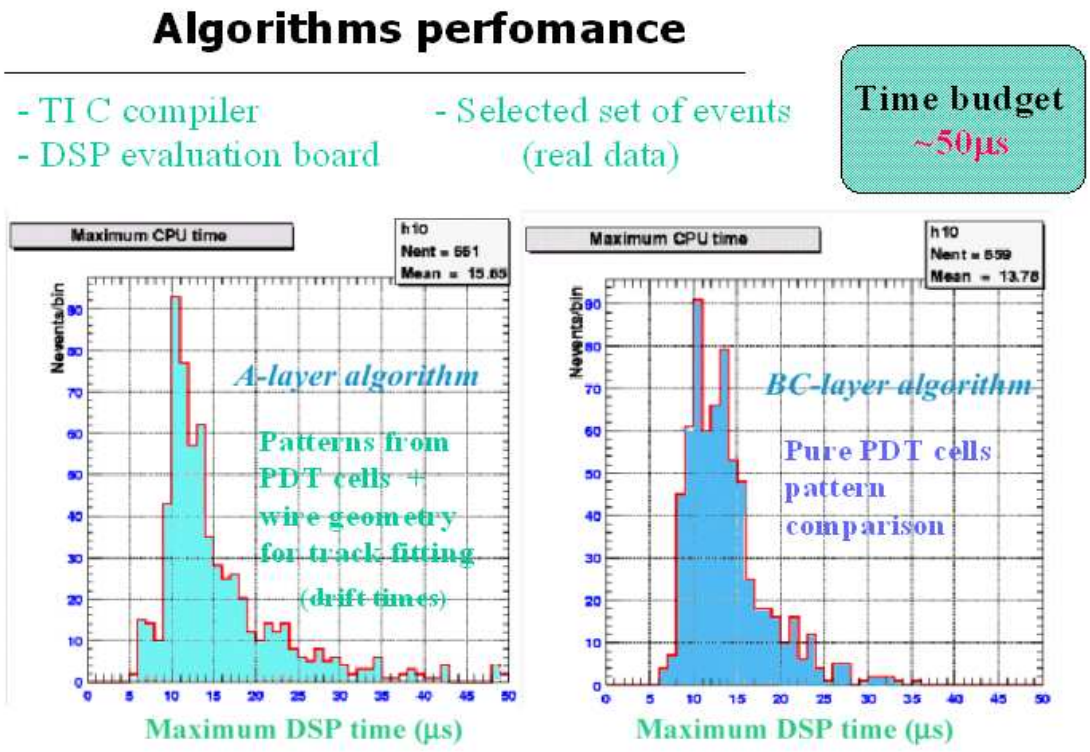

Figure 4.7: Results of A and BC layer code timing tests.

segment combinations with the best track resolution. For successful matches in a ($\Delta\phi$, $\Delta\eta$) = (45°,0.30) window, the processors calculate the momentum of the track from its deflection in the toroid and define a track quality word combining quality bits of the matching stubs. Three quality flags (loose, medium and tight) are defined with different criteria for the central and forward tracks (Table 4.2).

The η and ϕ of the constructed tracks are copies of one of the available segments with the A-layer segment preferred. The scintillator times from the corresponding layers (A,B,C) are also assigned to the track. Assembled tracks are reported to the L2-global board.

Table 4.2: Quality definition for the L2 muon tracks.

Tracks	**loose**	**medium**	**tight**
Central	$Q_A > 0.\text{or.}Q_{BC} > 0$	$Q_A > 0.\text{and.}Q_{BC} > 0$	$Q_A > 1.\text{and.}Q_{BC} > 1$
Forward	$Q_A + Q_{BC} > 1$	$Q_A > 0.\text{and.}Q_{BC} > 0$	$Q_A + Q_{BC} > 3$

At the second stage the L2-global provides an additional loop over central and forward muon candidates matching them in the overlapped ($|\eta| \approx 1$) regions of the muon system and sets the L2 muon trigger bits based on quantity and parameters (quality, detector region, time, p_T)[2] of the detected tracks. Fig 4.8 shows an example of a matched L2 muon candidate with a muon track reconstructed by the offline software.

4.4 The Level-2 muon trigger performance

In the present analysis at least one "medium" L2 candidate was required without any restriction on the L2 muon p_T and time. With these conditions the efficiency of the L2-muon trigger is high (above 96% for offline muons with $p_T > 6$ GeV) and provides minimum losses to the leptoquark signal in a $LQ\bar{L}\bar{Q} \rightarrow b\bar{b}\nu\bar{\nu} \rightarrow$jet($\mu$)jet($\mu$)+$\not\!\!E_T$ signature. The detailed efficiency studies of the muon plus jet triggers used in the analysis are described in Chapter 6.

[2]Due to a limited L2 p_T resolution the efficiency plateau falls to about 80% at a $p_T = 5$ GeV threshold. This restricts the usage of the p_T based triggers.

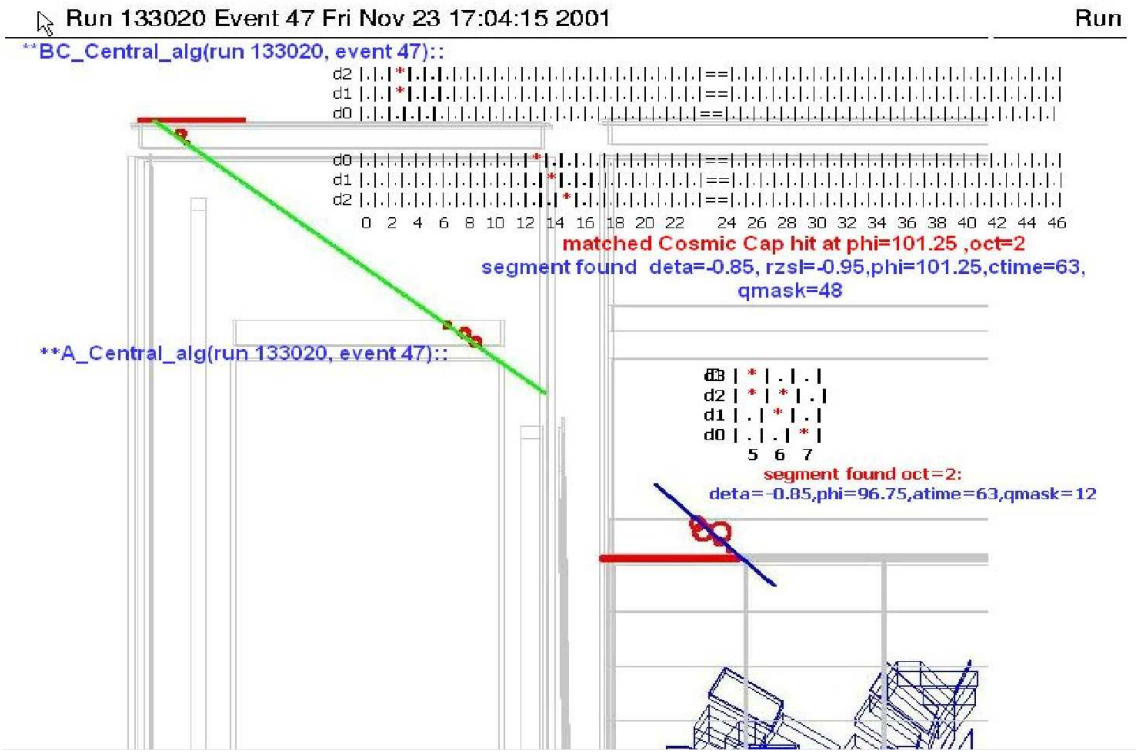

Figure 4.8: A muon track reconstructed by the L2 (red stars) and offline software.

CHAPTER 5
EVENT RECONSTRUCTION

The DØ collision events are described by jets, muons, electromagnetic objects, and missing transverse energy identified by the reconstruction software. Electrons are identified by their longitudinal and transverse shower profiles in the calorimeters and by the fraction of their energy deposited in the electromagnetic sections of the calorimeters. These showers must be isolated from other energy depositions and have an associated track in the central tracking detectors. Jets are reconstructed using a cone algorithm of radius $R = \sqrt{(\Delta\eta)^2 + (\Delta\phi)^2}$, where ϕ is the azimuthal angle and η is the pseudorapidity. Cone sizes of $R = 0.5$ are used in the present analysis. Jet energies are corrected for energy lost in calorimeter cracks, energy from the underlying event, and jet energy outside the cone. Missing transverse energy is determined from the energy deposition in the calorimeters and the transverse momentum of any muons present. Muon tracks are reconstructed using signals from the muon chambers and scintillators. The p_T of a muon is defined using the deflection of the reconstructed tracks in the magnets or by a matched track in the central tracking chambers that originates from the primary interaction vertex.

5.1 The reconstruction software

The event reconstruction chain is illustrated in Fig 5.1. The raw data (real or simulated detector hits and corresponding data taking conditions) are stored on tape. At the first stage of data processing the raw hits are reconstructed as physics objects: vertices, particle and jet candidates, missing energy, etc. At the next stage the reconstructed events that pass certification and correction procedures are preselected to form smaller sets (skims). Selection criteria are sets of triggers and preliminary conditions on the physics objects. The resulting subsets of data (certified physics objects, 10KByte/event) are available for the analyses that could use both the DØ framework tools and specific algorithms and data formats. Up to the last stage, the software development and management is provided by the DØ code control system. The objects and algorithms most important for the leptoquark search will be discussed in the next sections.

5.2 Muons

Muon candidate reconstruction is based on information from the muon detector system and the central tracking system. The muon detector system with its toroid magnet covers more than 90% of the angular acceptance up to a pseudo-rapidity $|\eta| = 2$. It provides unambiguous muon identification with a momentum measurement. A muon identified on the basis of the information provided by the muon detector is called a local muon. The central tracking system provides accurate momentum resolution and is highly efficient at finding tracks in the whole angular acceptance of the muon detector. A local muon that is successfully matched with a

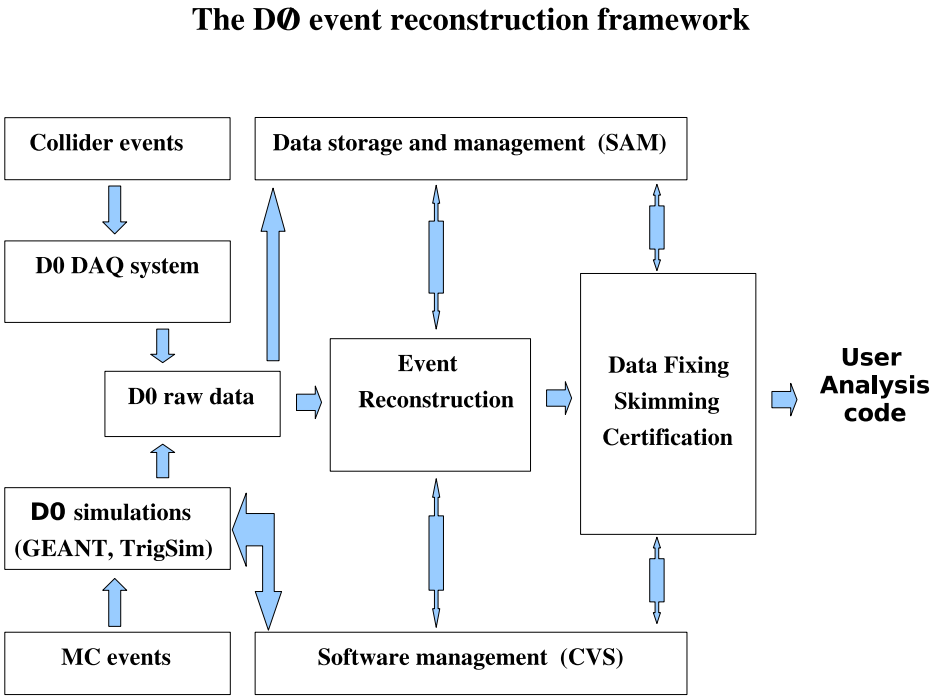

Figure 5.1: The DØ data reconstruction framework.

central track is called a "central track-matched muon". The calorimeters can also serve as an independent source of muon identification using the signature of a minimum ionizing particle (MIP). However the efficiency of MIP identification is lower then other muon signatures.

The reconstructed muon candidates are differentiated by type and quality. Requirements applied to the muon candidates used in the present analysis are summarized in Table 5.1. Reference [48] provides detailed information about muon identification algorithms and candidate definitions.

Table 5.1: Type and quality definitions of muon candidates used in this analysis.

Type		
1	Central track + local muon track (A layer)	
2	Central track + local muon track (BC layer)	
3	Central track + local muon track (A+BC layers)	
Quality		
loose	**medium**	**tight**
$type = 1$ .and.	$type = 1$ .and.	
$NH_{scint} > 0$ .and.	$Region = bottom$[a] .or.	
$NH^{A}_{wire} > 1$	$type = 1$ .and.	
	$P_{BC}(p_\mu)$[b]> 0.7 .and.$p_\mu < 6$ GeV	
$type = 2$ .and.	$type = 2$ .and.	
$NH^{BC}_{scint} > 0$ .and.	$NH^{BC}_{scint} > 0$ .and.	
$NH^{BC}_{wire} > 1$ .and.	$NH^{BC}_{wire} > 1$ .and.	
$Region \neq bottom$	$Region = bottom$	
$type = 3$ medium, but	$type = 3$ .and.	$type = 3$ .and.
one of criteria failed	$NH^{A}_{wire} > 1$ .and.	$NH^{A}_{wire} > 1$ .and.
	$NH^{A}_{scint} > 0$ .and.	$NH^{A}_{scint} > 0$ .and.
	$NH^{BC}_{wire} > 1$ .and.	$NH^{BC}_{wire} > 2$ .and.
	$NH^{BC}_{scint} > 0$	$NH^{BC}_{scint} > 0$ .and.
		a converged local fit

[a] octant 5 and 6 with $|\eta| < 1.6$

[b] P_{BC} denote probability of a low momentum muon to reach the BC layer

This analysis uses *medium* muons which have a central track and hits in the muon system both in the A layer and in either the B or C layer. This requirement is relaxed in the bottom of the detector. These geometrical requirements are essentially the same as the trigger. We associate a muon with a jet if a cone in pseudorapidity- and azimuthal-space, $\Delta R = \sqrt{(\Delta\eta)^2 + (\Delta\phi)^2}$, about the jet is less then 0.5 and contains the muon, where η is pseudorapidity and ϕ is azimuthal angle. We applied a veto on events with isolated *medium* muons with $p_T > 5$ GeV or *loose* muons with $p_T > 10$ GeV.

5.3 Jets

Energy deposition in the calorimeter due to electromagnetic showering, hadronic showering or ionization is observed as signals from the calorimeter sensitive elements (cells). Detector jets are objects made of clusters of neighboring calorimeter cells. The momentum of any given jet is calculated by combining the momenta of cells which belong to the jet.

Fig. 5.2 shows the cell segmentation of the DØ calorimeter in the r-z plane. The geometrical position of a cell center in (η,ϕ) space defines the cell coordinate. Each cell is assigned a 4-momentum vector $p^{cell} = (E^{cell}, p^{cell})$ where E^{cell} is the the measured energy in the cell and p^{cell} is the 3-momentum vector with norm E^{cell}, with direction defined by the primary interaction vertex and the center of the cell. A set of cells which are close (located in an approximately 0.1×0.1 (η,ϕ) region) define a geometrical tower (drawn in the same shading in Fig 5.2). The reconstructed towers are built from the the geometrical one by combining 4-momenta of cells:

$$p^{twr} = (E^{twr}, p^{twr}) = \sum (E^i, p^i)$$

Noisy cells and isolated cells are excluded in the sum above. The transverse momentum p_T^{twr}, the polar θ^{twr} and the azimutal ϕ^{twr} angles, and the pseudorapidity η^{twr} are then calculated using p^{twr}.

The Run II jets are reconstructed in two stages. In the first one a list of preclusters with $p_T > 1$ GeV is built from all towers. Preclusters are formed around seed towers with the $p_T^{seed} > 500$ MeV and require the member towers be at a distance $R < 0.3$ from the seed tower and have $p_T > 1$ MeV. At stage two the list of preclusters are used as input to the Run II cone algorithm [49] that constructs proto-jets. The second proto-jet list is constructed by the midpoint algorithm [50] which searches proto-jets around the preclusters and around the midpoints formed between any combination of two proto-jets obtained in the previous step. For these two proto-jet lists a merging/splitting algorithm is finally applied to remove double counted preclusters and form the resulting final jets.

In the present paper we use jets with energy greater then 8 GeV with radius 0.5. The "good" jets correspond to the criteria: (a) $0.05 <$ EM fraction < 0.95; (b) the coarse hadronic fraction < 0.4; (c) confirmed by the L1 trigger; and (d) no reconstructed EM objects with p_T over 5 GeV in $\Delta R < 0.4$ about the jet's axis. Jets that failed the "good" jet criteria are believed to be a byproduct of calorimeter noise or a misidentified EM object and so defined as "bad". Only "good" jets were used for the calculation of kinematic variables and analyses cuts.

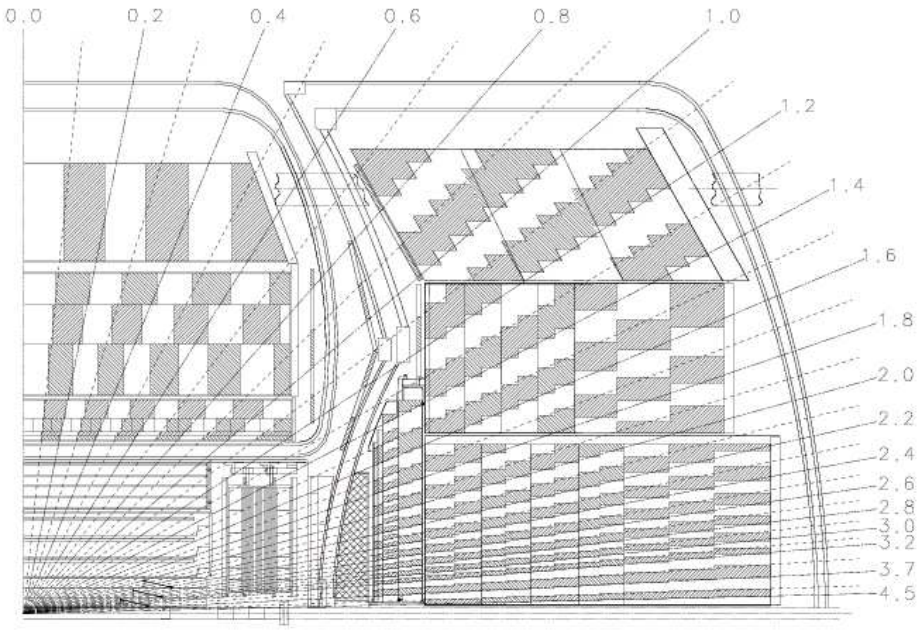

Figure 5.2: View of the calorimeter in the $r - z$ plane.

5.3.1 Electromagnetic objects

The electron and photon (EM) candidates are formed by calorimeter clusters with a minimum transverse energy greater then 1.5 GeV. The cluster EM fraction is required to be greater then 90%. An isolation EM fraction is required to be less then 0.2, where the isolation variable is defined as $\frac{E^{tot}_{0.4}-E^{em}_{0.2}}{E^{em}_{0.2}}$ ($E^{tot}_{0.4}$ is the total energy in a cone of radius 0.4 and $E^{em}_{0.2}$ is the EM energy in a cone of radius 0.2). Additional selection criteria are based on the shower shape analysis (8×8 matrix as a measure of how similar the shower is to an electron shower) and the presence of a matching track over a certain momentum threshhold (for electrons). The p_T of the electron is calculated using the position and energy of the EM cluster and the primary vertex

(or a vertex (0,0,0) if there is no vertex).

We used DØ certified (as described in references [51] and [52]) EM objects were used without any additional requirements. We vetoed events with an isolated EM object with p_T over 5 GeV.

5.3.2 Missing energy

The presence of neutrinos and other non-interacting particles is inferred by measuring the event missing transverse energy ($\not\!\!E_T$). $\not\!\!E_T$ is determined by the vector sum of the transverse components of the energy deposited in the calorimeter and the p_T of detected muons. Muon momentum was smeared in Monte Carlo events to compensate for the difference between data. The corrections applied to the reconstructed jets, electromagnetic objects, and from the jet energy scale and the electromagnetic scale are also propagated in the missing energy calculations [53]. For the event selection we also used $\not\!\!H_T \equiv |\sum_{jets} \vec{p_t}|$, the vector sum of jet transverse momenta.

5.3.3 Jet b-tagging using the impact parameter

The Jet LIfetime Probability (JLIP) b-tagging algorithm [54] uses the fact that tracks originating from secondary vertices have larger impact parameters than tracks from the primary vertex. Impact parameter is defined as the minimal distance from the primary vertex to a track in the plane transverse to the beam. It has the sign of the scalar product of the vector corresponding to it (starting from the primary vertex) with the track $\vec{p}_T$.

The algorithm requires at least two tracks in a jet each with a hit in the silicon tracker. The impact parameters of the jet-associated tracks are combined into a single variable, the "jet lifetime probability", that determines the probability that all tracks in a jet originate from the primary interaction point. The distribution of this variable for jets from $c-$ and $b-$quark decays has a peak at very low value while it is uniform for jets from the fragmentation of light quarks. This makes it possible to select b-jets by applying a cut on this probability.

The present analysis uses six certified working points of the JLIP b-tagger which correspond to threshholds on the probability of a jet to be of light flavor. These probability threshholds are 0.1%, 0.3%, 0.5%, 1.0%, 2.0%, 4.0% and define b-tags which are further denoted as $P^{lf}_{0.1}$, $P^{lf}_{0.3}$, $P^{lf}_{0.5}$, $P^{lf}_{1.0}$, $P^{lf}_{2.0}$, and $P^{lf}_{4.0}$. A mean mistag rate for these working points for light quark jets with $E_T < 95$ GeV is approximately equal to the tag threshhold value. Direct tagging using JLIP was performed only on data. For Monte-Carlo samples the b-tag probabilities were obtained using the Tag Rate Function (TRF). The TRF gives b-tag probabilities which depend on the E_T, η and jet flavor. The flavor of a MC jet can be found by matching the Monte-Carlo hadrons with a jet cone. An MC jet is considered to be a b-jet if its cone contains at least one b-hadron. If the jet cone does not match with a b-hadron but matches with a c-hadron, the jet will be considered as a c-jet. If the jet cone does not match to a b or c hadron, it is considered as a light quark jet.

The TRF should be multiplied by a factor called taggability, defined as the probability of a jet to be taggable. It equals the ratio of the numbers of taggable jets to the total number of jets in given E_T and η bins. A jet is considered as taggable

if it has at least two good quality tracks. We also include in the determination of the taggability the z-position of the primary vertex of the event. Taggability is analysis dependent and should be calculated for the data sample used for conditions which are close to that actually used for b-tagging. To parameterize the taggability jets with $E_T > 15$ GeV and $|\eta| < 2.5$ were selected from events which passed the following cuts:

- $\Delta\phi(\not\!\!E_T$, jet $E_T > 15$ GeV$) > 0.5$
- $\not\!\!E_T > 60$ GeV, $\not\!\!H_T > 40$ GeV, $E_T^{jet1} > 40$ GeV, $E_T^{jet2} > 20$ GeV
- veto on events with isolated muons or EM objects.

Fig. 5.3a presents the E_T dependence of the jet taggability for data. The solid line shows a fit to the data and the dashed lines show the uncertainty band after varying the fit by $\pm 1\sigma$. Figures 5.3b and 5.3c show the corresponding dependence on η and z-position of the primary vertex. In Fig. 5.3d the E_T distribution of taggable jets (points with error bars) is compared with prediction based on the taggability fits for all three variables :

$$F(p_T, \eta, PVz) = (eff_{mean})^{-2} \times eff(E_T) \times eff(\eta) \times eff(PVz)$$

Corresponding closure plots for the η of jets and for the z position of the primary vertex are presented in Figures 5.3e and 5.3f. All closure plots show good agreement between real and parameterized distributions.

5.4 Simulations

DØ software provides the framework [55] for the full reconstruction of Monte-Carlo events. The simulation chain include three basic stages:

• Generation of events. In the present analysis PYTHIA [56], ALPGEN [57] and CompHEP [58] generators were used for the simulation of leptoquark pair production and the Standard Model backgrounds (Section 6.2.2). The leptoquark signal samples were generated with PYTHIA. For all other samples PYTHIA was used only to perform showering and hadronization while at the parton level MC events were generated with ALPGEN and CompHEP. The parton density functions used were CTEQ5L [59].

• Simulation of the DØ detector response. Energy deposition in the active areas of

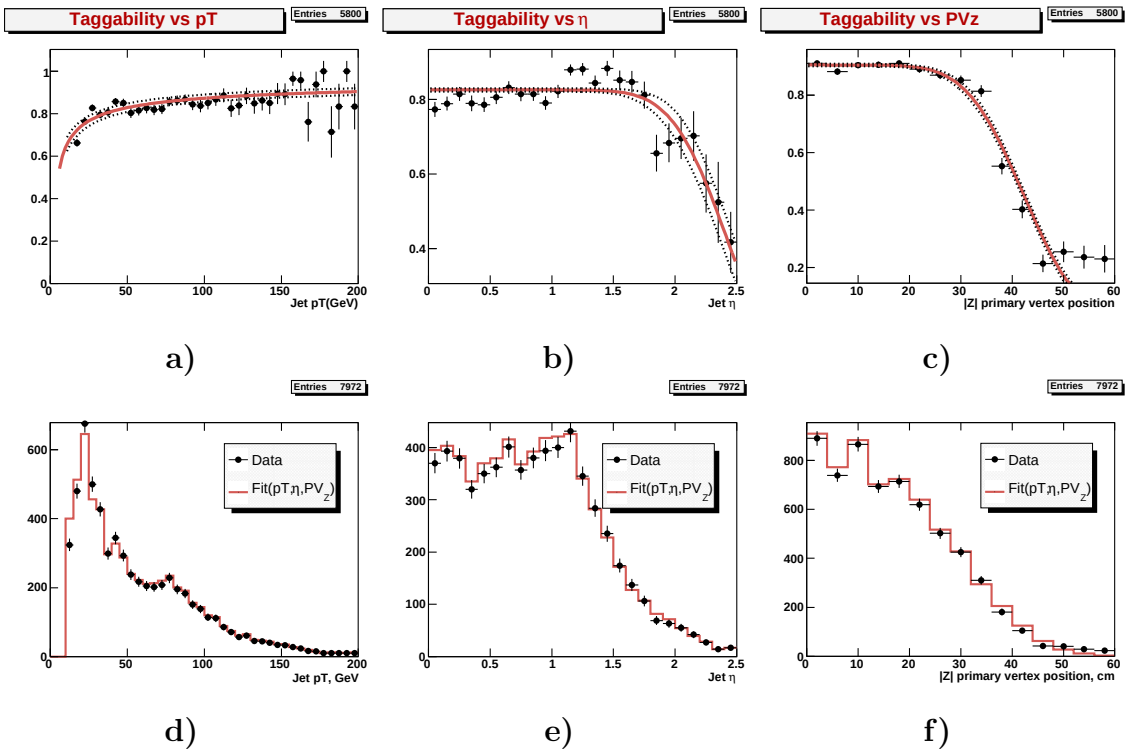

Figure 5.3: Taggability as function of jet E_T (a) , η (b), PV_Z (c), and the corresponding closure plots (d, e, f).

the detector is obtained using GEANT [60]. The D0Sim package was used for the electronic simulation of the detector and pile-up of any additional minimum-bias interactions that occur in the same crossing as the signal event. An average of 0.8 minimum bias events were superimposed for all MC samples.

• Reconstruction of the simulated detector response. This software is identical to that used reconstruction of real collider data.

An additional package, TrigSim [61], is available for trigger efficiency studies and to test and debug online trigger software before it goes online. TrigSim simulates the L1 trigger hardware and runs the same code for the L2 and L3 systems as the DØ data acquisition system. The output of TrigSim contains trigger objects as well as trigger bit masks. In the present analysis, TrigSim was used to cross check the efficiency parameterization extracted from real data samples (Chapter 6).

CHAPTER 6
SEARCH FOR THE THIRD GENERATION LEPTOQUARKS USING MU+JET EVENTS

This Chapter describes a search for charge 1/3 third generation leptoquarks (LQ) produced in $p\bar{p}$ collisions at $\sqrt{s} = 1.96$ TeV using the DØ detector at Fermilab. Third generation leptoquarks are assumed to be produced in pairs and to decay to a tau neutrino and a b quark with branching fraction B. Data collected with muon plus jet triggers were analyzed using muon and impact parameter b-tagging.

6.1 Data samples

The analysis is based on data collected by the DØ detector between May 2002 and November 2004. The MU_JT20(25)_L2M0 and MUJ2_JT25(_LM3) triggers were used to select events. The main trigger requirements were the presence of a muon candidate with hits in muon scintillators and wire chambers and a jet with $E_T > 20$ GeV ($E_T > 25$ GeV starting May 2004). All data events were reconstructed using the certified DØ framework. The resulting data sample corresponds to an effective luminosity of 367 pb^{-1}. This was used for the normalization of the Standard Model background samples. The contributions from the particular triggers are shown in Table 6.1. The triggers detailes are described in Appendix A.

6.2 Data cleaning

In events without a primary vertex or in those that contain mismeasured jets, the $\not\!\!E_T$ can not be reconstructed accurately. We applied "track confirmation" criteria to the good jets and rejected events containing bad jets with $E_T > 15$ GeV and events without a reconstructed primary vertex.

A jet is considered confirmed if the scalar sum of the p_T of tracks associated with it exceeds 5% of the jet E_T. For an effective usage of jet track confirmation, the primary vertex is required to be ± 60 cm from the center of the detector. The tracks used should have at least eight CFT hits. The distance of closest approach to the primary vertex should not exceed 2 cm in r and 5 cm in z. This criteria algorithm, proposed in [62], was used to confirm any good jet with $E_T > 15$ GeV and $|\eta_{det}| < 1.5$. Such detector η range corresponds to the fiducial region of the central detector.

We studied the inefficiency introduced by cleaning on a signal with natural $\not\!\!E_T$ using $W \rightarrow \mu\nu + jets$ (Appendix B). This process was chosen because its features are similar to the leptoquark signal. It is also one of the most important backgrounds and can be selected relatively easily with the desired purity. Fig. 6.1 presents the W transverse mass and Fig. 6.2 shows the $\not\!\!E_T$ distribution for the sample. The

Table 6.1: Effective luminosities associated with different triggers.

Trigger	mu_jt20_l2m0	mu_jt25_l2m0	muj2_jt25(_lm3)
L_{int}	114 pb^{-1}	210 pb^{-1}	42 pb^{-1}

red histogram represents our set of SM processes while the blue histogram shows the contribution of the $W \rightarrow \mu\nu + 2\ jets$ separately. Other processes contribute about 10% in total. To account for the difference in track-matching and isolation efficiency between the data and MC the factor 0.915 [63] was applied to MC events. To find the inefficiencies of the bad jet removal and the jet track confirmation we

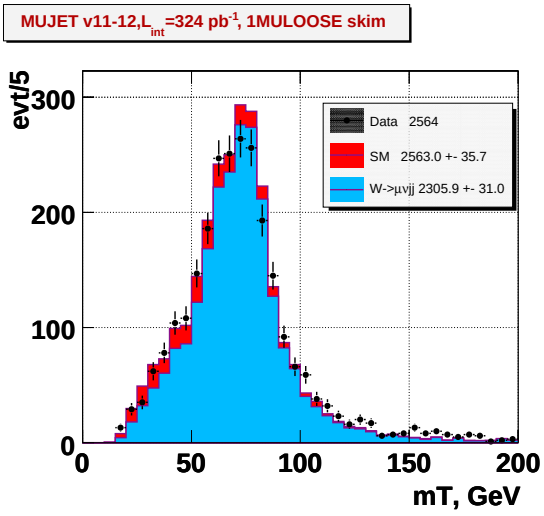

Figure 6.1: The transverse mass distribution for the W mujet triggered sample.

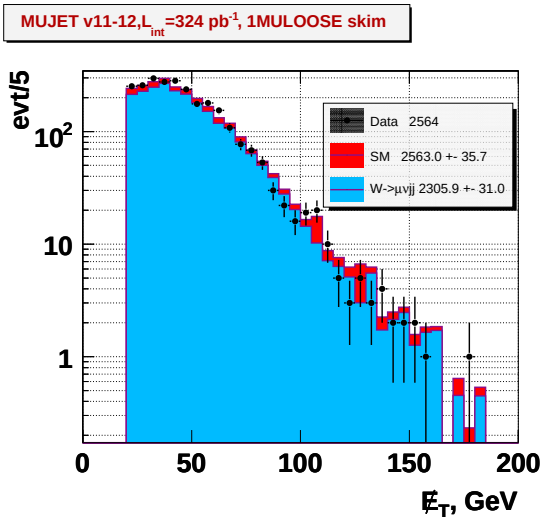

Figure 6.2: $\not\!\!E_T$ for the W mujet triggered sample.

selected the central part of the m_T distributions. The results are summarized in Table 6.2. The scale factors shown were applied to all Monte Carlo samples if the corresponding cuts were used.

Table 6.2: The efficiencies of cleaning cuts for data and Monte-Carlo. Events are selected in the m_T window of 50-90 GeV.

Cut	Data	MC	Data/MC ratio
track. conf., first leading jet	0.963±0.005	0.995±0.001	0.967±0.005
track. conf., first two leading jets	0.951±0.007	0.990±0.002	0.960±0.007
bad jet removal	0.968±0.005	0.986±0.002	0.982±0.005

6.3 Trigger efficiency parameterization

For muon plus jet triggers the TopTrigger package [64] was used for events with muons and jets of energy above 15 GeV. For data with objects of lower energies, efficiencies were extracted using real data samples of unbiased muon events which passed a missing energy based triggers. For the MU_JT20_L2M0 trigger the corresponding turn-on curves as a function of leading muon p_T are shown in the left plots of Fig. 6.3. The efficiency extracted from the TopTrigger parameterization for signal events of $M_{LQ} = 150$ GeV is also shown on these plots for comparison (blue points with error bars). The parameterizations of these curves used in the analysis are shown on the right plot in the same figures. The dotted lines are the uncertainties of the fit functions due to variation of parameters. In Appendix C similar plots illustrate the efficiency parametrization of the MU_JT25_L2M0 and MUJ2_JT25(_LM3) triggers. For events containing more then one muon the total muon trigger efficiency

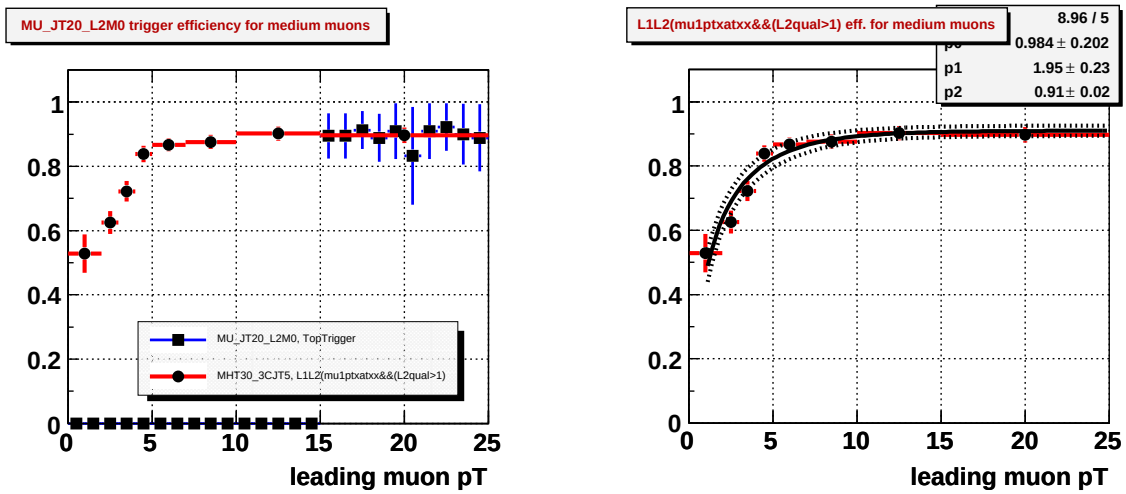

Figure 6.3: MU_JT20_L2M0 trigger. Efficiency (left plot, red graph) as a function of the leading muon p_T measured with a missing H_T trigger and its parameterization (right plot, black graph) with the errors bounds (dotted lines). The efficiency as calculated with the TopTrigger package for the signal sample M=150 GeV (left plot, blue graph) is shown for comparison.

of the event was calculated as $P(N_{muons}) = 1 - (1 - P(i)) \times .. \times (1 - P(N)), (i = 1, .., N_{muons})$. The resulting efficiencies for the signal sample of $M_{LQ3} = 150$ GeV vs $\not\!\!E_T$ and the leading jet E_T^{jet0} are illustrated in Fig. 6.4. For events with at least one medium muon, $\not\!\!E_T > 40$ GeV and $E_T^{jet0} > 40$ GeV the efficiency is about 90%.

6.4 Signal features

The signature of the $LQ\bar{L}\bar{Q} \rightarrow b\bar{b}\nu\bar{\nu}$ decay is two energetic b-jets accompanied by significant $\not\!\!E_T$. Figures 6.4(a-c) show distributions of jet multiplicity, E_T of leading jets and the $\not\!\!E_T$ for a simulated decay of a leptoquark pair with $M_{LQ} =$ 150 GeV. For the missing energy and for the leading jet E_T, the maximum regions of

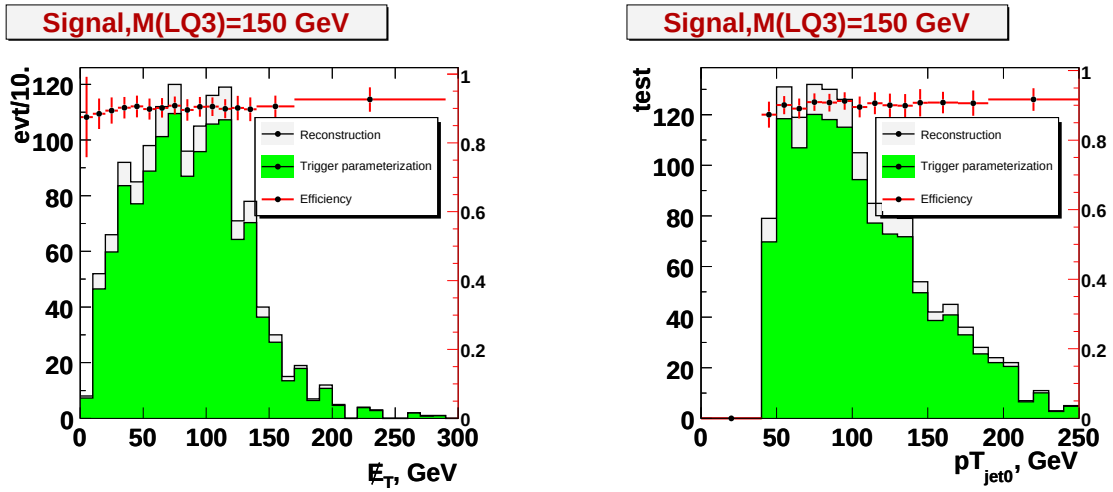

Figure 6.4: MUJET triggers efficiencies vs $\not\!\!E_T$ and the leading jet E_T for the $M_{LQ3} =$ 150 GeV signal sample.

the corresponding distributions start around 50 GeV which allows high cuts for these parameters. The second leading jet energy distribution has a maximum at 30 GeV and the corresponding cut was chosen at 20 GeV for the initial signal selection. The minimum $\Delta\phi$ angle between $\not\!\!E_T$ and the nearest jet has a flat distribution until ~ 0.7 rad with the majority of the signal events above this value. Fig. 6.4f shows the p_T of reconstructed muons coming from the decay of b or c quarks. The spectra falls fast above p_T of 5 GeV. About 5% of the events with muons have more than one muon arising from semileptonic decays. Fig. 6.4g gives the p_T distribution of two leading reconstructed muons in these events.

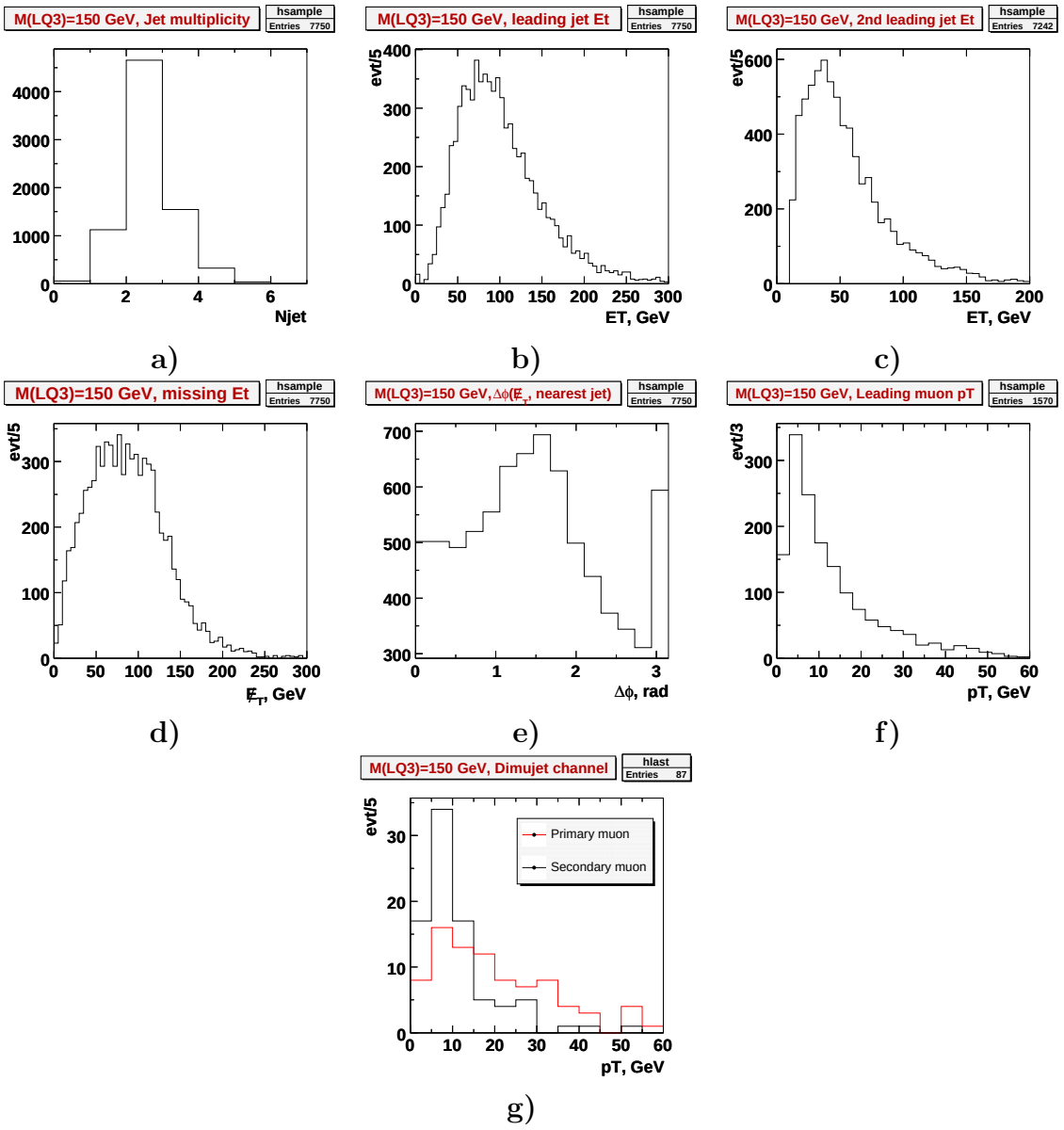

Figure 6.5: Leptoquark (M_{LQ3} = 150 GeV) signal properties: a) jet multiplicity distribution, b) first leading jet E_T, c) second leading jet E_T, d) $\not\!\!E_T$ distribution, e) the minimum $\Delta\phi$ angle between $\not\!\!E_T$ and the nearest jet, f) p_T of the leading muon from semileptonic decay, g) p_T of muons in the dimuon channel

6.5 Backgrounds

The instrumental background to the leptoquark signal comes mostly from QCD processes with fake $\not\!\!E_T$ due to jet mismeasurement or calorimeter noise. The background dominates the low $\not\!\!E_T$ region. Physical backgrounds (which we defined as "SM processes") include processes with real $\not\!\!E_T$. The most important of these are leptonic decays of W/Z bosons + jets events and processes with a top quark. $W \rightarrow \mu\nu + jets$ events mimic the signal if a muon from W decay accidentally overlaps a jet. The $W \rightarrow \mu\nu$ or $e\nu$ samples with $b\bar{b}$ pairs and a muon or electron in the final state look similar to the signal if the lepton remains unreconstructed. $Z \rightarrow \nu\nu + b\bar{b}$ is the same topology as LQ.

To estimate the contribution of SM backgrounds we used the official DØ Monte Carlo samples for the processes shown in Table 6.3. For all samples except $t\bar{t}$ and single top, the NLO cross section were obtained from [65]. Cross sections for $t\bar{t}$ production were taken from [66] and single top production from [67].

Only the samples W/Z + two jets in the final state were used according to the jet topology of this analysis. This approach was chosen due to technical difficulties in combining currently available Alpgen+Pythia samples generated for different jet multiplicities. The combining procedure [68] requires a matching of partons with particle jets to avoid double counting of configurations. The existing code [69] performs this in a very inefficient way, e.g. only about 5% of events survived selection for some samples. As a result the statistical uncertainty becomes unacceptably large. However we assume that good description of clean signal $W \rightarrow \mu\nu + jets$ shown in Fig 6.1 and Fig 6.2 implies that similar Monte Carlo samples for other leptons and

Z boson also can be considered good. The systematic uncertainty of 15% due to SM cross sections used is considered in the determination of the leptoquark mass limit.

Table 6.3: MC samples used for SM background description

Process	σ(NLO), pb	Events generated
W($\mu\nu$) + jj	288	186929
W($e\nu$) + jj	288	188967
W($\tau\nu$)+ jj	288	27996
Z($\nu\nu$) + jj	174	80986
W($\mu\nu$) + $b\bar{b}$	4.2	98951
W($e\nu$) + $b\bar{b}$	4.2	97950
W($\tau\nu$) + $b\bar{b}$	4.2	27249
Z($\nu\nu$) + $b\bar{b}$	1.2	29239
$t\bar{t} \rightarrow b\bar{b}l\nu l\nu$	0.69	9000
$t\bar{t} \rightarrow b\bar{b}l\nu jj$	2.9	44248
$t\bar{t} \rightarrow b\bar{b}jjjj$	3.1	57250
Single top, $\mu\nu bq\bar{b}$	0.26	15500
Single top, $\mu\nu b\bar{b}$	0.12	30500

6.6 The muon tagging analysis

The analysis was done in two steps. At the first step only muon tagging of b-jets was applied. At the second step the JLIP tagging was additionally required to improve the signal to background ratio. This section describe the analysis based on the selection of events in which as least one jet is associated with a muon.

Preselection

After removing bad runs and bad luminosity blocks, events with problems such as missing crates, coherent noise, or without a reconstructed vertex were also rejected. Next, a set of preliminary "precuts" was used to define the initial data sample for muon plus jet events:

- at least two jets, with $E_T^{jet2} > 15$ GeV
- at least one jet associated with a medium track confirmed muon ($\Delta R(\mu, jet) < 0.5$)
- $\not\!\!E_T > 35$ GeV
- $\Delta\phi(\not\!\!E_T, nearestjet) > 0.5$

Applying the same cuts to the $M_{LQ3} = 150$ GeV signal sample gave an acceptance of about 12% (including the muon plus jet trigger parameterization, section 4.1) which includes the 2.6% contributed by the channel with two muon associated jets. The event flow for each muon trigger is shown in Table 6.4.

For the selected data sample a comparison with standard model samples shows 25 times more data than expected due mostly to QCD multijets. Futher data cleaning is a necessity. Fig. 6.6 demonstrates the change of the $\not\!\!E_T$ distribution for events in the the selected data sample after removing bad jets with $E_T > 15$ GeV and requiring track confirmation for any good jet with $E_T > 15$ GeV and $|\eta_{det}| < 1.5$. The blue histogram shows preselected events; the yellow shows the effect of removing bad jets, and the red histogram is the cleaned sample after subsequent jet track confirmation. The effect of the track confirmation is small and this cut was excluded from the analysis. It was subsequently found that no events with unconfirmed jets survived the full set of cuts. The contribution of the events containing energetic bad jets is significant. As shown on Fig. 6.7a, these bad jets are mostly located around the calorimeter crack regions and so have a high probability of being reconstructed with the incorrect energy and thereby degrade the measurement of events $\not\!\!E_T$. Thus

Table 6.4: Initial data sample selection.

Triggers	mu_jt20_l2m0	mu_jt25_l2m0	muj2_jt25(_lm3)	
$L_{recorded}, pb^{-1}$	140.5	230.4	51.5	422.4
Triggered events	7297605	9877983	2104674	19280262
Data quality cut	6141060	8987791	1754707	16883558
$L_{effective}, pb^{-1}$	114.5	209.7	42.7	366.9
Cal problems, No vertex	5849399	8464925	1669555	15983879
Precuts	17512	32639	6390	56541

events with bad jets were removed.

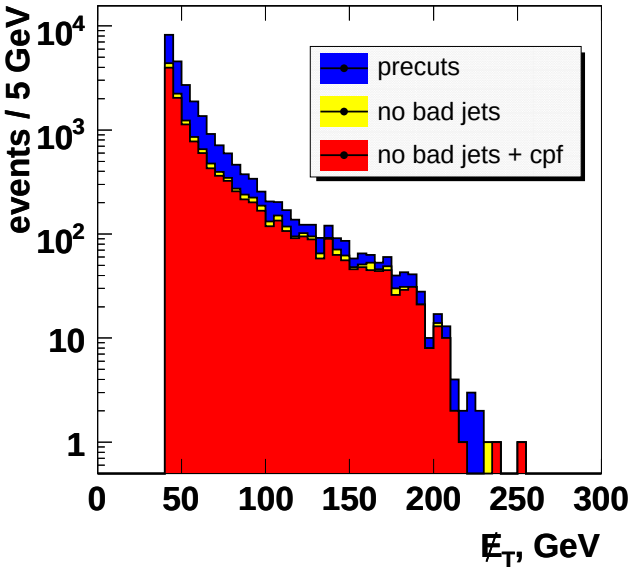

Figure 6.6: The effect of bad jets removal and jet track confirmation on $\not\!\!E_T$. The blue histogram shows preselected events; the yellow shows the effect of removing bad jets, and the red histogram is the cleaned sample after the track confirmation.

To exclude regions of trigger inefficiency the cut on leading jet E_T^{jet1} was set at 40 GeV, the E_T^{jet2} of the second jet was required to be greater then 20 GeV, and the leading muon was required to have $p_T^{\mu} > 4$ GeV. Finally after a combination of cuts on $\not\!\!H_T$ (Fig. 6.7b), $\not\!\!E_T$ (Fig. 6.8a), and $\Delta\phi(\not\!\!E_T, nearestjet)$ (Fig. 6.8b), good agreement between data and SM predictions was obtained. Table 6.5 illustrates the cutflow where (CN, N=0,1,2,3,4) corresponds to criteria:

- at least one muon with $p_T > 4$ GeV with BC layer hits (c0)

- removal of bad jets events (c1)

- $E_T^{jet1} > 40$ GeV, $E_T^{jet2} > 20$ GeV (c2)

- $\Delta\phi(\not\!\!E_T, nearestjet) > 0.7$ (c3)

- $\not\!\!E_T > 75$ GeV, $\not\!\!H_T > 50$ GeV (c4)

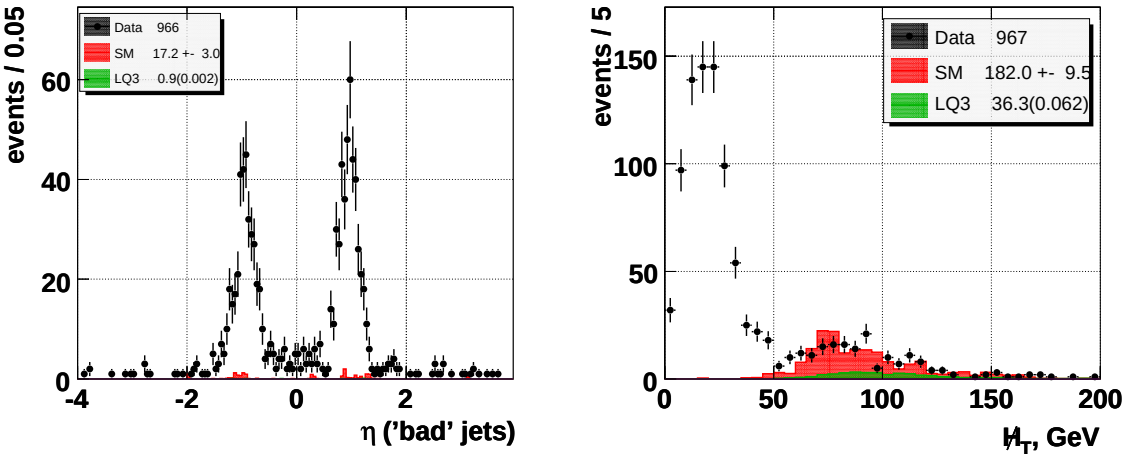

a) b)

Figure 6.7: *a*) The η distribution of the unconfirmed jets: excess of data (dots) due to instrumental background in the calorimeter crack regions, *b*) The $\not\!\!H_T$ distribution: the SM (red histogram) does not describe data (dots) below 50 GeV.

The correction scale factor $\epsilon_{corr} = \epsilon_{DataCleaning} \times \epsilon_{TrackMatch}$= 0.919 was applied to MC events : $\epsilon_{DataCleaning} = 0.982 \pm 0.005$ is the scale factor for bad jet removing and $\epsilon_{TrackMatch} = 0.936 \pm 0.005$ is the track matching efficiency for medium muons [63]. The DATA/MC comparisons for the $\not\!\!E_T$, p_T of the first and second jets, and the leading muon p_T^{μ} after the cuts c0-c4 cuts are shown in Fig 6.9.

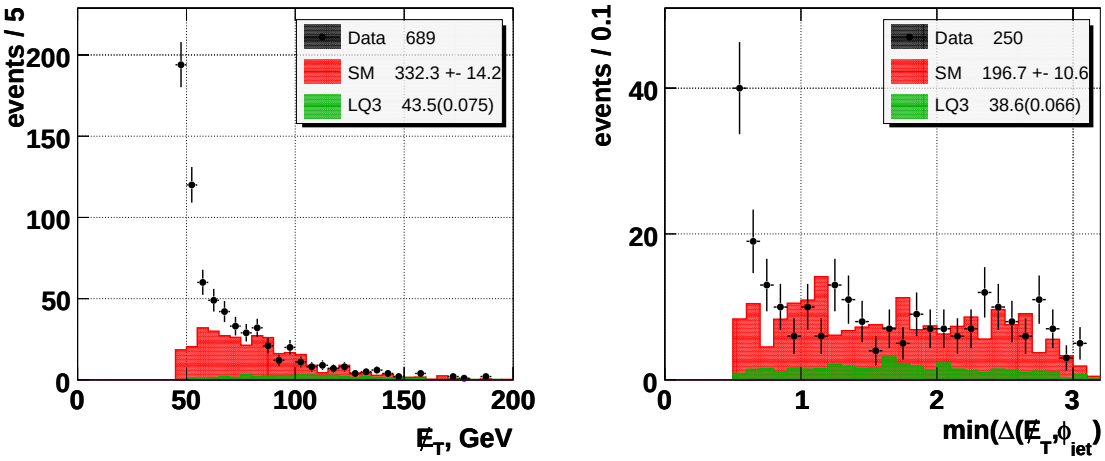

a) b)

Figure 6.8: Excess of data (dots) due to instrumental background for $\not\!\!E_T < 65$ GeV and $\Delta\phi(\not\!\!E_T, nearestjet) < 0.7$ rad regions: *a*) the $\not\!\!E_T$ distribution after the $\Delta\phi(\not\!\!E_T, nearestjet) > 0.7$ rad cut. *b*) The $\min(\Delta\phi(\not\!\!E_T, jet)$ distribution after $\not\!\!E_T > 65$ GeV. SM background is shown in red histograms and the leptoquark signal for M_{LQ}=150 GeV is shown in green histograms.

Table 6.5: Preliminary cuts. Acceptance values for $M_{LQ3} = 150$ GeV.

Cut	Precuts	c0	c1	c2	c3	c4
Data, # events	56541	49008	28224	17090	7775	191
SM, # events	2349	1432	1249	625	548	178
Signal acceptance, %	12.1	10.9	10.7	9.7	8.8	6.2

These selection criteria used in Fig. 6.9 were defined as "noQCD" since only a small insignificant excess of data events in the lower $\not\!\!E_T$ bins can be seen. After these cuts less then 30 events are from QCD multijet sources while the remainder are

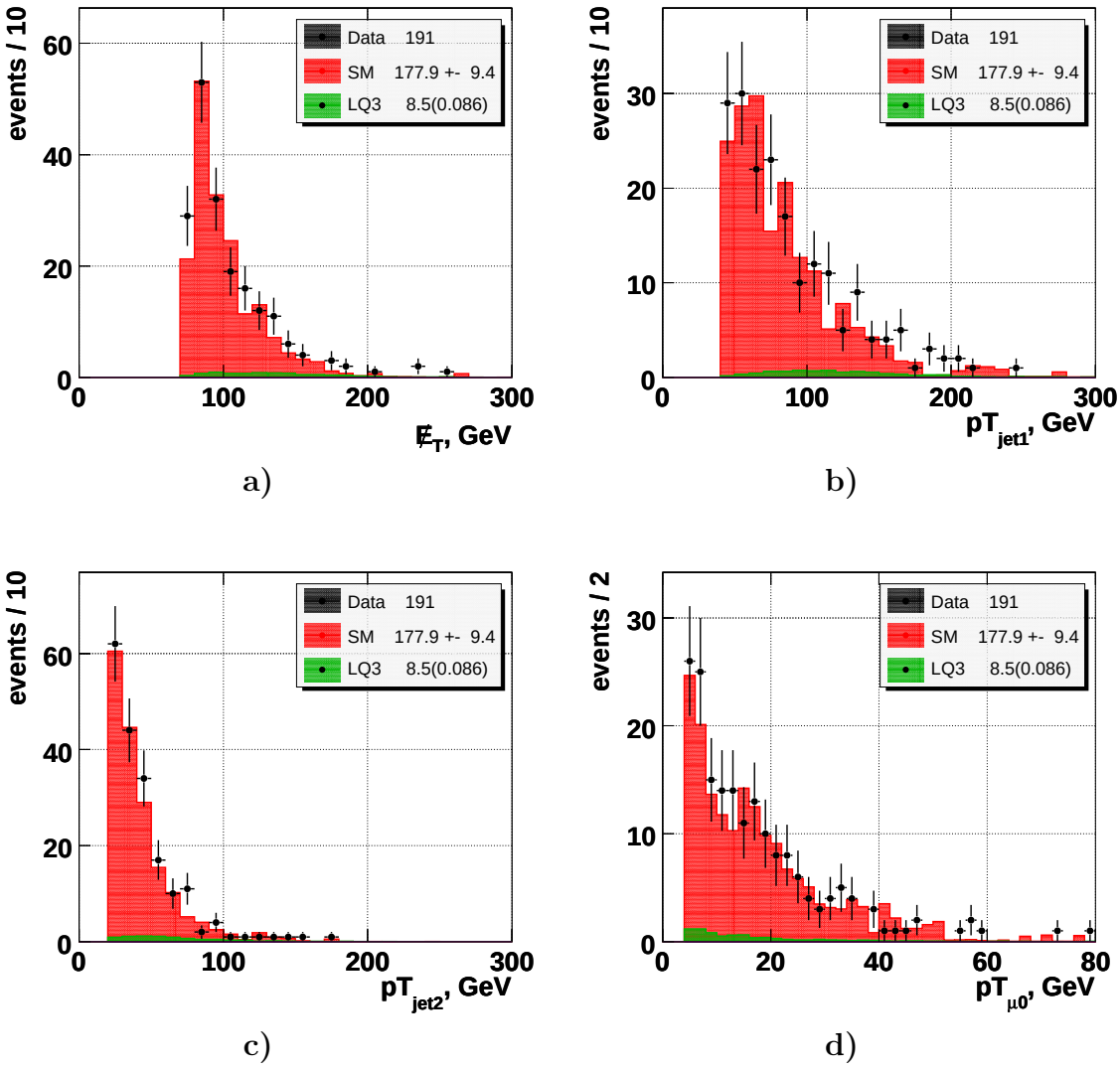

Figure 6.9: Comparison data (dots) and SM MC (red histograms) in the "noQCD" point: *a*) the $\not\!\!E_T$ distribution, *b*) leading jet p_T, *c*) second leading jet p_T, *d*) leading muon p_T. For the leptoquark signal (M_{LQ}=150 GeV) these distributions are shown in green histograms.

from SM processes (W, Z, and *top*). A veto on isolated leptons (for $p_T^{e/\mu} > 5$ GeV) removes events which do not fit the signal signature.

In the surviving events one jet was already tagged with an associated muon which makes it the most promising b-jet candidate. The two b-jets in the LQ3 signal carry a dominant fraction of the event's transverse energy. So the most energetic non-muon, or "recoil" jet, becomes the next most probable b-jet candidate. The fraction of E_T carried by these two jets and the muon was define

$$X_{jj} \equiv (E_T^{jet1} + E_T^{jet2} + p_T^{\mu})/(\sum_{alljets} E_T + p_T^{\mu})$$

The X_{jj} distribution for the events which passed the "noQCD" cuts and the e/μ isolation veto is shown in Fig. 6.10a. Requiring $X_{jj} > 0.8$ reduces $t\bar{t}$ and single top background by a factor of 4. It was also required that both b-jets candidate be in the $|\eta| < 1.5$ region and $E_T > 50$ GeV for the recoil jet (Fig. 6.10b).

Muon b-tagging

The main sources of background for muon-tagged events are

- muons from W/Z decays
- muons from K/π decays
- muons produced in a calorimeter shower
- fake muons

The last two are very small due to the thickness of the calorimeter and the magnets. Because muons originating from K/π decays in general have a softer p_T spectrum than muons from semileptonic decays of heavy quarks [71], the appropriate selection of the p_T cut can suppress their contribution. The momentum of the leading muon

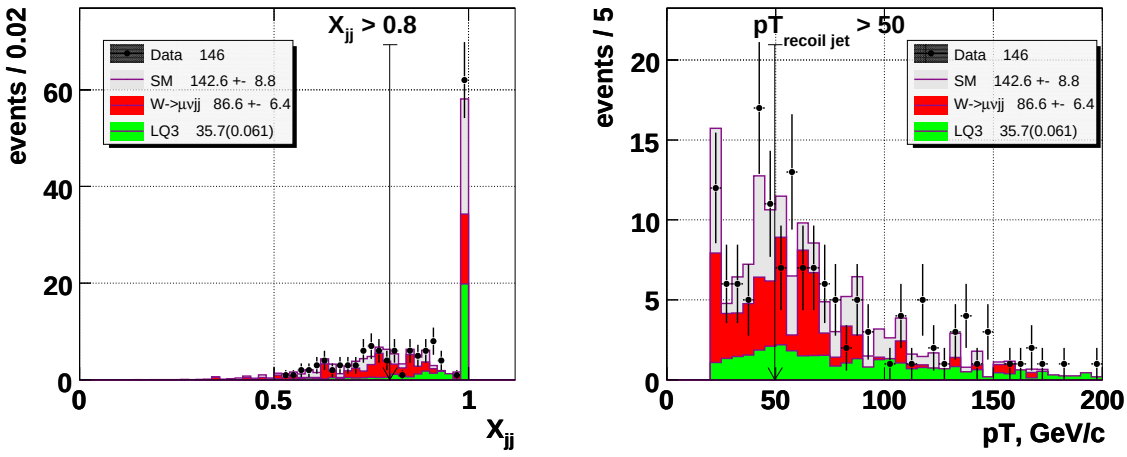

a) b)

Figure 6.10: a) Distributions of the X_{jj} variable, b) the E_T of the recoil jet. SM background is shown in grey histograms and the leptoquark signal for M_{LQ}=150 GeV is shown in green histograms. Also shown the contribution of the $W \rightarrow \mu\nu + jets$ background (red histograms)

p_T^{μ} was required to be greater than 6 GeV.

Most of the W events which mimic b-decays are those in which the muon from the direct decay of the W falls into a $\Delta R < 0.5$ cone of a jet. Additional isolation cuts can reduce this source. If the muon comes from a jet it points in most cases to the tracker region with some tracks and to the calorimeter region with a high energy deposition from that jet. The direction of a muon from W decay which is accidentally associated with a jet does not have strong correlations. The discrimination parameters are the transverse calorimeter energy and Σp_T of tracks in the cone around the muon direction. We define:

$\Sigma p_T^{track} \equiv \sum_{tracks, dR(track,\mu)<0.5} |\vec{p_t}|$, scalar sum of track p_T in a cone of 0.5 around

the muon. Only tracks which passed the criteria for track confirmation were counted. A cut at 10 GeV (Fig. 6.11a) removes 50% of W-events and keeps 96% of the signal.

$F_\mu \equiv$ fraction of calorimeter energy around the muon direction in a 0.4 cone over a 0.6 cone. Requiring $F_\mu > 0.7$ (Fig. 6.11b) removes 47% of $W \to \mu\nu$ and keeps 94% of the signal.

Additionally discrimination based on $\Delta R \times p_T^\mu$ was found to be very effective. Muons originating from a jet are closer to the jet axis the more p_T they have [72] while for W muons the distribution in this parameter is uniform. The $\Delta R \times p_{T\mu} < 3.5$ GeV cut was applied as shown on Fig. 6.11c. These three cuts are not independent, but combined reduce the W background by 95% while keeping 75% of signal.

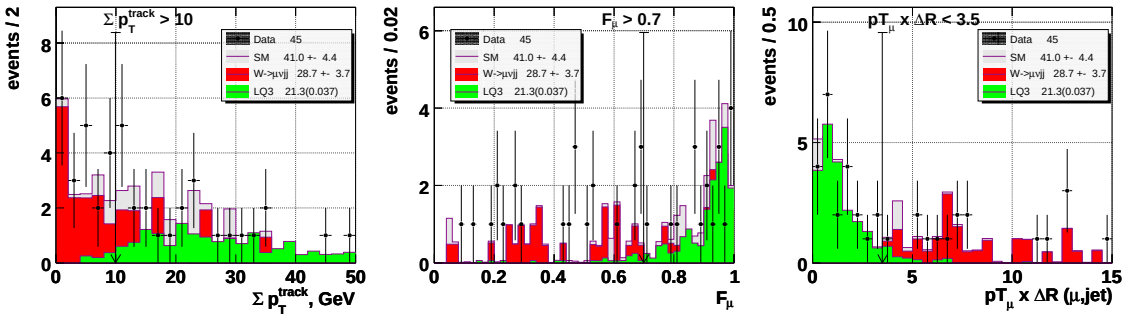

Figure 6.11: Distributions of the isolation variables used for the suppression of the W background (red histograms). *a*) Sum of tracks p_T in a cone of 0.5 around the muon, *b*) Fraction of calorimeter energy around the muon direction in a 0.4 cone over a 0.6 cone (F_μ), *c*) $\Delta R \times p_T^\mu$ distribution. SM background is shown in grey histograms and the leptoquark signal for M_{LQ}=150 GeV is shown in green histograms.

For the dimuon channel all cuts shown in Table 6.6 except the $E_T^{rjet} > 50$ GeV cut were applied. Following all cuts three events remain in the data compared to 3.8 expected from SM processes. 2.7% of the $M_{LQ3} = 150$ GeV signal sample survived the selection. The higher acceptance of the $M_{LQ3} = 200$ GeV signal could allow the $\not\!\!E_T$ cut to be increased up to 85 GeV to improve the signal to background ratio.

Table 6.6: Number of data events and expected signal after selection cuts.

Cut	Data	SM±stat	Signal[a] (Accept.%)	W($\mu\nu$) +jj	W/Z($l\nu$) +jj	W/Z($l\nu$) +$b\bar{b}$	Top[a]
"noQCD"	191	177±9	36.2(6.2%)	101	37.0	7.45	32.8
e/μ iso. veto	146	142±9	35.7(6.1%)	86.6	32.9	5.45	17.7
$\|\eta_{det}\| < 1.5$	111	110±7	31.8(5.5%)	65.9	23.8	4.43	16.0
$X_{jj} > 0.8$	76	70.4±6.4	26.9(4.6%)	44.5	18.9	3.33	3.63
$E_T^{rjet} > 50.$	45	41.0±4.4	21.3(3.7%)	28.7	7.01	2.15	3.08
$p_T^{\mu} > 6.$	38	33.9±3.9	18.7(3.2%)	27.8	1.59	1.76	2.73
$F_{\mu} > 0.7$	19	19.7±2.9	17.6(3.0%)	14.8	1.59	1.29	2.08
$\Sigma p_T^{track} > 10.$	7	9.02±1.87	17.1(2.9%)	5.25	0.95	1.10	1.71
$\Delta R \times p_T^{\mu} < 3.5$	3	3.76±0.85	15.9(2.7%)	1.43	0.00	1.01	1.32

[a]for $M_{LQ3} = 150$ GeV

[a]The SM MC samples are arranged in groups: W($\mu\nu$)jj contains only W($\mu\nu$)jj; W/Z($l\nu$)jj includes all W($e\nu, \tau\nu$)+jj and Z($\nu\nu$)+jj; samplesW/Z($l\nu$)$b\bar{b}$ includes all W($\mu\nu, e\nu, \tau\nu$)+$b\bar{b}$ and Z($\nu\nu$)+$b\bar{b}$; Top contains $t\bar{t}$ and single top samples. Signal acceptance is shown for M_{LQ3}=150 GeV

Fig. 6.12 show the $\not\!\!E_T$ and jet multiplicity (for jets with $E_T > 20$ GeV) distributions for data, LQ3 signal and SM Monte Carlo after all cuts. The dominant

backgrounds are W and $t\bar{t}$ events. We obtained a 95% confidence level (CL) observed

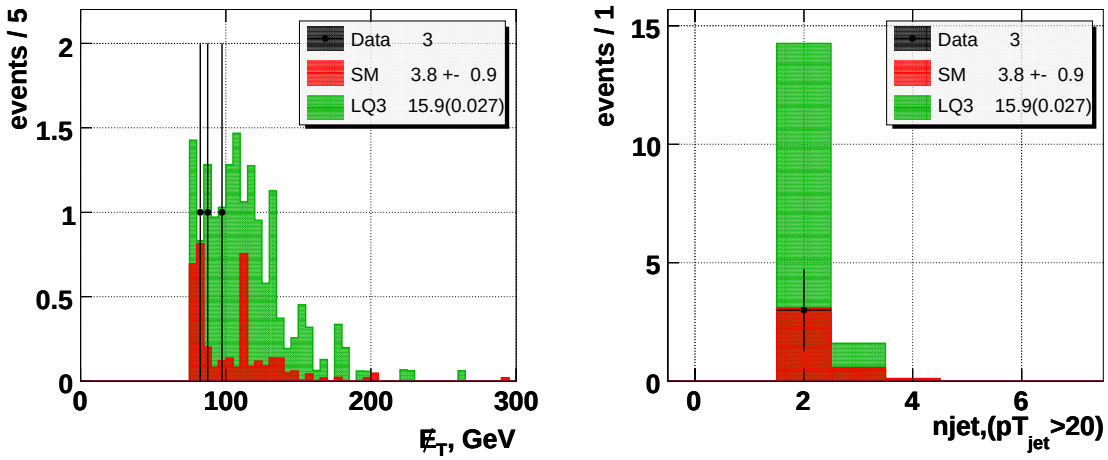

Figure 6.12: a) The $\not\!\!E_T$ and b) the jet multiplicity distributions after the muon tagging. SM background is shown in red histograms and the leptoquark signal for M_{LQ}=150 GeV is shown in green histograms.

and expected limits on cross section using algorithms described in [73]. The observed limit is calculated using the number of data events which survived selection cuts. Calculation of the expected limit set $N_{data} \equiv N_{mc}$ where N_{mc} is the number of SM events which survived the same cuts. The observed and expected limits for the signal cross section for M_{LQ3} of 150, 160, 170, 200 GeV are shown in Table 6.7. The systematic errors on trigger efficiency, jet calibration corrections, SM cross sections and integrated luminosity are taken into account in the limit determination as will be described in Section 6.8. The result allows us to exclude leptoquarks with masses below 180 GeV.

Table 6.7: Muon tagging analysis summary.

M_{LQ3}	$\not\!\!E_T$	Data	SM±stat±sys	Accept.	σ 95% CL limit	M_{LQ3}
GeV	GeV			%	pb obs/exp	exclusion
150	75	3	$3.8 \pm 0.9 \pm 1.0$	15.9(2.7%)	0.58 / 0.58	yes
160	75	3	$3.8 \pm 0.9 \pm 1.0$	12.2(3.1%)	0.50 / 0.54	yes
170	75	3	$3.8 \pm 0.9 \pm 1.0$	9.34(3.4%)	0.46 / 0.47	yes
200	85	2	$2.6 \pm 0.5 \pm 1.2$	3.73(3.8%)	0.36 / 0.36	**180 GeV**

6.7 Combining muon and JLIP b-tag

In the muon tagging analysis, the remaining W background is difficult to suppress without losses in signal acceptance. While increasing the $\not\!\!E_T$ cut gave some improvement the flat shape of the $\not\!\!E_T$ spectra restricts this possibility. A vertex based b-tag suppressed the W background and instrumental backgrounds while having good signal efficiency. This makes it possible to relax isolation requirements and the $\not\!\!E_T$ cut. We will use $M_{LQ3} = 200$ GeV to illustrate the effect of the additional b-tag cut.

First, to check the validity of the JLIP tagger, we applied a single JLIP b-tag to the sample corresponding to the"noQCD" point of Table 6.6 plus a veto on isolated leptons. The tagged jet could be the muon associated jet. The result, Table 6.8, shows an agreement between data and SM for all JLIP working points with 67% ($P^{lf}_{4.0}$ tag) to 48%($P^{lf}_{0.1}$ tag) of the signal surviving.

Second, we applied a single JLIP b-tag to data and MC samples which survived muon cuts The muon tag analysis (Table 6.7) reduced the data sample to 2 events.

Adding a single JLIP tag reduced this to zero at all JLIP working points (Table 6.9). For the $P^{lf}_{4.0}$ point, it decreased SM backgrounds by 25% while keeping 90% of signal.

Table 6.8: JLIP b-tag after "noQCD" cuts, $M_{LQ3} = 200$ GeV

Tag	Data	SM±stat	Signal (Accept. %)	S/$\sqrt{B}$	σ 95% CL limit observed[a]
"noQCD" + e/μ iso. veto	146	142±8	8.3±0.30 (8.4%)	0.69	
$P^{lf}_{4.0}$	17	17.9±1.5	5.6±0.2 (5.7%)	1.32	0.51
$P^{lf}_{2.0}$	10	13.8±1.2	5.4±0.2 (5.5%)	1.45	0.36
$P^{lf}_{1.0}$	10	11.2±1.0	5.1±0.2 (5.2%)	1.53	0.44
$P^{lf}_{0.5}$	7	9.2±0.8	4.8±0.2 (4.9%)	1.58	0.38
$P^{lf}_{0.3}$	7	8.2±0.7	4.6±0.2 (4.6%)	1.59	0.42
$P^{lf}_{0.1}$	5	6.3±0.6	4.0±0.2 (4.1%)	1.59	0.42

[a]The observed limits shown are calculated including statistical errors on the number of SM background, 15% error on signal acceptance and 6.5% error on the integrated luminocity.

Finally the cuts were relaxed to gain signal acceptance by not using the F_μ cut and reducing the $\not\!\!E_T$ requirement to 70 GeV. Table 6.10 shows the JLIP working points for the final set in which the $P^{lf}_{2.0}$ JLIP b-tag point corresponds to the maximum of the S/$\sqrt{B}$ ratio. After the final cuts the SM background contains mainly events from the Top and W/Z$(l\nu)b\bar{b}$ channels; the contribution of other W events is only 12% (Table 6.12). Fig. 6.7 shows the $\not\!\!E_T$ distribution for the $M_{LQ3} = 200$ GeV

Table 6.9: JLIP b-tag after all μ-tag cuts, $M_{LQ3} = 200$ GeV

Tag	Data	SM±Stat	Signal (Accept. %)	S/$\sqrt{B}$	95% CL limit[a], pb
$\mu - tag$ cuts	2	2.3±0.5	3.7 (3.8%)		0.36
$P^{lf}_{4.0}$	0	1.7±0.2	3.3±0.2 (3.4%)	2.51	0.26
$P^{lf}_{2.0}$	0	1.6±0.2	3.2±0.2 (3.3%)	2.51	0.27
$P^{lf}_{1.0}$	0	1.5±0.2	3.1±0.2 (3.1%)	2.48	0.28
$P^{lf}_{0.5}$	0	1.4±0.2	2.9±0.2 (2.9%)	2.42	0.30
$P^{lf}_{0.3}$	0	1.3±0.1	2.7±0.2 (2.8%)	2.37	0.32
$P^{lf}_{0.1}$	0	1.1±0.1	2.4±0.1 (2.5%)	2.26	0.36

[a]The observed limits shown are calculated including statistical errors on the number of SM background, 15% error on signal acceptance and 6.5% error on the integrated luminocity.

signal and SM Monte Carlo samples.

The contribution of QCD and $W/Z(lv) + c\bar{c}$ SM sources to the total background after all cuts is small. The JLIP b-tag removes 10 times more $W/Z(lv) + c\bar{c}$ events then $W/Z(lv) + b\bar{b}$, thus its expected contribution after all cuts is less then 0.1 events. The contribution of the QCD background is estimated from the number of data events after the selection cuts (Table 6.6). Assuming there are less then five QCD events after the $\Delta R \times p_T^{\mu} < 3.5$ GeV cut and using 2% for the mistag rate of the applied $P^{lf}_{2.0}$ tag, less then 0.1 QCD events will survive all cuts. For the cross section limit calculation the combined contribution of the QCD and $W/Z(lv) + c\bar{c}$ was taken as 0 as it give the most conservative limit.

The 95% CL limits are shown in Table 6.11 for different leptoquark masses

with systematic errors taken into account. The cross section limit for $M_{LQ3} =$ 200 GeV is now 0.24 pb compared to 0.36 pb for the muon-tag only analysis.

Table 6.10: JLIP b-tag, $M_{LQ3} = 200$ GeV, optimized $\mu - tag$ cuts.

Tag	Data	SM±Stat	Signal(Accept. %)	S/$\sqrt{B}$	95% CL limit[a], pb
$P^{lf}_{4.0}$	2	2.6±0.3	3.7±0.2 (3.7%)	2.28	0.37
$P^{lf}_{2.0}$	0	2.4±0.3	3.5±0.2 (3.6%)	2.30	0.25
$P^{lf}_{1.0}$	0	2.2±0.2	3.4±0.2 (3.4%)	2.29	0.26
$P^{lf}_{0.5}$	0	2.0±0.2	3.2±0.2 (3.2%)	2.25	0.27
$P^{lf}_{0.3}$	0	1.9±0.2	3.0±0.2 (3.1%)	2.21	0.29
$P^{lf}_{0.1}$	0	1.6±0.2	2.7±0.1 (2.7%)	2.12	0.33

[a]The observed limits shown are calculated including statistical errors on the number of SM background, 15% error on signal acceptance and 6.5% error on the integrated luminocity.

Table 6.11: Summary for muon for MUON + JLIP tagging analysis.

M_{LQ3}	Data	SM±stat±sys	LQ3±stat±sys	Accept.	σ 95% CL limit
GeV	# events	# events	# events	%	pb obs(exp)
150	0	2.4±0.3±0.5	13.4±0.9±1.2	2.3±0.3	0.38(0.59)
160	0	2.4±0.3±0.5	10.9±0.5±0.9	2.8±0.2	0.31(0.49)
170	0	2.4±0.3±0.5	8.4 ±0.4±0.8	3.1±0.3	0.28(0.45)
200	0	2.4±0.3±0.5	3.5 ±0.2±0.3	3.6±0.3	0.24(0.37)
220	0	2.4±0.3±0.5	2.1 ±0.1±0.2	4.1±0.3	0.21(0.33)

Table 6.12: Individual contributions of the backgrounds after the b-tag and relaxed muon cuts. $M_{LQ3} = 200$ GeV

Cut	Data	Bkg±stat[a]	Signal (acpt,%)	W($\mu\nu$) +jj	W/Z($l\nu$) +jj	W/Z($l\nu$) +$b\bar{b}$	Top
All cuts	0	2.4±0.3	3.5±0.2 (3.6%)	0.2	0.0	1.1	1.1

[a]The estimated contribution W/Z($l\nu$)+$c\bar{c}$ and QCD backgrounds is less then 0.2 events, as described in text. For the cross section limit calculation it was taken as 0, as give the most conservative limit.

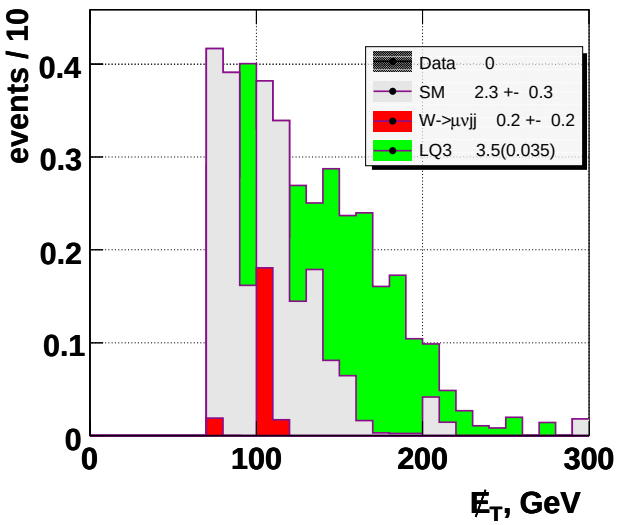

Figure 6.13: The $\not\!\!E_T$ distribution after the muon- and b-tagging. The contribution of the W+two light jets background (red histogram) is small compare to W/Z($l\nu$)+$b\bar{b}$ and Top samples (grey histograms). The leptoquark signal for M_{LQ}=200 GeV is shown in green histogram.

6.8 Systematic uncertainties

Sources of systematic uncertainties included errors on the determination of the integrated luminosity and SM cross sections. Trigger and jet selection efficiencies were measured with data and their contribution to the systematic errors was small. The energy of jets (and $\not\!\!E_T$) were varied within the energy scale correction errors and the impact on the signal acceptance and background rates were determined with MC. Errors on the efficiency to tag jets came from two sources. Jets required at least two charged particles in the silicon tracker for the JLIP algorithm. This depended on the jet's location and energy and gave an uncertainty of 2%. Uncertainties in the b-tagging itself gave errors of about 5% for signal and for background. An error due to the $b \to \mu$ branching fraction is 6%. Systematic errors are summarized in Table 6.13. Other sources of systematic errors have been studied. The systematic errors due to cuts on Σp_T^{track} and $\Delta R \times p_T^{\mu}$ were studied by varying these cuts by $\pm 10\%$. The influence of the PDF error on the LQ3 acceptance was evaluated by changing bounds on the $|\eta|$ of the leading jets by ± 0.1. For $M_{LQ3} = 200$ GeV the effect of simultaneous decreasing or increasing these cuts contribute less than $\pm 4\%$ to the signal acceptance.

6.9 Leptoquark Mass Limit

Figure 6.9 show the theoretical cross section for leptoquark pair production. The uncertainty includes the renormalization scale variation $\mu = \pm 2 M_{LQ}$ and the PDF uncertainties. The upper limit on the leptoquark mass M_{LQ} was obtained by the intersection of the observed 95% cross section limit curve with the lower bound

Table 6.13: Systematic uncertainty summary (in percents.)

	Jet energy scale	b-tagging efficiency	Int. lum.	SM cross section	Trigger efficiency	Jet selection	$b \to \mu$ BF
Signal[a]	+4.2,-3.2	+4.8,-5.2	6.5	–	5.0	1.0	6.0
SM bkg.	+7.7,-9.7	+5.3,-5.6	6.5	15.0	5.0	–	–

[a]for $M_{LQ3} = 200$ GeV sample

of theory.

The actual experimental limits are on $\sigma \times B^2$, where B denotes the $LQ \to \nu b$ branching fraction. If $M(LQ) < M(t)+M(\tau)$ the νb channel is the only decay mode for charge 1/3 LQ. Above the $M(LQ) = M(t)+M(\tau)$ threshold the $t\tau$ decay channel may be possible. We will obtain mass limits for two cases. The first is $B = 1$ for all LQ masses. For the second, we assume that at very large LQ masses the branching fraction for the νb and $t\tau$ channels are each 0.5. Just above $M(t) + M(\tau)$, the $t\tau$ is kinematically suppressed and the possibility of $t\tau$ decay is determined by the suppression factor F_{sp}. Correspondingly for the νb channel we used B(LQ $\to \nu b$) = $1-0.5*F_{sp}$, where $F_{sp} = \sqrt{(1+d_1-d_2)^2-4d_1}[1-(d_1+d_2)/2-(d_1-d_2)^2/2]$, with $d_1 = (m_t/M_{LQ})^2$ and $d_2 = (m_t/M_{LQ})^2$. For $M_{LQ} = 200$ GeV this give B^2=0.93.

Muon tagging alone allows us to exclude at 95% CL leptoquarks with mass up to 180 GeV. The limit established in combination with a JLIP b-tag is stronger. Assuming a decay into the $\nu\bar{\nu}b\bar{b}$ channel, a mass limit of 195 GeV for charge 1/3 third generation leptoquarks was obtained. This limit assumes that $LQ \to \tau t$ occurs and is suppressed due to phase space. If $B = 1$, then the mass limit is 197 GeV.

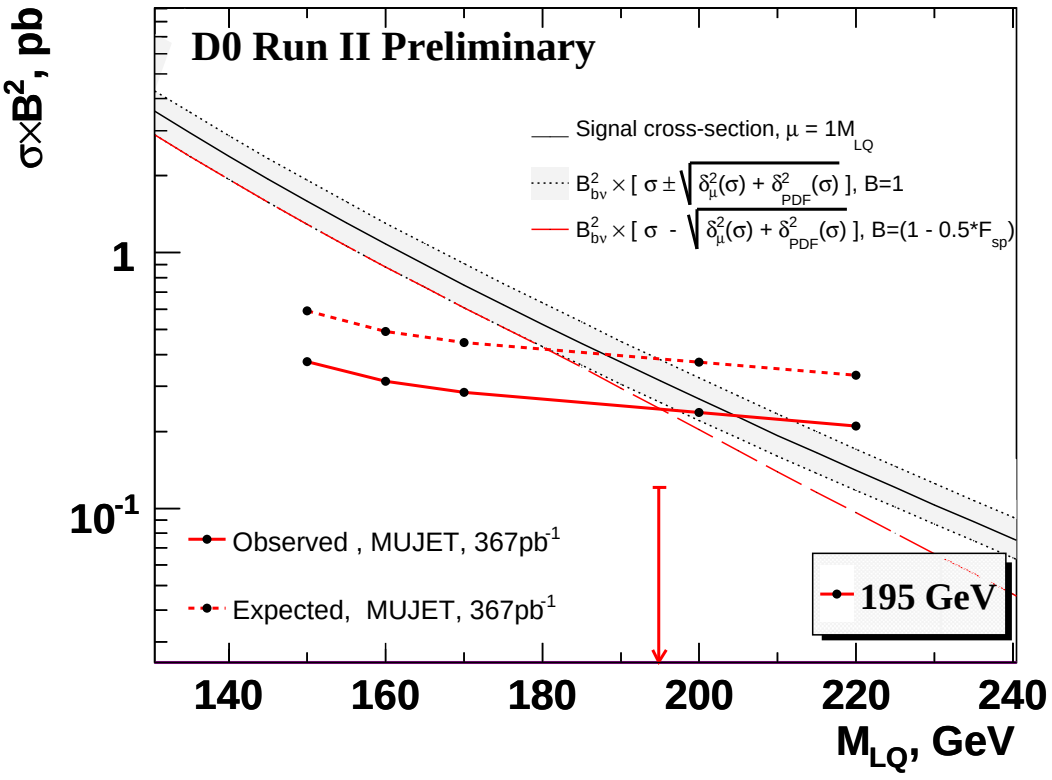

Figure 6.14: The 95% CL limit on σB^2 (points plus solid line) as a function of M_{LQ} for the pair production of third generation leptoquarks. The theory band which includes PDF and the renormalization scale errors is shown in grey. The long-dashed line below the theory band indicates the threshold effect for the τt channel. Also shown are the expected 95% CL limits (points plus short-dashed line)

Appendix A. Conditions of the data skim and triggers used in this analysis

Skim

Events were selected requiring at least one *loose* muon with $p_T^{\mu} > 4$ GeV and $\Delta R(jet, \mu) < 0.7$ rad

MUJET triggers

- **MU_JT20_L2M0** trigger (Aug 22, 2002 - Jun 28, 2004)

  L1: require a muon scintillator trigger and one
  jet trigger tower with $E_T > 3$ GeV

  L2: a muon candidate with medium quality and one jet with $E_T > 10$ GeV

  L3: at least one jet with $E_T > 20$ GeV
  ($E_T > 25$ GeV for the MU_JT25_L2M0 trigger)

- **MU_JT25_L2M3** trigger (Aug 23, 2004 - Nov 11, 2004)

  L1: require a muon scintillator and
  loose wire trigger and one jet trigger tower with $E_T > 5$ GeV

  L2: a muon candidate with medium quality and one jet with $E_T > 10$ GeV

  L3: at least one jet with $E_T > 25$ GeV

Appendix B. Selection of the W signal.

The signal $W \rightarrow \mu\nu$ sample was selected using the MUJET triggers to study the efficiency of jet selection criteria. The following criteria were required:

• $\not\!\!E_T > 20$ GeV, $E_T^{jet1} > 40$ GeV, $E_T^{jet2} > 20$ GeV

• isolated track-matched muon of *medium* or *loose*

quality with $p_T > 20$ GeV, no other isolated muons or electrons with $p_T > 5$ GeV. We looked for *loose* muons only when we had no *medium* candidates or the *medium* candidate had $type = 1$. *Loose* muons were selected in approximately 10% out of the total number of events.

• muon isolation from the nearest jet: $\Delta R > 0.5$

• energy in the hollow cone between 0.1 and 0.4

around the muon direction should be less than 2.5 GeV

• difference in the calorimeter energy in cones 0.6 and 0.4

around the muon should be below 3.5 GeV

• scalar sum of p_T of tracks in the cone 0.5 around the muon

should be less than 2.5 GeV

• χ^2 of track matched to the muon should be less than 3.3

• $\Delta\phi$ between the muon and $\not\!\!E_T$ is required to be greater than 0.6 rad

• reconstructed W transverse mass should be below 200 GeV

For efficiency determination events in the m_T window of 50-90 GeV were selected.

Appendix C. Trigger efficiency parameterization for the MU_JT25_L2M0 and MU_JT25_L2M3 triggers.

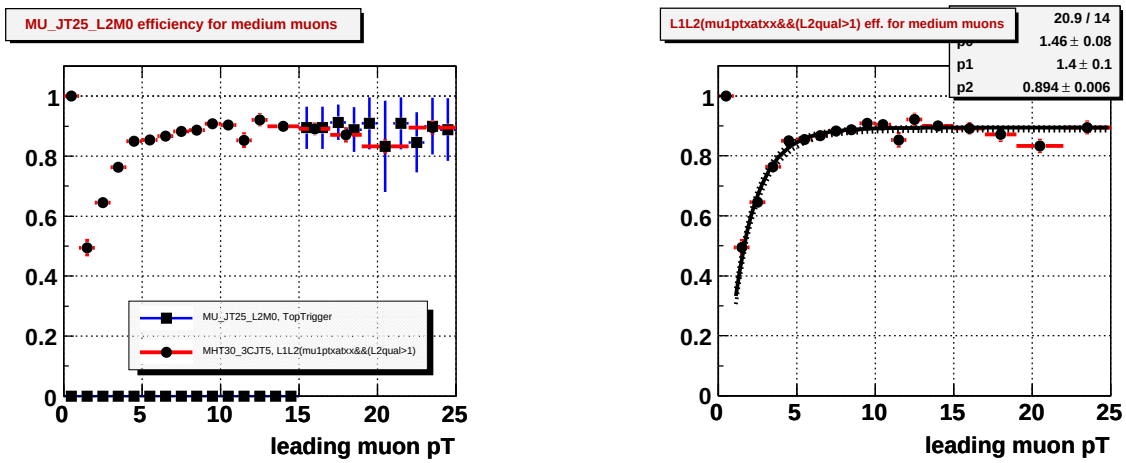

a)

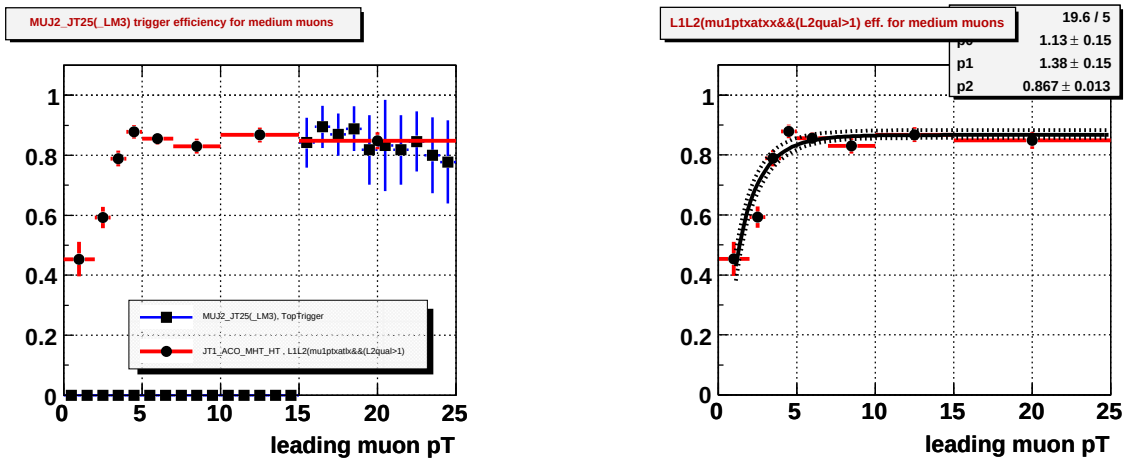

b)

Figure 6.15: MU_JT25_L2M0 trigger (a) and MUJ2_JT25_LM3 trigger (b). Efficiency (left plot, red graph) as a function of the leading muon p_T measured with a missing H_T trigger and its parameterization (right plot, black graph) with the errors bounds (dotted lines). The efficiency as calculated with the TopTrigger package for the signal sample M_{LQ3}=150 GeV (left plot, blue graph) is shown for comparison.

REFERENCES

[1] F. J. Yndurain, "Quantum Chromodynamics: An Introduction to the Theory of Quarks and Gluons", (1983); G. Altarelli, "The Development of Perturbative QCD", (1994); W. Greiner and A. Schafer, "Quantum Chromodynamics", (1994).

[2] P. Renton, "Electroweak Interactions, An Introduction to the Physics of Quarks and Leptons", Cambrige University Press (1990).

[3] R. P. Feynman, "QED" (1985); P. W. Milonni, "The Quantum Vacuum: An Introduction to Quantum Electrodynamics", (1994)

[4] G. Backenstoss, B. D. Hyams, G. Knop, P.C. Marin, and U. Stierlin,"Helicity of μ-mesons from π^- decay", Phys. Rev. Lett. V6 8 415 (1961).

[5] P. Lanacker, "Grand Unified Theories and Proton Decay",
Phys. Rep, 72 (1981).

[6] H. Murayanna and T. Yanagida, "A Viable SU(5) GUT with light Leptoquark Bosons", Mod. Phys. Let. A7 147 (1992).

[7] S. Eidelman *et al.*, Physics Letters B592, 1 (2004) and 2005 partial update for edition 2006.

[8] W. J. Marciano and G. Senjanovic, "Predictions of Supersymmetric Grand Unified Theories", Phys. Rev. D25 3092 (1982).

[9] M. M. Boyce, M. A. Doncheski, and H. Konig, "Charged Heavy Lepton Production in Superstring Inspired E_6 Models", Phys. Rev D55 68 (1997).

[10] W. Buchmüller, R. Rückl and D. Wyler, Phys. Lett. B191 442 (1987), Erratum B448 320 (1999).

[11] S. Davidson. D .C. Bailey and B .A. Campbell, "Model independent constraints on leptoquarks from rare processes", Z. Phys. C61 613 (1994).

[12] A. Djouadi, T. Kohler, M. Spira, J. Tutas, Z. Phys. C 46:679 (1990).

[13] P. H. Frampton and T. W. Kephart, "Higgs Sector and Proton Decay in SU(15) Grand Unification", Phys. Rev D42 3892 (1990); P. H. Frampton, "Light Leptoquarks as possible Signature of Strong Electroweak Unification", Mod. Phys. Lett. A7 559 (1992).

[14] T. G. Rizzo, "Desert GUTs and New Light Degrees of Freedom", Phys. Rev. D45 3903 (1992).

[15] J. C. Pati and A. Salam, "Unified Lepton-Hadron Symmetry and a Gauge Theory of the Basic Interactions", Phys. Rev. D8 1240 (1973).

[16] D. E. Acosta and S. K. Blessing, "Leptoquark searches at HERA and the Tevatron," Ann. Rev. Nucl. Part. Sci. **49**, 389 (1999).

[17] P. B. Straub, "Minireview of leptoquark searches," arXiv:hep-ex/0212023.

[18] S. Hagopian [DØ and CDF Collaborations], "Leptoquark summary from the Tevatron," *Prepared for 13th Topical Conference on Hadron Collider Physics, Mumbai, India, 14-20 Jan 1999.*

[19] C. Adloff *et al.* [H1 Collaboration], Z. Phys. C 74:191 (1997).

[20] J Breitweg *et al.* [ZEUS Collaboration], Z. Phys. C 74:207 (1997).

[21] J. L. Hewett and T. G. Rizzo, "Much ado about leptoquarks: A comprehensive analysis," Phys. Rev. D **56**, 5709 (1997). [arXiv:hep-ph/9703337].

[22] J. Blümlein and R. Rückl, "Production of Scalar and Vector Leptoquarks in e^+e- Annihilation", Phys. Lett. B **304** 337 (1993);
J. Blümlein, E. Boos, and A. Kryukov, "Vector Leptoquark Pair Production in e^+e- Annihilation", Phys. Lett B **392** 137 (1997).

[23] N. Cabibbo and R. Gatto, Phys. Rev **124** 1577 (1961).

[24] J. L. Hewett and S. Pakvasa, Phys. Rev. D **37** 3165 (1988);
J. Blümlein, E. Boos and A. Kryukov, "Leptoquark pair production in hadronic interactions," Z. Phys. C **76**, 137 (1997).

[25] M. Kramer, T. Plehn, M. Spira and P. M. Zerwas, "Pair production of scalar leptoquarks at the Tevatron", Phys. Rev. Lett. **79**, 341 (1997) [arXiv:http://arxiv.org/abs/hep-ph/9704322].

[26] B. Abbott *et al.* [DØ Collaboration], "Search for charge 1/3 third generation leptoquarks in p anti-p collisions at s**(1/2) = 1.8-TeV," Phys. Rev. Lett. **81**, 38 (1998) [arXiv:hep-ex/9803009].

[27] F. Abe *et al.* [CDF Collaboration], "Search for Second and Third Generation Leptoquarks Including Production via Technicolor Interactions in pp-bar collisions at s**(1/2) = 1.8-TeV", Phys. Rev. Lett. **85**, 20562061 (2000).

[28] F. Abe *et al.* [CDF Collaboration], "Search for third generation leptoquarks in anti-p p collisions at s**(1/2) = 1.8-TeV", Phys. Rev. Lett. **78**, 2906 (1997).

[29] S. Abachi, *et al.*, Phys. Rev. Lett. **74**, 2632 (1995); F. Abe, *et al.*, Phys. Rev. Lett. **74**, 2626 (1995).

[30] See http://www-d0.fnal.gov/www_buffer/pub/Run1_publications.html, http://www-d0.fnal.gov/www_buffer/pub/Run2_publications.html for a complete list of DØ publications in Run I and Run II.

[31] V. M. Abazov *et al.*, "The Upgraded DØ Detector", submitted to Nucl. Instr. and Methods, physics/0507191, Fermilab-Pub-05/341-E.

[32] S. T. Repond, "The Central Tracker Trigger System of DØ ", DØ Note **3925**; 7th International Conference on Advanced Technology and Particle Physics Villa Olmo, Cosmo, Italy, Oct. 15-19, 2001.

[33] The DØ Collaboration, "The DØ Silicon Tracker Technical Design Report", DØ Note **2169** (1994).

[34] The DØ Collaboration, "The DØ Central Fiber Tracker Technical Design Report", http://d0server1.fnal.gov/projects/SciFi/cft_home.html, (1997).

[35] S. Abachi *et al.* [DØ Collaboration], "The DØ Detector," Nucl. Instrum. Meth. A **338**, 185 (1994).

[36] B. Baldin, *et.al.*, "Technical Design of the Central Muon System", DØ Note **3365** (1997).

[37] G. Alexeev, *et.al.*, "Technical Design Report for the DØ Forward Muon Tracking Detector based on Mini-drift Tubes", DØ Note **3366** (1997).

[38] A. Lo, C.-C. Miao, R. Partridge, "Luminocity Monitor Technical Design Report", DØ Note **3320** (1997); C.-C. Miao, "The DØ Run II Luminocity Monitor", Nucl. Phys. Proc. Suppl., 78 342-347 (1999).

[39] W. Taylor [DØ Collaboration], "An impact parameter trigger for the DØ experiment," IEEE Trans. Nucl. Sci. **48**, 557 (2001).

[40] T. Cristiansen, "The D-Zero L2-Muon Trigger Performance for P11", DØ Note **4053** (2002).

[41] T. Cristiansen, Ph.D thesis, (chapter 4 and 5) (2003), http://www.physik.uni-muenchen.de/ tcrist/prelim/diss.pdf

[42] A. Maciel, S. Uzunyan, C. Leonidopulos, J. Kowalkowski, "The L2-Muon Trigger Methods and Algorithms," DØ Note **4756** (2005).

[43] M. Fortner, A. Maciel, H. Evans, B. Kothari and S. Uzunian, "The level-2 muon trigger at DØ ", IEEE Trans. Nucl. Sci. **49** 1589 (2002).

[44] A. Maciel, "Muon-Track Matching at Level-2", DØ Note **4726** (2005).

[45] A. Maciel, "Muon timing at Level-2", DØ Note **4445** (2004).

[46] D. Wood *et.al.*, "Muon Data Formats to L2 & L3", DØ Note **3537** (1998).

[47] S. Protopopescu, S. Baffiony, E. Nagy, "Thumbnail: a compact data format", DØ Note **3979** (2002).

[48] C. Clemént *et.al.*, "MuonID Certification Data for p14", DØ Note **4530** (2004).

[49] E. Busato, B. Andrieu, "Jet Algorithms in the DØ Run II Software: Description and User's Guide", DØ Note **4457** (2004).

[50] G.C. Blazey *et. al.*, in "Proc. of the QCD and Weak Boson Physics in Run II Workshop (Batavia 1999)", [hep-ex/005012].

[51] EM ID certification page, http://www-d0.fnal.gov/phys_id/emid/d0_private/certification.

[52] D. Chapin *et. al.*, "Measurement of $Z \rightarrow e^+e^-$ and $W \rightarrow e^{+/-}\nu$ Production Cross Section with $|\eta| < 2.3$ ", DØ Note **4897** (2005).

[53] L. Saweyer and A.L Stone, "Missing ET Reconstruction: Variables and Methods", DØ Note **3957** (2002).

[54] The JLIP agorithm description,
http://www-d0.fnal.gov/phys_id/bid/d0_private/certification/p14Pass2/JLIP.

[55] Guide To MC Generation,
http://www-clued0.fnal.gov/runjob/current/tutorials.

[56] T. Sjostrand *et al.*, Computer Phys. Commun. 135 238 (2001).

[57] M. L Mangano *et al.*, "ALPGEN, agenerator for hard multiparton processes in hadronic collisions", JHEP 0307 (2003).

[58] E .Boos *et al.*. [CompHEP Collaboration], "CompHEP 4.4: Automatic computations from Lagrangians to events", Nucl. Instrum. Meth. A534, p250 [hep-ph/0403113] (2004).

[59] H. L. Lai *et al.*, Eur. Phys. J C12, 375 (2000).

[60] A. Agostinelli *et al.*, NIM A 506, 250-303 (2003).

[61] DØ Trigger Simulator Manual.
http://www-d0.fnal.gov/computing/trigsim/general/docs/manual.

[62] L. Duflot, *et. al.*, "Search for Squarks and Gluinos in the Jets + Missing E_T topology with *DØ* Detector", DØ Note **4737** (2005).

[63] W. Fisher, "A Search for Anomalous Heavy-Flavor Quark Production in Assocoation with W Bosons", DØ Note **4594** (2004).

[64] M. Agelou, *et. al.*, "Top trigger efficiency measurement and the top trigger package", DØ Note **4512** (2004).

[65] http://www-clued0.fnal.gov/ nunne/cross-sections/nnlo_xsect.html.

[66] N. Kidonakis and R. Vogt, Int. Mod. Phys. **A19** 1793 (2004).

[67] http://www-d0.fnal.gov/Run2Physics/top/d0_private/wg/singletop/singletop.html.

[68] M. Mangano, *et. al.*, http://www-d0.fnal.gov/computing/MonteCarlo/generators/matching_prescriptions/mlm/mlm_prescription.html.

[69] E. Nagy, "Comparison of Sherpa/Alpgen/CKKW MC", DØ, New Phenomena Workshop, March, 2004

[70] K. Hanagaki, J. Kasper, "Identification of b-jet by Soft Muon", DØ Note **4867** (2005).

[71] A. Maciel, A. Sznajder, "Run-1b Measurement of the b-Quark Production Cross Section from a Sample of Muon Tagged Jets", DØ Note **3705** (1999).

[72] V. Barger, R. Phillips, "Collider physics" Redwood City, Calif. : Addison-Wesley Pub. Co., Advanced Book Program, 1987.

[73] T. Junk, "Confidence level computation for combining searches with small statistics", Nucl. Instrum. Meth. A **434**, 435 (1999) [arXiv:hep-ex/9902006].